

SFR estimations from z = 0 to z = 0.9. A comparison of SFR calibrators for star-forming galaxies

M. Figueira, A. Pollo, K. Malek, V. Buat, M. Boquien, F. Pistis, L. P. Cassarà, D. Vergani, M. Hamed, S. Salim

▶ **To cite this version:**

M. Figueira, A. Pollo, K. Malek, V. Buat, M. Boquien, et al.. SFR estimations from z = 0 to z = 0.9. A comparison of SFR calibrators for star-forming galaxies. Astronomy and Astrophysics - A&A, 2022, 667, 10.1051/0004-6361/202141701 . insu-03863234

HAL Id: insu-03863234
https://insu.hal.science/insu-03863234

Submitted on 21 Nov 2022

HAL is a multi-disciplinary open access archive for the deposit and dissemination of scientific research documents, whether they are published or not. The documents may come from teaching and research institutions in France or abroad, or from public or private research centers.

L'archive ouverte pluridisciplinaire **HAL**, est destinée au dépôt et à la diffusion de documents scientifiques de niveau recherche, publiés ou non, émanant des établissements d'enseignement et de recherche français ou étrangers, des laboratoires publics ou privés.



Distributed under a Creative Commons Attribution 4.0 International License

A&A 667, A29 (2022)
https://doi.org/10.1051/0004-6361/202141701
© M. Figueira et al. 2022

Astronomy & Astrophysics

SFR estimations from $z = 0$ to $z = 0.9$

A comparison of SFR calibrators for star-forming galaxies

M. Figueira[1,2], A. Pollo[1,3], K. Małek[1,4], V. Buat[4], M. Boquien[5], F. Pistis[1], L. P. Cassarà[6,7], D. Vergani[8], M. Hamed[1], and S. Salim[9]

[1] National Centre for Nuclear Research, ul. Pasteura 7, 02-093 Warszawa, Poland
e-mail: Miguel.Figueira@ncbj.gov.pl
[2] Institute of Astronomy, Faculty of Physics, Astronomy and Informatics, Nicolaus Copernicus University, ul. Grudziądzka 5, 87-100 Toruń, Poland
[3] Astronomical Observatory of the Jagiellonian University, Orla 171, 30-244 Kraków, Poland
[4] Aix Marseille Univ, CNRS, CNES, LAM, Marseille, France
[5] Centro de Astronomía (CITEVA), Universidad de Antofagasta, Avenida Angamos 601, Antofagasta, Chile
[6] INAF–IASF Milano, via Bassini 15, 20133 Milano, Italy
[7] Institute for Astronomy, Astrophysics, Space Applications and Remote Sensing, National Observatory of Athens, Penteli 15236, Athens, Greece
[8] INAF – Osservatorio di Astrofisica e Scienza dello Spazio, Via P.Gobetti 93/3, 40129 Bologna, Italy
[9] Department of Astronomy, Indiana University, Bloomington, IN 47404, USA

Received 2 July 2021 / Accepted 4 August 2022

ABSTRACT

Context. The star formation rate (SFR) is a key ingredient for studying the formation and evolution of galaxies. Being able to obtain accurate estimations of the SFR, for a wide range of redshifts, is crucial for building and studying galaxy evolution paths over cosmic time.
Aims. Based on a statistical sample of galaxies, the aim of this paper is to constrain a set of SFR calibrators that are able to work in a large redshift range, from $z = 0$ to $z = 0.9$. Those calibrators will help to homogenize SFR estimations of star-forming galaxies and to remove any possible biases from the study of galaxy evolution.
Methods. Using the VIMOS Public Extragalactic Redshift Survey (VIPERS), we estimated a set of SFR based on photometric and spectroscopic data. We used, as estimators, photometric bands from ultraviolet (UV) to mid-infrared (mid-IR), and the spectral lines Hβ, [O II]λ3727, and [O III]λ5007. Assuming a reference SFR obtained from the spectral energy distribution reconstructed with Code Investigating GALaxy Emission (CIGALE), we estimated the reliability of each band as an SFR tracer. We used the GALEX-SDSS-WISE Legacy Catalog (GSWLC, $z < 0.3$) to trace the dependence of these SFR calibrators with redshift.
Results. The far and near UV (FUV and NUV, respectively), u-band and 24 µm bands, as well as $L_{\rm TIR}$, are found to be good SFR tracers up to $z \sim 0.9$ with a strong dependence on the attenuation prescription used for the bluest bands (scatter of SFR of 0.26, 0.14, 0.15, 0.23, and 0.24 dex for VIPERS, and 0.25, 0.24, 0.09, 0.12, and 0.12 dex for GSWLC). The 8 µm band provides only a rough estimate of the SFR as it depends on metallicity and polycyclic aromatic hydrocarbon properties (scatter of 0.23 dex for VIPERS). We estimated the scatter of rest-frame luminosity estimations from CIGALE to be 0.26, 0.14, 0.12, 0.15, and 0.20 dex for FUV, NUV, ugriz, $K_{\rm s}$, and 8–24 µm-$L_{\rm TIR}$. At intermediate redshift, the Hβ line is a reliable SFR tracer (scatter of 0.19 dex) and the [O II]λ3727 line gives an equally good estimation when the metallicity from the R_{23} parameter is taken into account (0.17 for VIPERS and 0.20 dex for GSWLC). A calibration based on [O III] retrieves the SFR only when additional information such as the metallicity or the ionization parameter of galaxies are used (0.26 for VIPERS and 0.20 dex for GSWLC), diminishing its usability as a direct SFR tracer. Based on rest-frame luminosities estimated with CIGALE, we propose our own set of calibrations from FUV, NUV, u-band, 8, 24 µm, $L_{\rm TIR}$, Hβ, [O II], and [O III].

Key words. Galaxy: evolution – Galaxy: general – galaxies: photometry – galaxies: star formation – techniques: spectroscopic

1. Introduction

The formation and evolution of galaxies is a complex process guided by the buildup of stellar mass (M_*) through the formation of stars. By measuring the star formation rate (SFR), the evolution of galaxies over cosmic time can be quantified through the cosmic star formation history (e.g., Lilly et al. 1995; Madau et al. 1996; Smolčić et al. 2009; Madau & Dickinson 2014; Driver et al. 2018). In other words, the measurement of SFR over a large range of redshift is crucial in order to acquire a broad and accurate understanding of the Universe. Because different surveys are characterized by different sets of observed wavelengths and/or spectroscopic features, it is necessary to be able to estimate the SFR consistently from several bands.

Over several decades a variety of methods have been developed to measure the SFR using different bands (e.g., Searle et al. 1973; Donas & Deharveng 1984; Kennicutt 1998; Kennicutt et al. 2009; Kennicutt & Evans 2012; Davies et al. 2016; Brown et al. 2017). The simplest method, and at the same time the most common, assumes that the flux in a certain rest-frame band is related to the flux emitted by high-mass stars, either directly or indirectly. It implies that a simple scaling exists

Open Access article, published by EDP Sciences, under the terms of the Creative Commons Attribution License (https://creativecommons.org/licenses/by/4.0), which permits unrestricted use, distribution, and reproduction in any medium, provided the original work is properly cited.
This article is published in open access under the Subscribe-to-Open model. Subscribe to A&A to support open access publication.

between the luminosity in this band and the SFR, and so far this assumption has been found to work very well. Bands from X-rays to radio, including also spectral lines, have been used and calibrated, especially in the local Universe where a high statistical precision has been reached using the prolific Sloan Digital Sky Survey (SDSS) database.

In the local Universe, the Hα line ($\lambda \sim 656$ nm) is a common SFR tracer (e.g., Kewley et al. 2004; Brinchmann et al. 2004; Salim et al. 2007, 2016; Brown et al. 2017) used through the SFR calibrations of Kennicutt (1983, 1998) and Kennicutt et al. (1994), and is sensitive to timescales of a few Myr (<20 Myr, Calzetti 2013; Davies et al. 2016). This emission line represents the ionized (H II) regions created through the emission of Lyman continuum photons ($E > 13.6$ eV) from high-mass stars. In addition to being a relatively direct tracer of high-mass stars, it does not depend on metallicity or star formation history (SFH), and the dust attenuation is relatively low.

However, beyond $z \sim 0.5$, the Hα line is redshifted out of the optical window. While some studies make use of Hα above this limit (e.g., McCarthy et al. 1999; Tresse et al. 2002; Maier et al. 2015; Villa-Vélez et al. 2021), these samples generally contain a small number of galaxies and have a narrow redshift range. SFR estimations beyond the local Universe require the use of different bands and calibrations, along with a method to estimate the dust attenuation suffered by galaxies.

The Hβ line ($\lambda \sim 486$ nm), for instance, can be used as an SFR tracer if we assume that it can be related to Hα through the case B recombination. It suffers, however, from higher dust attenuation than Hα and from stellar absorption. Another spectral line commonly used when Hα is not available is the [O II]λ3727 line. This spectral line is less related to the emission of photons from high-mass stars, suffers a high attenuation, and can strongly depend on the ionization parameter and the metallicity. This latter parameter is more difficult to estimate at intermediate redshift and depends on the chosen calibration (Kewley et al. 2004). The [O III]λ5007 line has also been calibrated as an SFR tracer but gives a poor estimation due to its strong dependence on metallicity and the ionization parameter (e.g., Moustakas et al. 2006; Villa-Vélez et al. 2021). Nonetheless, a proper SFR calibration with [O III]λ5007 will become necessary for future observations at high redshift, such as with the *James Webb* Space Telescope (JWST).

As spectroscopic observations are more costly than imaging, they are not available for every galaxy. Instead, surveys are generally performed in the continuum and these continuum bands need to be calibrated to give a reliable estimation of the SFR.

The ultraviolet (UV) continuum represents a direct tracer of the emission of high-mass stars, sensitive to short timescales (~100 Myr, Buat 2015; Davies et al. 2016). However, the calibration factor linking $L_{\rm UV}$ to the SFR shows a dependence on metallicity, which is expected to be more important at higher metallicity (Madau & Dickinson 2014). In addition, UV bands suffer from very high dust attenuation, making them particularly sensitive to the prescription used to correct it. The Balmer decrement method, together with an attenuation law (e.g., Cardelli et al. 1989; O'Donnell 1994; Calzetti et al. 2000), are generally used to correct for dust attenuation through the comparison of the observed Hα to Hβ ratio with the dust-free theoretical value (Berman 1936; Groves et al. 2012). Other methods can be used if those spectroscopic lines are not observed: it is possible to link the attenuation correction to the magnitude in the near-ultraviolet (NUV) and far-ultraviolet (FUV) bands (Hao et al. 2011), use the UV spectral slope ($\beta_{\rm UV}$, Meurer et al. 1999), or simply assume an average correction based on the literature. Thanks to the huge amount of observed galaxies by the UV space telescope GALEX (Martin et al. 2005), several works have calibrated the FUV and NUV bands in the local Universe.

The *u*-band is less affected by dust attenuation than UV bands but can be contaminated by stellar emission from the old stellar population (Hopkins et al. 2003; Prescott et al. 2009; Boquien et al. 2014; Davies et al. 2016), which becomes more and more important as the redshift decreases. However, unlike the previous bands, *u*-band measurements can easily be obtained from ground-based telescopes, making it a powerful SFR tracer, as it reflects the UV part of galaxies past a certain redshift.

On the other side of the spectrum, infrared (IR) bands can also be used as SFR tracers. Because the dust is heated by the UV flux from high-mass stars and it reprocesses the emission in the IR, these bands trace, indirectly, high-mass stars, and therefore the SFR, with a higher timescale (~1 Gyr, Boissier 2013) compared to bluer bands. One advantage is that dust attenuation at these wavelengths is not as significant as in the blue part of the spectrum, and therefore the correction can generally be safely ignored.

At 8 μm, the flux is dominated by the emission of polycyclic aromatic hydrocarbons (PAHs), which are found around H II regions. The luminosity at this wavelength roughly correlates with total infrared luminosity ($L_{\rm TIR}$, 8−1000 μm) (Pope et al. 2008; Nordon et al. 2012) and can be used as an SFR tracer, even though it is known that the metallicity has an impact on the PAH strength, and therefore on the derived calibrations (e.g., Madden et al. 2006; Draine et al. 2007; Ciesla et al. 2014; Schreiber et al. 2018). The luminosity at ~20 μm allows for a robust estimation of $L_{\rm TIR}$ when accounting for the non-linear behavior (e.g., Calzetti et al. 2010) at high SFRs. The observed flux is also often used to estimate $L_{\rm TIR}$ based on templates up to $z \sim 4$ (e.g., Chary & Elbaz 2001; Wuyts et al. 2008; Magdis et al. 2012; Dale et al. 2014; Talia et al. 2015; Boquien & Salim 2021) and is linked to the SFR trough calibrations (e.g., Kennicutt 1998). We note that the accuracy of $L_{\rm TIR}$ estimation based on templates depends on the redshift and the band used. Elbaz et al. (2010) found a scatter of 0.15 dex for $L_{\rm TIR}$ estimation when using the 24-μm band and Chary & Elbaz (2001) templates up to $z \sim 1.5$. The overestimation above redshift 1.5 increases up to a factor of seven. Using Magdis et al. (2012) templates, Talia et al. (2015) found a scatter for $L_{\rm TIR}$ of 0.19 dex for galaxies up to $z \sim 3$. The scatter of $L_{\rm TIR}$ and SFR from a single band were estimated by Boquien & Salim (2021) for *Spitzer*, Wide-field Infrared Survey Explorer (WISE), JWST, and *Herschel* measurements, and ranges from 0.05 to 0.23 dex for $L_{\rm TIR}$, and 0.13 to 0.24 dex for the SFR.

The *Spitzer* satellite enabled a robust calibration of the SFR from the 24-μm band and the WISE satellite (Wright et al. 2010) increased the number of galaxies observed at 22 μm[1] with its all-sky survey, but also at 12 μm from which the SFR can also be derived (e.g., Cluver et al. 2014, 2017). Reliable measurements of $L_{\rm TIR}$ were made possible with the advent of satellites such as the Infrared Space Observatory (ISO) (up to 240 μm), *Spitzer* (up to 160 μm), AKARI (up to 168 μm), and *Herschel* (up to 500 μm).

Because bluer bands represent the emission of high-mass stars and the IR bands represent the dust reprocession, it is possible to use them in combination to obtain the total SFR (e.g., Bell et al. 2005; Kennicutt et al. 2009; Boquien et al. 2014;

[1] The effective wavelength of the WISE-4 band is closer to 22.8 μm (see Wright et al. 2010; Brown et al. 2014a,b).

Clark et al. 2015). These composite calibrations are useful as they are able to give an estimation of the SFR without relying on dust attenuation corrections.

The fact that Hα is more difficult to observe beyond the local Universe represents an obstacle regarding the choice of a reference SFR. Another common method, also used in the local Universe, relies on the reconstruction of the spectral energy distribution (SED) of the galaxies, from which several properties such as the SFR, M_*, and rest-frame luminosity can be estimated. One of the main advantages of SED fitting over pre-calibrated relations at a given wavelength is that the red shifting of the observed data is naturally accounted for.

Such reconstructions are based on stellar population libraries (Bruzual & Charlot 2003; Maraston 2005), dust emission templates (e.g., Chary & Elbaz 2001; Dale & Helou 2002; Draine et al. 2014), active galactic nucleus (AGN) models (Fritz et al. 2006; Stalevski et al. 2012, 2016), SFHs (e.g., Boissier et al. 2003; Buat et al. 2008; Ciesla et al. 2016, 2017), attenuation laws (Charlot & Fall 2000; Calzetti et al. 2000), initial mass function (IMF, Salpeter 1955; Kroupa 2002; Chabrier 2003), and metallicity. Several codes are available to perform broad-band SED fittings of galaxies, such as LePhare (Arnouts et al. 2013), Multi-wavelength Analysis of Galaxy Physical Properties (MAGPHYS, da Cunha et al. 2012), *hyperz* (Bolzonella et al. 2000, 2010), or Code Investigating GALaxy Emission (CIGALE, Burgarella et al. 2005; Noll et al. 2009; Boquien et al. 2019). The obvious limitation is that panchromatic data are mandatory in order to accurately reconstruct the SEDs and obtain reliable estimations of the physical properties of galaxies, and a multiwavelength set of data is not always available. However, a lot of effort was made in order to build multiwavelength catalogs such as the *Herschel* extragalactic legacy project (HELP, Shirley et al. 2021), a catalog of ~170 million objects over 1270 deg^2, based on 51 surveys from optical to the far-infrared (FIR), the GALEX-SDSS-WISE legacy catalog (GSWLC, Salim et al. 2016, 2018), containing ~700 000 galaxies at $z < 0.3$, the GAMA survey (Driver et al. 2016), with ~250 000 objects at $z < 0.5$, or the Deep Extragalactic VIsible Legacy Survey (DEVILS, Davies et al. 2018), with ~60 000 galaxies at $0.3 < z < 1.0$. The existence of more unique, statistically important multiwavelength catalogs makes possible a new calibration of the true SFR.

The goal of this paper is to estimate the SFRs of a sample of star-forming galaxies at intermediate redshifts ($0.5 < z < 0.9$) using the VIMOS Public Extragalactic Redshift Survey (VIPERS), a spectroscopic statistically significant survey with very rich auxiliary data and for which spectral lines are available. We used indicators known to be accurate in the local Universe and measured their reliability at moderate redshifts. To make a comparison at lower redshifts, we made use of GSWLC ($z < 0.3$, Salim et al. 2016, 2018). Based on VIPERS and GSWLC, we derived a new set of calibrations from UV to $L_{\rm TIR}$, and from the spectral lines Hβ, [O II]λ3727, and [O III]λ5007.

The paper is organized as follows. In Sect. 2, we describe the data samples used in this study. In Sect. 3, we present the criteria applied to select the star-forming samples and the parameters of the CIGALE run used to derive the reference SFR and rest-frame luminosities. The analysis of each SFR tracer is presented in Sect. 4 and the discussion of the results, as well as the derivation of new calibrations, are presented in Sect. 5. We present our conclusions in Sect. 6.

Throughout the paper, we used the WMAP7 cosmology (Komatsu et al. 2011) with $\Omega_M = 0.272$, $\Omega_\Lambda = 0.728$, and $H_0 = 70.4$ km s^{-1} Mpc^{-1}. The SFR was estimated based on the Chabrier (2003) IMF. The conversion from the Salpeter (1955) and Kroupa (2002) IMFs was done by applying a multiplicative factor of 0.64 and 0.94, respectively (Madau & Dickinson 2014). All magnitudes are given in the AB system (Oke 1974).

2. The samples of data

2.1. The intermediate-redshift sample: VIPERS

VIPERS is a spectroscopic survey performed with the VIsible Multi-Object Spectrograph (VIMOS, Le Fèvre et al. 2003) and is primarily dedicated to the study of large-scale structures of the Universe through redshift space distortions (Guzzo & VIPERS Team 2013; Garilli et al. 2014; Scodeggio et al. 2018). Nonetheless, the VIPERS catalog can be equally used in the field of galaxy formation and evolution thanks to its statistically significant spectrophotometric sample of ~10^5 galaxies. The volume surveyed by VIPERS (~5×10^7 h^3 Mpc^{-3}) is comparable to 2dFGRS at $z \sim 0.1$ (Colless et al. 2001, 2003). Additionally, because VIPERS targeted galaxies in the range $0.5 < z < 1.2$, this survey can be seen as a unique counterpart of SDSS ($z < 0.5$, York et al. 2000; Ahn et al. 2014; Blanton et al. 2017) at intermediate redshifts.

VIMOS is a 4-channel imaging spectrograph with a 224 arcmin^2 field of view at the European Southern Observatory's Very Large Telescope (ESO/VLT). Observations were performed with the multiobjects-spectroscopic mode and the low-resolution red grism, giving a spectral resolution of $R = 220$ and spectral coverage from 5500 to 9500 Å in the observed frame.

The selection of targets was based on the "T0005" release of the Canada-France-Hawaii Telescope Legacy Survey (CFHTLS, Goranova et al. 2009) Wide photometric catalog toward a subarea of the W1 (~16 deg^2) and W4 fields (~8 deg^2). To limit the sample to galaxies with $z < 1.2$, only sources from the photometric parent catalog having $i_{\rm AB} < 22.5$ mag (after Galactic extinction correction) were selected. To remove galaxies below $z \sim 0.5$, a simple but effective color-color selection based on the g, r, and i bands was applied. Stellar decontamination was performed based on the half-light radius and the reconstruction of the spectral energy distribution from CFHTLS *ugriz* bands. In the end, VIPERS galaxies cover a range of $17.5 < i_{AB} < 22.5$ in magnitude.

The efficiency of these selection criteria was tested with the help of two control samples based on previous studies with VIMOS: VVDS-Deep and VVDS-Wide (Le Fèvre et al. 2005; Garilli et al. 2008) using galaxies observed both in VIPERS and in the control samples. Even though the above selection rules are effective to select intermediate-redshift galaxies from amongst low-redshift galaxies and stars, a perfect sample is not achievable and some contamination was expected. The use of these simple selections, however, allowed the sampling rate to be doubled, reaching ~47%, compared to a selection based only on magnitude (~23% for VVDS-Wide, Garilli et al. 2008).

Using the EZ code (Garilli et al. 2010; García et al. 2014), the observed spectrum was compared to galaxy templates and the contribution of a set of emission lines in order to assign a redshift, which was then independently checked by two members of the VIPERS team. In this work, we used the VIPERS PDR-2[2] catalog consisting of 91 507 objects (galaxies, AGN, and stars).

[2] http://vipers.inaf.it/

2.2. The low-redshift sample: GSWLC

GSWLC[3] (Salim et al. 2016, 2018) is a local galaxy catalog based on the tenth release of SDSS data (Ahn et al. 2014). Three different catalogs were produced depending on the GALEX exposure time (GSWLC-A, -M, and -D for all-sky shallow, medium, and deep exposure time), with a total of 658 911 objects (~90% of SDSS DR10 objects) at $0.01 < z < 0.3$. Photometry was taken from the GALEX GR6/7 final release (Bianchi et al. 2014 with additional corrections, see Salim et al. 2016), the 2MASS Extended Source Catalog (XSC, Jarrett et al. 2000), SDSS DR10, and WISE from the AllWISE Source Catalog and unWISE (Lang et al. 2016). SDSS and GALEX were corrected for Galactic extinction based on Peek & Schiminovich (2013) and Yuan et al. (2013) coefficients. All the details concerning the construction of the catalog can be found in Salim et al. (2016).

We chose to use GSWLC for consistency because the associated catalog of physical parameters was obtained with the CIGALE code, the same as for VIPERS (Sect. 3.2), reducing the bias associated with the use of different SED fitting methods. In the second version of the GSWLC catalog, the WISE-4 (or WISE-3 if not available) band from unWISE was used to estimate $L_{\rm TIR}$ from the Chary & Elbaz (2001) templates, allowing us to better constrain the SED fitting in the IR part of the spectrum. The $L_{\rm TIR}$ was corrected for AGN contamination based on a systematic trend observed for galaxies classified as AGNs in GSWLC-A1, between the SFR estimated from stellar emission and the SFR estimated from WISE-4 (or WISE-3 if not available) observed fluxes (Salim et al. 2018). By using this new method, referred to as the SED+$L_{\rm TIR}$ fitting where the $L_{\rm TIR}$ acts as an additional constraint, the dust emission is less dependent on the reconstructed stellar emission.

We point out here that Chary & Elbaz (2001) templates were constructed two decades ago and it might be risky to use them in order to estimate $L_{\rm TIR}$. When constructing the catalog, Salim et al. (2016) checked the consistency of $L_{\rm TIR}$ estimated using the templates of Chary & Elbaz (2001) with those of Dale & Helou (2002), finding a marginal difference of 0.01 dex between them. In addition, these estimations were compared with $L_{\rm TIR}$ estimated using Dale & Helou (2002) templates for galaxies belonging to the SDSS Stripe82 (Rosa-González et al. 2002) from which they found a very good agreement, with a mean difference of 0.01 dex and a scatter of 0.07 dex.

Estimations of $L_{\rm TIR}$ from 24 μm using the Chary & Elbaz (2001) templates are reliable up to $z = 1.5$ (Elbaz et al. 2010) but can be overestimated by a factor of seven above this redshift (Nordon et al. 2010) due to the different ISM conditions (Magnelli et al. 2010), and above $L_{\rm TIR} \geq 10^{12}\ L_{\odot}$ (Berta et al. 2013). Using the Magdis et al. (2012) templates, it is possible to correctly estimate $L_{\rm TIR}$ up to $z \sim 3$ (scatter of 0.2 dex, Talia et al. 2015).

Because this work focuses on galaxies at $z < 1$, there should not be any problem in using the GSWLC, whose SEDs were constrained by $L_{\rm TIR}$ from the Chary & Elbaz (2001) templates. When estimating $L_{\rm TIR}$ from mid-IR bands in this work, however, we use the new set of templates[4] from Boquien & Salim (2021) (see Appendix. D). We refer the reader to Boquien & Salim (2021) for a more detailed discussion on the comparison with previous templates, and the scatter for $L_{\rm TIR}$ and SFR when estimated using a single band.

[3] https://salims.pages.iu.edu/gswlc/
[4] https://salims.pages.iu.edu/bosa/

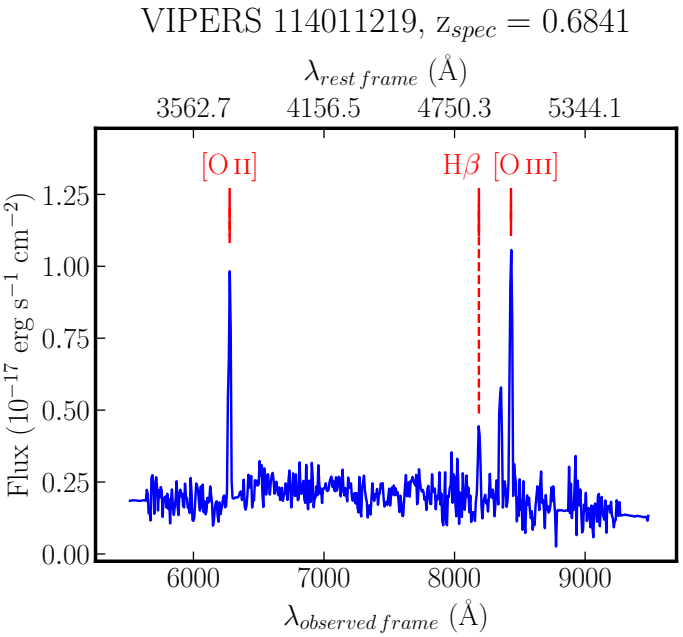


Fig. 1. Exemplary spectrum of a VIPERS star-forming galaxy based on the BPT diagram, at the median redshift of our sample. Line measurements of all four emission lines ([O II]λ3727, Hβ, and [O III]$\lambda\lambda$4959,5007) are considered to be reliable based on the catalog flags (flag 1112, see text).

In this work, we made use of GSWLC-A2.1, an updated version[5] (Salim, priv. comm.) of the current GSWLC-A2 public catalog, with a total of 640 659 objects (Salim et al. 2018).

3. Data preparation and methodology

3.1. Selection of sources

3.1.1. VIPERS

The VIPERS PDR-2 catalog (Scodeggio et al. 2018) contains galaxies, AGNs, and stars, which can be either primary objects (main targets of the survey) or secondary objects (targets falling into main targets slits), each of them having an associated redshift and a redshift flag ($z_{\rm flag}$). The first step of the selection consists in excluding stars from our sample by setting a lower limit on the redshift and broad-band AGNs based on the specific VIPERS $z_{\rm flag}$. In addition, we required a well-defined spectroscopic redshift ($3 < z_{\rm flag} < 4.5$, confidence level on the redshift estimation at the level of 99%). We also chose to include secondary objects in our sample, with the same criteria for the redshift quality, under the condition that these objects fulfill the same constraint used to select the main target galaxies ($17.5 < i_{AB} < 22.5$ mag).

The second step of the selection is based on the detection of the lines observed in VIPERS: Hβ, [O II]λ3727, and [O III]$\lambda\lambda$4959, 5007 (see Fig. 1 for a typical spectrum of VIPERS star-forming galaxies close to the median redshift). In the catalog, the quality of line detection and fitting is characterized by four criteria: the difference between the observed and Gaussian peak should be lower than 7 Å (flag x), the full width at half maximum should be between 7 and 22 Å (flag y), the difference between the observed and Gaussian amplitude should be <30%

[5] This version uses updated SDSS filters while Fukugita et al. (1996) filters were used in the previous ones.

Table 1. Number of VIPERS galaxies after each selection and for both fields.

Field	VIPERS galaxies	$3.0 \leq z_{\rm flag} \leq 4.5$	Flag(Line)≥1111	% of total
$W1$	57970 (+287)	35221 (+152)	3407 (+11)	5.8%
$W4$	28112 (+243)	16301 (+106)	1371 (+6)	4.8%
$W1 + W4$	86082 (+530)	51522 (+258)	4778 (+17)	5.5%

Notes. The numbers in brackets correspond to the secondary objects observed by VIPERS. The first column describes the field, and the second column shows the number of primary and secondary galaxies on that field. The third column shows the number of galaxies after the cut for the redshift range, while the fourth shows an additional cut for the quality of the line measurements. The last column presents the final percentage of the initial sample used for this work. The initial VIPERS galaxies sample (first column) is defined so that: (1) stars are removed; (2) galaxies have redshift measurements ($1 < z_{\rm flag} < 29.5$); and (3) the i-band flux of secondary galaxies respects the same constraint as target galaxies ($17.5 < i_{\rm AB} < 22.5$). This sample represents all of the potential galaxies that could have ended up in our final sample. See Guzzo & VIPERS Team (2013) and Scodeggio et al. (2018) for the explanation of the flag system.

(flag z), the signal-to-noise (S/N) ratio of the flux or S/N ratio of the equivalent width (EW) should be higher than seven and three, respectively (flag $t = 1$), or 3.5 and eight, respectively (flag $t = 2$). The flags are equal to 1 (for xyz) if the condition is fulfilled and 0 otherwise.

In this work, we selected galaxies having flags higher or equal to 1111, considered reliable in VIPERS. Taking $t = 1$ instead of $t = 2$ increases the size of our sample by 1015 additional galaxies. This selection affects, in particular, the weakest lines [O III]λ4959 (699 galaxies with flags 1111) and Hβ (440 galaxies), but much less [O III]λ5007 (21 galaxies) and [O II]λ3727 (six galaxies).

We ended up with a sample of 4795 galaxies with well-defined redshift and lines measurements. The number of primary and secondary galaxies for the $W1$ and $W4$ fields after each selection step is shown in Table 1.

To select the star-forming galaxies, we used the blue BPT diagram (Baldwin et al. 1981; Lamareille 2010) based on the [OII]λ3727, [OIII]λ5007, and Hβ spectral lines. Contrary to the original BPT diagram, based on [NII], [OIII]λ5007, Hβ, and Hα, which is insensitive to reddening because these lines are relatively close to each other, the blue BPT diagram is affected by extinction, in particular for the [OII]λ3727/Hβ ratio. We used the equivalent width instead of fluxes of the emission lines (only for the purpose of selecting our sample of star-forming galaxies), which significantly reduced the dependence on reddening (Lamareille 2010; Bongiorno et al. 2010). Another effect to take into account is the absorption by the stellar photosphere to the $n = 2$ level for Balmer lines (Hopkins et al. 2003; Tremonti et al. 2004; Davies et al. 2016), which reduces the equivalent width of the line by a few Å. This value depends on the temperature and gravity of the stars in the galaxy and can go up to 15 Å (Groves et al. 2012). To correct Hβ for Balmer absorption, we assumed a general value of $\mathrm{EW}_c = 2$ Å (Miller & Owen 2002; Goto et al. 2003) (increasing the flux by 20% in average), our sample being composed of blue galaxies with strong emission lines by construction.

Figure 2 (left) shows that the BPT diagram accounts for two composite regions where star-forming galaxies and Seyfert 2, and star-forming galaxies and low-ionization nuclear emission-line regions (LINERs) are mixed. The star-forming and Seyfert 2 composite region should be dominated by star-forming galaxies (up to 30% of Seyfert 2 in Lamareille 2010) so we decided to include this region in our star-forming sample as it increases the number of galaxies by a factor of two. In the same way, we considered the star-forming and LINERs composite region located inside the star-forming region as occupied by star-forming galaxies. The number of galaxies in each category is given in Table 2.

We note that the selection of star-forming galaxies might be different at higher redshifts because of the evolution of the [OIII]λ5007/Hβ ratio. An increase in this ratio was observed at $z > 1$ (e.g., Kewley et al. 2013; Holden et al. 2016) and confirmed by Steidel et al. (2014) at $z \sim 2.3$. The evolution of [OIII]λ5007/Hβ between $0.2 < z < 0.6$ is on the order of 0.2 to 0.3 dex, and is due to an increase in the ionization parameter (Kewley et al. 2015), in agreement with models of ionization parameter and ionization parameter + ISM pressure evolution (Cullen et al. 2016). As a result, some of the star-forming galaxies would be shifted at a higher position in the BPT diagram, leading to a reduction of the star-forming sample and contamination by AGNs. Nevertheless, we are confident as this blue BPT diagram was already used to classify VVDS galaxies up to $z \sim 0.8$ (Lamareille et al. 2009; Lamareille 2010).

The relations between M_* and SFR, the so-called main sequence (MS), in terms of the different selections applied to obtain the VIPERS star-forming galaxies is plotted in Fig. 2 (right). This is the selection of the lines that significantly affects the distribution of galaxies in the SFR-M_* space and biases our sample toward more active galaxies for which $\log(\mathrm{SFR}) > -1$. The SFR and M_* values used in Fig. 2 (right) are public and were obtained from the SED fitting with *hyperz* (Davidzon et al. 2013). Several stripes can be seen, and are particularly visible at low SFR. They are due to the low number of templates used in the SED fitting process, and degeneracies between the SED templates and the physical properties of the galaxies. This leads to a poorer estimation of the physical parameters. For this reason and for consistency with the GSWLC catalog, we reconstructed the SED of galaxies using the CIGALE code (see Sect. 3.2). Nonetheless, this reconstruction was performed only for the star-forming sample, as it is the main sample studied in this paper.

3.1.2. GSWLC

To construct the sample of low-redshift galaxies, we made use of the catalog flags quantifying the quality of the SED, the UV, and MIR data availability, and data the belonging to the SDSS main galaxy sample (MGS). We first selected a subsample of galaxies with good SEDs (no broad-line spectrum, no missing SDSS photometry, and an SED fitting characterized by a reduced χ^2 ($\chi^2_{\rm red}$) less than 30). This high $\chi^2_{\rm red}$ value was chosen since the SFR and M_* of galaxies below this limit differ by less than 0.1 dex in comparison with Brinchmann et al. (2004). Despite this good agreement, SED with $\chi^2_{\rm red} > 5$ should be approached with caution (Salim et al. 2016). Therefore, we decided to exclude them (5.8%, 5655 galaxies) from the final analysis. Additionally, we selected only galaxies with GALEX FUV-NUV measurements,

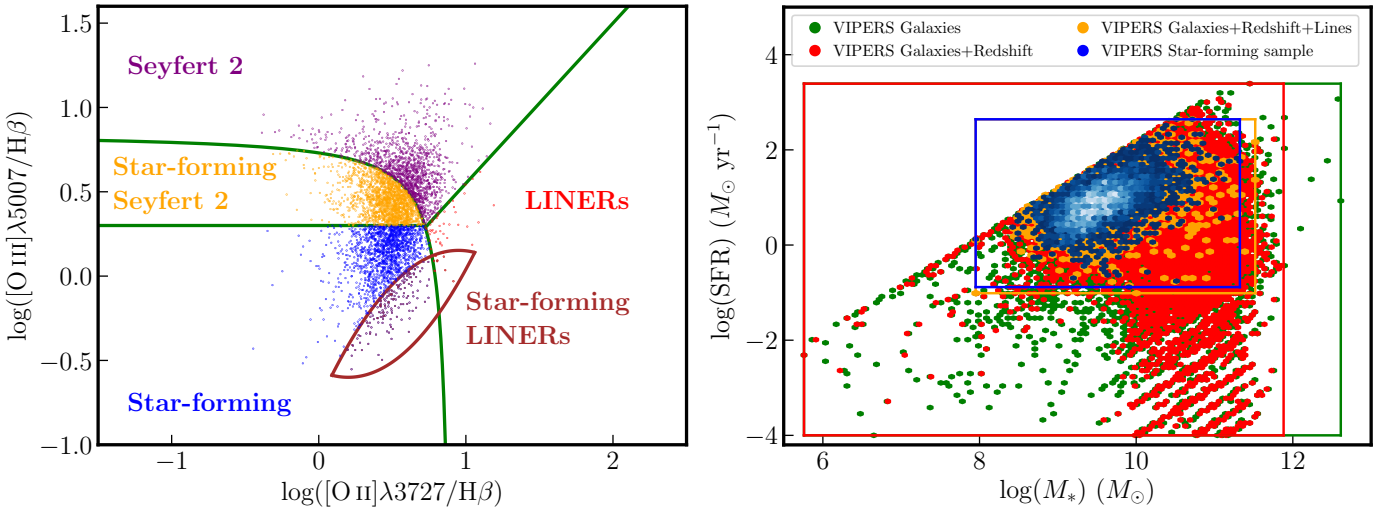


Fig. 2. Distribution of VIPERS galaxies throughout the selection process. *Left panel*: BPT diagram for the sample of VIPERS galaxies. Star-forming (blue), Star-forming/Seyfert 2 composite (yellow), and Seyfert 2 (purple) galaxies, and LINERs (red), and star-forming/LINERs composites (brown) are separated by green lines whose equations are given in Lamareille (2010). *Right panel*: SFR versus M_* for VIPERS galaxies after each selection (SFR and M_* are estimated using *hyperz* in this plot): all galaxies (green), selection on redshift (red), on lines (orange), and star-forming sample (blue). Visible green, red, and orange points therefore represent galaxies excluded after each selection. Rectangles represent the extent in SFR and M_* after each selection.

at least one WISE-3/WISE-4 measurement (to better constrain the IR part of the SED, see Sect. 2.2) for which the derived $L_{\rm TIR}$ is not contaminated by AGN, and which are part of the MGS. This selection was made in order to have a very good wavelength coverage and to allow for the best SED fitting and parameter estimations with CIGALE. Unfortunately, it is not possible to obtain such excellent wavelength coverage for VIPERS and to have a significant sample at the same time. It follows that the estimated parameters for VIPERS are more dependent on templates than GSWLC.

The lines measurements were obtained by cross-matching the GSWLC catalog with the MPA-JHU catalog[6]. In total, 99.8% of the GSWLC subsample has a counterpart in the MPA-JHU catalog. The MPA-JHU catalog already accounts for foreground Galactic reddening corrections using O'Donnell (1994). To create a reliable sample of star-forming galaxies, we followed Tremonti et al. (2004) and selected galaxies with a $S/N > 5$ for Hα, Hβ and [N II], and a $S/N > 3$ for [O III]λ5007 detections. We selected the star-forming galaxies using the BPT diagram (Baldwin et al. 1981) and the more restrictive limit established by Kauffmann et al. (2003) (see Fig. 3 left). From 93 605 galaxies with good lines measurements, 92 696 selected objects are star-forming galaxies and 909 are Seyfert galaxies or LINERs.

We note that only a few galaxies are classified as Seyferts or LINERs in the BPT diagram (red dots) and most of them are at the edge of the Kauffmann et al. (2003) limit. This apparent lack of Seyferts and LINERs comes from the previous step when the selection of galaxies based on the WISE-3 and WISE-4 measurements availability was performed: galaxies for which the WISE-based $L_{\rm TIR}$ was corrected for AGN emission (flag 6 and 7 in GSWLC) were already removed. The galaxies close to the Kauffmann et al. (2003) limit were not removed, probably because they showed no or weak signs of AGN emission. These galaxies, removed in the previous selection step (17 029 galaxies), are shown in Fig. 3 (purple dots).

For consistency, we applied a cut in M_* for the GSWLC star-forming sample to match the M_* range of the VIPERS sample ($8.8 < \log(M_*) < 11.4\ M_\odot$). We remind the reader that this range of M_* is slightly different compared to what is seen in Fig. 2 (right) because new M_* estimations were obtained using CIGALE.

We ended-up with a GSWLC main sample of 91 533 star-forming galaxies. We also defined a [O II] sample where a selection criteria was also applied to [O II] ($S/N > 5$, 48 845 galaxies, referred as the [O II] sample) and a second one with an additional selection for [O III]λ4959 ($S/N > 3$, 35 456 galaxies, referred as the [O II]+[O III] sample). These two subsamples will be used when estimating the SFR from [O II] and when using the metallicity. The detailed selection is shown in Table 3.

As for VIPERS, we show the effects of the different selections applied to GSWLC in Fig. 3 (right). Selection on the FUV and NUV measurements removed part of the red passive galaxies as these fluxes trace the emission from young high-mass stars. This is the selection of star-forming galaxies that removed the major part of the low-SFR galaxies. While we have a comparable mass range, the average SFR of the VIPERS sample is higher than GSWLC, as is expected from younger star-forming galaxies.

Table 2. Number of VIPERS galaxies in each of the classes defined by the BPT diagram of Lamareille (2010).

Class	Number
All	4795
Star-forming	1633
Star-forming/Seyfert 2	1824
Seyfert 2	1286
LINERs	52
Star-forming/LINERs [(1)]	176
Our work	3457

Notes. [(1)]The star-forming/LINERs galaxies are classified either as star-forming galaxies or LINERs.

[6] https://wwwmpa.mpa-garching.mpg.de/SDSS/DR7/

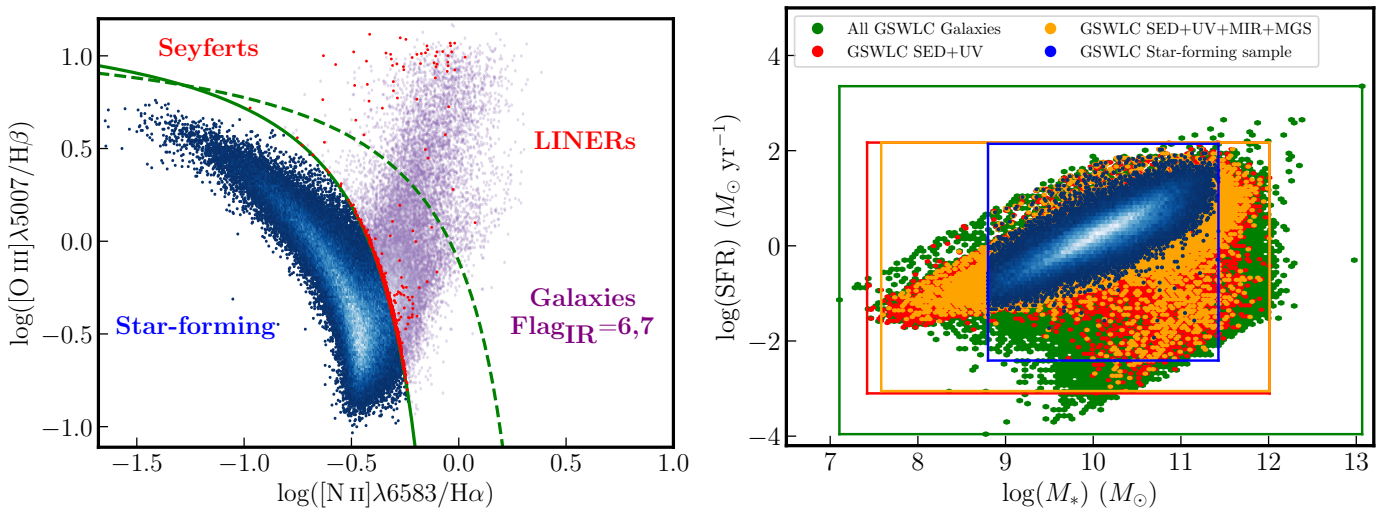


Fig. 3. Distribution of GSWLC galaxies throughout the selection process. *Left panel*: BPT diagram for the sample of GSWLC galaxies. The separation between Seyfert and LINERS (red points), and star-forming galaxies (blue to white density plot) is represented by the green curve (Kauffmann et al. 2003), while the dashed-green line represents the limit from Kewley et al. (2001). Galaxies for which $L_{\rm TIR}$ was corrected for AGN emission (and previously removed based on the GSWLC flags) are shown for information (purple to white density plot). *Right panel*: SFR versus M_* for GSWLC galaxies for each selection: all GSWLC galaxies (green), selection on the quality of the fits, χ^2_r, and availability of GALEX measurements (red), selection on MIR measurements from which $L_{\rm TIR}$ is not contaminated by the AGN component and belonging to the MGS (orange), and the star-forming sample (blue). Visible green, red, and orange points therefore represent galaxies excluded after each step. Rectangles represent the extent in SFR and M_* after each selection.

Table 3. Number of GSWLC galaxies after the different selection steps.

Catalog flags	Initial catalog 640 659	Good SED ($\chi^2_r < 5$) 595 586	GALEX data 209 628	L_{IR}-WISE 154 623	MGS 149 712
Lines S/N	Cross-correlation MPA-JHU 149 374			S/N selection 93 605	
BPT diagram	Star-forming galaxies 92 696			Seyfert – LINERs 909	
	Mass cut ($8.8 < \log(M_*) < 11.4\ M_\odot$)				
Final samples	Main sample 91 533			[O II] sample / [O II]+[O III] sample 48 845/35 456	

3.2. CIGALE

As we discussed in the previous section, the public main physical parameters obtained for VIPERS galaxies with *hyperz* suffer from the low number of templates used in the SED reconstruction (see Fig. 2 right). To improve them, we used CIGALE (Boquien et al. 2019). Based on flux measurements from UV to radio, CIGALE reconstructs the SED of galaxies based on templates built with different modules: the SFH (e.g., exponential, delayed, periodic), the stellar populations library (Bruzual & Charlot 2003; Maraston 2005), the dust attenuation model (Calzetti et al. 2000; Charlot & Fall 2000 or general double power laws, see Buat et al. 2011a; Lo Faro et al. 2017 for instance), the dust emission model (e.g., Draine et al. 2007, 2014; Casey 2012; Dale et al. 2014; Jones et al. 2017), the AGN contribution (e.g., Fritz et al. 2006; Baes et al. 2011; Stalevski et al. 2012, 2016; Camps & Baes 2015), and the radio emission.

Usually, the estimation of physical parameters is obtained from the best SED template. However, galaxies with different properties can have similar SEDs and the best template does not provide information about such uncertainties. To obtain more realistic values of the physical parameters, along with an estimation of the associated uncertainties, CIGALE employs a Bayesian analysis (Noll et al. 2009; Boquien et al. 2019). Instead of taking the best SED only, CIGALE selects a subsample of the best templates, each of them being weighted by their likelihood (which depends on χ^2). The Bayesian parameters and uncertainties are therefore the likelihood-weighted means and likelihood-weighted standard deviations of the parameters, which are more representative of the true nature of the galaxies compared to the parameter derived using the best template only.

The SED fitting of galaxies strongly relies on the chosen SFH (Pforr et al. 2012; Cassarà et al. 2016) and is hard to constrain from broad-band SED fitting, even with good measurements in the UV and optical part of the spectrum. The MS SFH is well defined by a function depending on the seed mass of the galaxy (Ciesla et al. 2017). This analytical form is, however, difficult to use as the SFH parameters cannot be reliably estimated using broad-band SED fitting techniques. Modeling the variations of the SFR within the scatter of the MS would require additional free parameters in this analytical form, making it complicated to use in SED modeling. The SFR is, however, relatively well-estimated based on the SFH models used in

Table 4. Modules and parameters of the CIGALE run for VIPERS galaxies.

Parameters [(1)]	Values
Star formation history: SFH delayed + quench/burst	
$\tau_{\rm main}$: e-folding time of the main stellar population (Gyr)	4, 5, 6, 7, 8, 9, 10, 13
age$_{\rm main}$: Age of the main stellar population in the galaxy (Gyr)	5, 5.5, 6, 6.5, 7
age$_{\rm burst}$: Age of the burst/quench episode (Myr)	10, 50, 100, 150, 200, 300, 450
$r_{\rm SFR}$: Ratio of the SFR after/before $age_{\rm burst}$	1, 1.6, 2.1, 2.7, 3.3, 3.9, 4.4, 5
Stellar population models: Bruzual & Charlot (2003)	
IMF	Chabrier (2003)
Z: metallicity	$Z_\odot$
age$_{\rm sep}$: Age of the separation between the young and the old star populations (Myr)	10
Dust attenuation law: Charlot & Fall (2000)	
A_V_BC: V-band attenuation in the birth clouds (mag)	0,0.2,0.4,0.6,0.8,1,1.2,1.4,1.6,1.8,2
BC_to_ISM_factor: A_V_ISM / A_V_BC	0.8
$\alpha_{\rm BC}$: Power law slope of the attenuation in the birth clouds	−0.7
$\alpha_{\rm ISM}$: Power law slope of the attenuation in the ISM	−0.7
Dust emission: Draine et al. (2007, 2014)	
$q_{\rm PAH}$: Mass fraction of PAH	1.77, 2.5, 3.19
$U_{\rm min}$: Minimum radiation field	10, 15, 25
α: Powerlaw slope dU/dM propto U^α factor	2
γ: Fraction illuminated from $U_{\rm min}$ to $U_{\rm max}$	0.02

Notes. [(1)]See Ciesla et al. (2016), Boquien et al. (2019).

the literature. Ciesla et al. (2017) proposed an SFH composed of a delayed SFH (for $t < t_0$), followed by a recent quench or burst (for $t > t_0$) equal to $r \times \mathrm{SFR}(t = t_0)$, where r represents the strength of the quench ($r < 1$) or burst ($r > 1$), giving good estimations of the SFR for several galaxy types at different redshifts. In this paper, we made use of this SFH but we discarded the possibility of a quench as our sample is composed of star-forming galaxies. Moreover, we wanted to keep the process of SED fitting as simple as possible, without modeling possible starburst galaxies during the quenching period, and limited photometric coverage of VIPERS galaxies would not allow for such a detailed study. We underline again that the choice of a particular SFH can have a certain impact on the derived properties from SED fitting, and more explanations about the difference between SFH models used in SED fitting, as well as the construction of this delayed SFH plus a quench or burst, can be found in Ciesla et al. (2017).

To take into account the emission lines due to the ionization from high-mass stars radiation, we included the nebular module based on CLOUDY13.01 models (Inoue 2011; Ferland et al. 2013), which takes into account 124 lines from He II λ30.38 nm to N II λ205.4 nm. Nebular emission is important for active star-forming galaxies because it also contributes to the continuum emission, and therefore has a certain impact on the galaxies' SEDs. In this module, we assumed that the Lyman continuum photons are not escaping the galaxy and are not absorbed by the dust.

The choice of a dust attenuation law (Charlot & Fall 2000; Calzetti et al. 2000 and modified versions) has no significant impact on the derivation of the SFR or $L_{\rm TIR}$ (Buat et al. 2011a; Lo Faro et al. 2017; Małek et al. 2018) but can influence the estimation of M_*. We chose the Charlot & Fall (2000) attenuation law as it is often used in other works and gives good results when compared to radiative-transfer models (Buat et al. 2018). We used the Bruzual & Charlot (2003) stellar population models and the dust emission templates of Draine et al. (2007) with updates from Draine et al. (2014). As most of the AGNs should be excluded from our sample, we did not include any AGN modules, allowing us to save computational time. The modules and parameters used in CIGALE are shown in Table 4. In addition, the rest-frame luminosities, and hence the k-corrected values, were obtained using the *restframe_parameters* module of CIGALE through a Bayesian approach.

The optical data from CFHTLS were cross-matched with GALEX, WIRCam-K$_s$, VIDEO-K$_s$ (W1 field only), WISE and *Spitzer* data (W1 field only). A detailed description of the VIPERS multiwavelength catalog construction can be found in Moutard et al. (2016a,b). Photometric data were corrected from reddening using the Schlegel et al. (1998) dust maps. This correction is small as $E(B-V)$ is, on average, equal to 0.03 and 0.05 for the W1 and W4 fields, respectively. In addition, we complemented the catalog with *Herschel* measurements (W1 field only) from the HELP database (Shirley et al. 2019, 2021) using a cross-matching radius of 1″.

We chose to not include the spectral lines' fluxes in the SED reconstruction of the galaxies. In this way, the line measurements remained independent from the CIGALE SFR estimations, contrary to rest-frame luminosity estimations, which depend on the templates used. All measurements located below the Lyman break (λ = 912 Å) in the rest-frame were discarded as CIGALE is not optimized to handle them: FUV measurements for galaxies at $z > 0.698$ (140 galaxies, 4%) were discarded.

In the case of the 351 galaxies for which a counterpart was found in the AllWISE catalog, 33% of WISE-2, 53% of WISE-3, and 86% of WISE-4 detections were upper limits and were considered as such during the SED fitting. In addition, since the WISE-3 and WISE-4 conversion from magnitudes to fluxes were uncertain by 10% (Wright et al. 2010), we increased the flux uncertainties by 10% in the SED fitting process for these two bands.

Most of the *Herschel* measurements have a $S/N < 3$ but their associated uncertainty is large enough so that these data do not significantly impact the SED reconstruction. The comparison of SFR and M_* for a run with and without *Herschel* data is found to be on the order of ∼0.03 dex. All the different bands used in

Table 5. VIPERS photometric data used in CIGALE.

Band	Wavelength	Available measurements	$S/N > 3$ (%)
GALEX FUV	1549.0 Å	415	78.8
GALEX NUV	2304.7 Å	2114	98
CFHT u	3884.7 Å	3453	99.9
CFHT g	4804.1 Å	3457	100
CFHT r	6207.9 Å	3457	100
CFHT i	7498.3 Å	3457	100
CFHT z	8815.0 Å	3457	99.9
CFHT K_s	2133.78 nm	3189	99.5
VISTA K_s	2137.66 nm	583	99.6
WISE-1	3.4 µm	351	100
WISE-2	4.6 µm	234, 117 (1)	74.1
WISE-3	12 µm	163, 188 (1)	59.5
WISE-4	22.8 µm	49, 302 (1)	14.3
Spitzer IRAC1	3.6 µm	533	100
Spitzer IRAC2	4.5 µm	320	100
Spitzer IRAC3	5.8 µm	41	100
Spitzer IRAC4	8 µm	35	100
Spitzer MIPS1	24 µm	150	100
Spitzer MIPS2	70 µm	15	100
Spitzer MIPS3	160 µm	1	100
Herschel PACS-Green	100 µm	441	2.9
Herschel PACS-Red	160 µm	441	6.8
Herschel SPIRE-S	250 µm	441	20.6
Herschel SPIRE-M	350 µm	441	7
Herschel SPIRE-L	500 µm	441	1.8

Notes. (1)Detections and upper limits. The S/N column takes into account detections only.

the CIGALE run and the number of available measurements are listed in Table 5.

To check the reliability of the SED fitting of CIGALE, one can refer to the reduced χ^2 associated with each SED (median value of 1.2). However, quantifying the quality of an SED using its χ^2 is not straightforward due to the nonuniform number of bands used in the SED fitting (Małek et al. 2018).

Another way to estimate the reliability of the SED fitting is to create a mock catalog for which the true physical parameters are known and recovered using the same initial configuration (see Table 4). The comparison between the recovered parameters and estimated parameters in our CIGALE run characterizes the accuracy of the SED fitting. This process is automatically implemented in CIGALE (Giovannoli et al. 2011; Boquien et al. 2019) and the results are presented in Fig. A.1 for $L_{\rm TIR}$, SFR, M_*, and the attenuation for Hβ, [O II], and [O III]. For the CIGALE run presented in this work, we observed that the recovered physical parameters are in good agreement with the input ones.

Figure 4 shows the comparison between the stellar mass and SFR estimations from CIGALE and *hyperz*. While SFR estimations seem to agree, although there is a large scatter, the M_* comparison shows an offset with an overestimation in CIGALE, or an underestimation in *hyperz*. For the SED fitting of VIPERS galaxies (Davidzon et al. 2013), *hyperz* uses the Bruzual & Charlot (2003) stellar population models, a Chabrier (2003) IMF, an exponentially declining or constant SFR, Calzetti et al. (2000) or Prevot et al. (1984), Bouchet et al. (1985) attenuation laws, and a metallicity $Z = 0.2Z_\odot$ or $Z = Z_\odot$.

We performed a run using a Calzetti et al. (2000) attenuation law to estimate the offset in M_* as compared to Charlot & Fall (2000). The M_* is systematically higher using the Charlot & Fall (2000) recipe, by 0.1−0.2 dex at all stellar masses. This is in agreement with Małek et al. (2018) and Buat et al. (2019), who found that a Charlot & Fall (2000) attenuation law led to higher M_* compared to Calzetti et al. (2000) by a factor of 1.5 and 1.7, respectively. To confirm that dust is one of the main reason for this offset, we performed an additional run based on the Charlot & Fall (2000) recipe and compared red and blue galaxies, and found that the offset in M_* was larger for blue than for red galaxies.

Using exponentially declining or delayed+burst SFHs, Ciesla et al. (2017) showed that the mean error on SFR between both estimations is close to 0, which is what is observed in Fig. 4. Both SFH prescriptions are found to recover the M_* with an error lower than 25%. Based on Fig. 11 of Ciesla et al. (2017), we estimated that the offset could reach 0.11 dex between both estimations.

We also performed a run using $Z = 0.2Z_\odot$. This does not significantly impact the SFR, while the M_* is slightly lower at low M_* by ∼0.06 dex.

To summarize, these three different parameters, in particular the dust attenuation recipe, do not significantly impact the derivation of the SFR but can lead to a different M_* estimation with a scatter of ∼0.3 dex, comparable to the offset observed in Fig. 4 (right).

To check our choice of stellar absorption correction (EW = 2 Å), we compared the estimated flux of the Hβ emission line from CIGALE (without stellar absorption) and from observations (stellar absorption not corrected). When a single value for the stellar absorption is used, as in this work, a correction ranging from 2 to 4 Å in EW applied to the observed line fluxes gives a good agreement with estimated fluxes from CIGALE.

3.3. Dust-attenuation correction

To correctly estimate the properties of a galaxy, dust attenuation has to be taken into account in order to recover the unattenuated flux, especially toward the bluer part of the spectrum where this effect is significant. The relation between the intrinsic (unattenuated or dust-free) and observed (attenuated) fluxes, $F_{\rm int}$ and $F_{\rm obs}$, respectively, is defined as:

$$F_{\rm int} = F_{\rm obs} \times 10^{0.4A(\lambda)} = F_{\rm obs} \times 10^{0.4k(\lambda)E(B-V)} \quad (1)$$

where $E(B-V)$ is the color excess between the B and V bands, $A(\lambda)$ is the attenuation at λ (in mag), and $k(\lambda)$ is the attenuation curve. Estimations of $A(\lambda)$ for each continuum band and spectral line were obtained through CIGALE for VIPERS. From [O III]λ5007 to [O II]λ3727, the average attenuation applied to $F_{\rm obs}$ ranges from 1.2 to 1.5 mag.

GSWLC does not provide the attenuation correction for the lines but only for the FUV and NUV bands. To estimate this correction, we used the Balmer decrement technique, which links the Hα/Hβ ratio to the attenuation at different wavelengths:

$$A(\lambda) = k(\lambda) \times \frac{-2.5}{k(\mathrm{H}\beta) - k(\mathrm{H}\alpha)} \log\left(\frac{(\mathrm{H}\alpha/\mathrm{H}\beta)_{\rm int}}{(\mathrm{H}\alpha/\mathrm{H}\beta)_{\rm obs}}\right), \quad (2)$$

where $(\mathrm{H}\alpha/\mathrm{H}\beta)_{\rm int}$ corresponds to the theoretical ratio in the dust-free case, and $(\mathrm{H}\alpha/\mathrm{H}\beta)_{\rm obs}$ is the observed ratio where Hα and Hβ are corrected for stellar absorption. For the theoretical ratio, we used the case B recombination with $T = 10^4$ K and $n_e = 10^2$ cm^{-3} equal to 2.86. This value is widely used

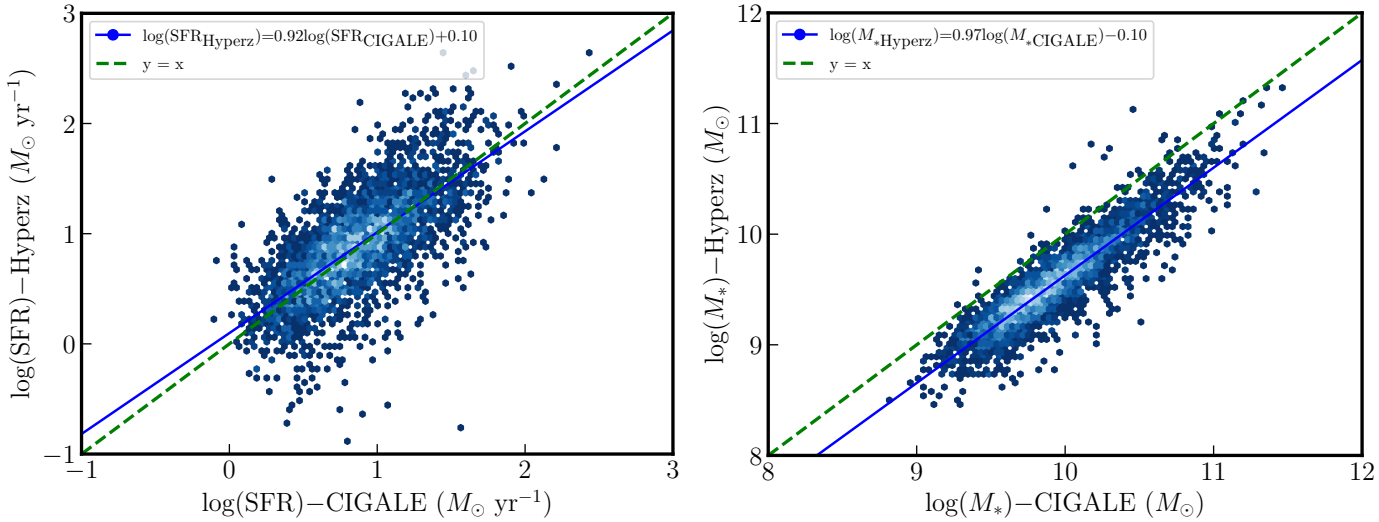


Fig. 4. Comparison between the main physical properties estimated using *hyperz* and CIGALE tools. *Left*: SFR derived using *hyperz* versus SFR derived using CIGALE. There is a good agreement between both estimations (0.03 dex), although there is a significant scatter (0.32 dex). *Right*: M_* derived using *hyperz* versus M_* derived using CIGALE. The scatter is smaller than for the SFR (0.17 dex) but an offset of 0.37 dex is observed. Such an offset arises from the different attenuation laws used between *hyperz* (Calzetti et al. 2000; Prevot et al. 1984; Bouchet et al. 1985) and CIGALE (Charlot & Fall 2000). The different SFHs and metallicity used may also be possible reasons for the increase in the M_* in CIGALE.

to determine the dust attenuation correction from the Balmer decrement, although the true value might be in between the case A and B recombination (e.g., Groves et al. 2012). For $k(\lambda)$, we used a Milky Way reddening law (e.g., Cardelli et al. 1989; O'Donnell 1994) with $R_V = 3.1$ and corrected the Hα, Hβ, [O III]$\lambda\lambda$4959,5007, and [O II]λ3727 emission lines, for which the average attenuation ranges from 0.8 to 1.4 mag.

4. Analysis

In this section, we tested different relations proposed in the literature for UV, u, 8- and 24-μm bands, L_{TIR}, and spectral lines. In the following, all luminosities are in the rest-frame and are estimated from CIGALE. For each calibration, we computed the coefficients of the linear fit and the Pearson coefficient between the SFR from CIGALE and the SFR estimated using the calibration. The mean and scatter are estimated as the mean and standard deviation of the difference of the log(SFR), respectively. All this information can be found in Appendix E.

We point out that the scatter derived from VIPERS fits is not completely representative. For the VIPERS sample, we do not have enough data in the MIR and FIR range of galaxy spectrum to constrain the precise value of the dust attenuation. As a consequence, dust attenuation is low (A_V peaking around 0.4), which results in an almost negligible change of estimated SFR based on the optical data only or the full range of the optical part of the spectra. We checked the impact of the wavelength coverage on the rest-frame luminosity by performing a dedicated test, described in Sect. 5.1.

4.1. SFR from continuum bands

4.1.1. Ultraviolet indicators

The UV emission of galaxies is dominated by the radiation from young high-mass stars. Due to their short lifetime, their UV radiation represents an excellent tracer of star formation with a timescale of ∼100 Myr. The main drawback is the dust attenuation, which is particularly significant at this wavelength. Either a correction is applied based on an attenuation law (Charlot & Fall 2000; Calzetti et al. 2000), or an IR band is used as a proxy representing the re-emitted UV flux absorbed by the dust (see Sect. 4.1.4). In this section, we focused only on the UV bands and used the calibrations of Rosa-González et al. (2002), Salim et al. (2007), Davies et al. (2016), and Brown et al. (2017), written in Appendix. B.1.

In Brown et al. (2017), the dust attenuation is corrected following two prescriptions, both using the FUV and NUV magnitudes of the galaxies. The first is characterized by $(M_{FUV} - M_{NUV})_{dust\ free} = 0$ and a Calzetti et al. (2000) extinction law, while the second assumes $(M_{FUV} - M_{NUV})_{dust\ free} = 0.022$ and the prescription of Hao et al. (2011). SFRs from FUV corrected with these two prescriptions are presented in Fig. 5. The SFR obtained using the Calzetti et al. (2000) attenuation law underestimates the SFR at low luminosity for VIPERS, while there is a relatively good agreement with GSWLC but with a high scatter. Such small discrepancies could originate from the use of different attenuation laws in CIGALE: Charlot & Fall (2000) for VIPERS and a modified Calzetti et al. (2000) for GSWLC. On the contrary, the Hao et al. (2011) attenuation recipe gives a better agreement with CIGALE SFR estimations and a smaller scatter with GSWLC.

Davies et al. (2016) computed the SFR following different bands, which were then recalibrated using the radiative transfer code of Popescu et al. (2011). To correct for dust attenuation, β_{UV} is estimated from FUV and NUV data (Calzetti et al. 1994) and linked to A_{UV} (Meurer et al. 1999):

$$A_{UV} = 4.43 + 1.99\beta_{UV}. \quad (3)$$

As seen in Fig. 6, the SFR for VIPERS galaxies are underestimated and the SFR for GSWLC galaxies are overestimated at low SFR. Because the calibration of the attenuation from Meurer et al. (1999) is computed at 1600 Å, it should naturally differ from the real attenuation suffered in the NUV. This could partially explain the strong disagreement observed for the NUV-based SFR. A smaller disagreement is also observed for the FUV-based SFR. For both bands, another source of uncertainty might come from our own derivation of β_{UV}, based on

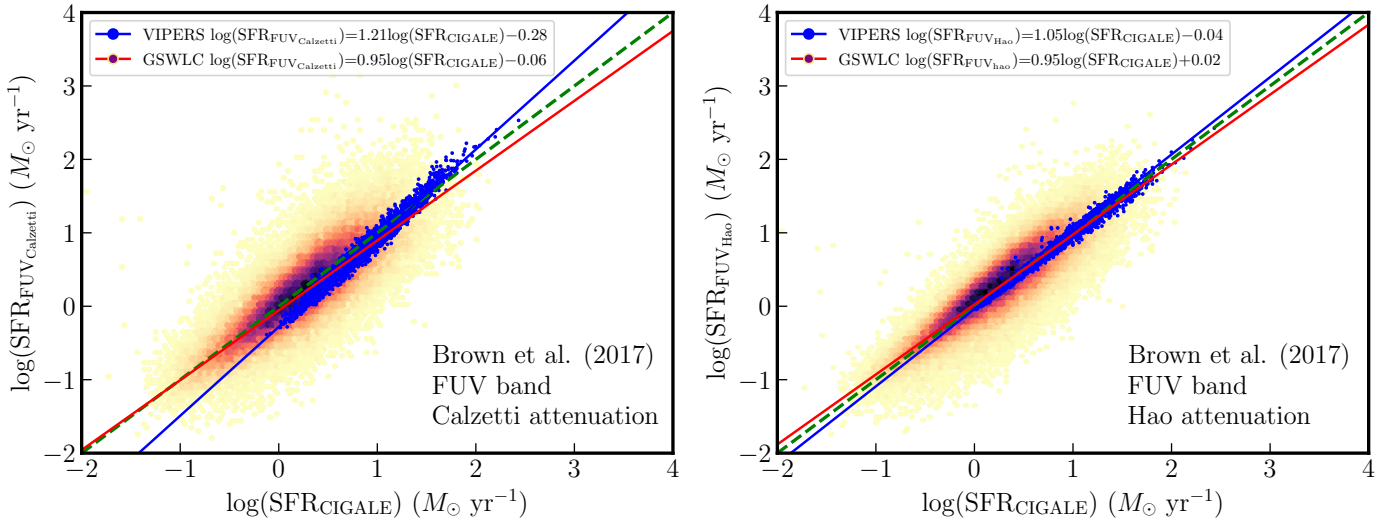


Fig. 5. SFR derived from the relations given in Brown et al. (2017) using GALEX FUV and the attenuation law from Calzetti et al. (2000) (*left*) and Hao et al. (2011) (*right*). Blue points represent the VIPERS galaxies and density hexabin represent the GSWLC galaxies sample. The blue line is the fit for VIPERS galaxies, the red line is the fit for GSWLC galaxies, and the green line is the 1:1 relation. The agreement is better with the Hao et al. (2011) attenuation correction recipe, both for VIPERS (mean and scatter of 0.01 and 0.05 dex) and GSWLC (−0.02 and 0.25 dex), compared to Calzetti et al. (2000) (0.09 and 0.10 dex for VIPERS, 0.02 and 0.30 dex for GSWLC).

L_{FUV} and L_{NUV}, which may be impacted by the templates, in particular for VIPERS.

To obtain a better estimation of the attenuation from β_{UV}, we derived new relations from the SED fitting from rest-frame FUV and NUV bands estimated by CIGALE:

$$A_{FUV} = (1.78 \pm 0.02)\beta_{UV} + (3.71 \pm 0.02), \quad (4)$$

$$A_{NUV} = (1.35 \pm 0.01)\beta_{UV} + (2.80 \pm 0.02). \quad (5)$$

We recall here that β_{UV} and, by extension, A_{FUV} and A_{NUV}, are also dependent on the assumed SFH. The SFH chosen influences the mass distribution and the dominance of high-mass stars, which directly affects the value of β_{UV}. In addition, the stellar evolution may have an impact on β_{UV} within the SFH: after a few dozen Myr, most of the high-mass stars leave the MS and the old stellar population gains more importance relatively to the young population, leading to a decrease in β_{UV} (i.e., it becomes redder). Wilkins et al. (2012) studied the influence of different SFHs on β_{UV} and found an uncertainty of 0.31 for A_{FUV}. In addition, β_{UV} is also affected by the metallicity, with an uncertainty of 0.7 for A_{FUV}.

Despite being recalibrated with the radiative transfer method of Popescu et al. (2011), the SFR calibrations of Davies et al. (2016) are not in good agreement with VIPERS and GSWLC for either band. We were able to recover a better agreement by using Eqs. (4) and (5) and the calibration from Salim et al. (2007), shown in Fig. 7. For GSWLC, the slight deviation may be explained by the use of a different attenuation law to the one used to derive Eqs. (4) and (5). This shows that SFR estimations heavily depend on the method chosen to retrieve the intrinsic luminosity in the UV. Nonetheless, the attenuation given by Eqs. (4) and (5) and based on VIPERS, gives reliable corrections at low redshifts, giving good SFR estimations.

Because the dust attenuation correction might be difficult to derive, Rosa-González et al. (2002) proposed an SFR calibration based on NUV luminosity and for which the attenuation correction Calzetti et al. (2000) was already taken into account. As observed in Fig. C.1 (top-left), using a calibration for which the dust attenuation correction is already included might lead to a high scatter when used on another sample of galaxies. When the average SFR of the VIPERS and GSWLC samples is compared to the estimation from Rosa-González et al. (2002), the SFR differ by 0.11 and 0.20 dex, respectively.

In Figs. 5–7, for instance, and throughout this work, we note that the fits for VIPERS galaxies are steeper than the fits for GSWLC galaxies. Although we made sure to select the same type of galaxies at low and intermediate redshifts, the wavelength coverage for GSWLC was better than that of the VIPERS galaxies in the IR bands. This in turn affects the SFRs when estimating them from the panchromatic coverage using the balanced SED. In such SED fitting tools, SFRs are sensitive to IR emission in particular. That is why we focused our efforts on modeling as best as possible the short wavelength fluxes, using carefully chosen SFHs and attenuation, to ensure a more reliable fit in the IR where the photometry was not as good as the short wavelength counterparts. While this method ensures a reliable SFR estimation using the full SEDs, attenuation plays a bigger role in estimating the total SFRs, assuming a more important hidden SFR fraction.

The fact that GSWLC have observations in UV wavelengths, directly tracing young stellar populations in those galaxies, may also partially explain the difference in slopes in Fig. 6, which relies more on templates. However, more direct measurements do not necessarily imply a better agreement with known calibrations, as seen in Fig. 6 for the GSWLC sample.

4.1.2. The *u*-band indicator

The *u*-band can also be used as an SFR tracer but, in addition to significant dust attenuation, it can be more strongly affected by the old stellar population than the FUV and NUV bands (Bell 2003). Moreover, the *u*-band luminosity can vary significantly during the stellar evolution, making it less reliable as an SFR tracer (Hopkins et al. 2003). In this subsection, we

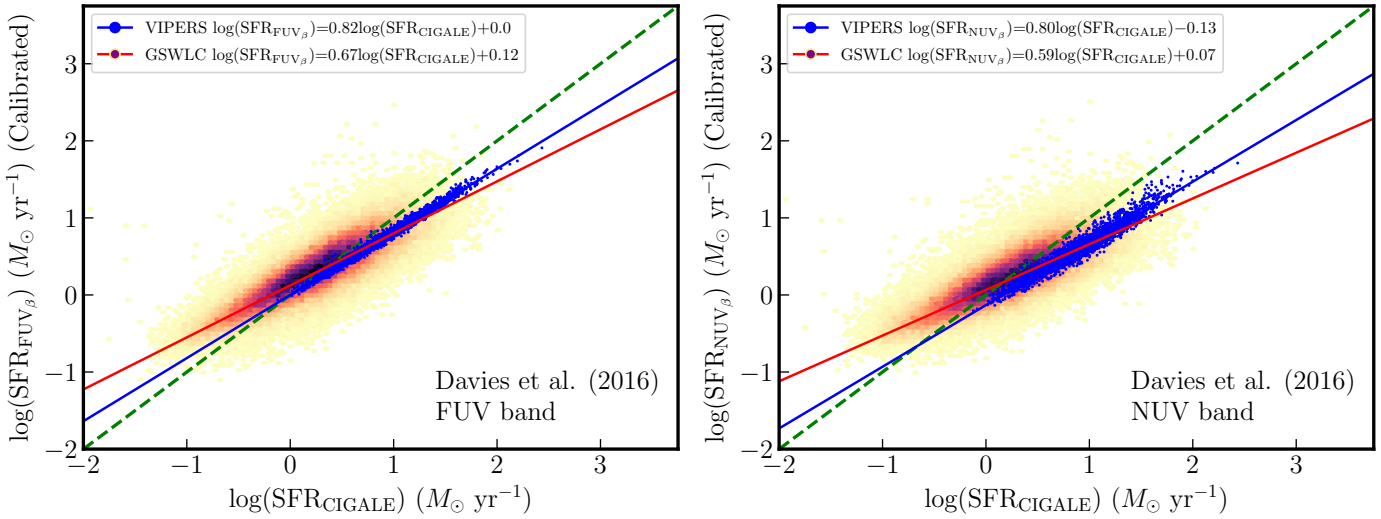


Fig. 6. SFR derived from the relations given in Davies et al. (2016) using GALEX FUV (*left*) and NUV (*right*), and the attenuation law from the $A_{UV} - \beta_{UV}$ relation of Meurer et al. (1999). We observed a disagreement with CIGALE both for VIPERS and GSWLC in the FUV (mean of 0.16 dex and scatter of 0.07 dex for VIPERS, −0.07 and 0.25 dex for GSWLC), stronger in the NUV band (0.29 and 0.10 dex for VIPERS, −0.01 and 0.29 dex for GSWLC).

used the calibrations of Hopkins et al. (2003), Moustakas et al. (2006), Davies et al. (2016), and Zhou et al. (2017), written in Appendix B.2.

Due to our selection criteria, VIPERS and GSWLC are predominantly composed of blue galaxies and the red population should not significantly contaminate the star-forming sample. Using a criterion based on the NUVrK$_s$ diagram (Arnouts et al. 2013), we found no passive galaxies in VIPERS and only 158 in GSWLC (0.2% of the sample). This number of passive galaxies should be taken with caution for GSWLC as this method is not well-constrained at $z = 0$.

However, even for star-forming galaxies, part of the stellar population is composed of old stars that can contaminate the *u*-band. Using CIGALE, we estimated this contamination as the old stellar population (≥100 Myr) to the total stellar luminosity ratio through the *u* filter[7]. The contamination ranges from 16% to 53%, with an average of 36%. This is consistent with the hydrodynamical simulations at $1 < z < 2$ of Boquien et al. (2014), who found that SFR estimations based on the *u*-band overestimates the SFR by ∼39%.

Based on a sample of galaxies with *u* and Hα flux measurements, Hopkins et al. (2003) derived a nonlinear calibration that reflects the change in star formation history and old-stellar population contamination (Fig. 8 left). Despite the assumption of an equivalent old stellar contamination between the sample of Hopkins et al. (2003), GSWLC, and VIPERS, which may not be entirely true, particularly for VIPERS due to the different redshift range, the nonlinear calibration of Hopkins et al. (2003) gives a good estimation of the SFR for VIPERS and GSWLC, without having to perform any additional decontamination.

Davies et al. (2016) derived a linear calibration for the *u*-band where the luminosity is scaled based on the $u - g$ color for $u - g > 0.55$ (reddest galaxies) to account for this old stellar population contamination. This correction concerns 34% of VIPERS galaxies, with an average contamination of 11%, and 99% of GSWLC galaxies, with a much higher average contamination equal to 51%. For some galaxies that are part of GSWLC, this correction leads to negative luminosity and they are excluded when performing the linear fit. No correlation is found between the $u - g$ color and the contamination in the *u*-band for VIPERS, as previously estimated with CIGALE.

This decontamination method associated with the calibration of Davies et al. (2016) leads to a significant underestimation of the SFR, especially for GSWLC, compared to CIGALE (Fig. 8 right). We also estimated the SFR based on the calibration of Davies et al. (2016) without performing any decontamination. As seen in Fig. C.1 (top right), it leads to a better agreement with CIGALE values.

Zhou et al. (2017) also found that a nonlinear calibration was in better agreement with the SFR derived from Hα and that the residuals were weakly correlated with the old stellar population. This SFR calibration is presented in Fig. C.1 (middle left) and is roughly equivalent to the calibration of Hopkins et al. (2003). At $z \sim 0.1$, Moustakas et al. (2006) showed that the scatter in the *u*-band luminosity to SFR calibration with respect to the D_{4000} break was mostly caused by the reddening effect. Therefore, a simple linear calibration based on the *u*-band should give a rather good estimation of the SFR. This calibration (see Fig. C.1, middle right) shows a high scatter and an underestimation of the SFR compared to CIGALE. However, the dust attenuation correction is already accounted for in their calibration, and such scatter and low SFR estimations may originate from the different treatement of dust reddening between the samples, rather than from a contamination from the old stellar population.

A proper calibration of the SFR based on the *u*-band should account for the old-stellar population contamination, assuming that the contribution to the luminosity of the old stars can be accurately removed. Because uncertainties due to dust attenuation dominate, a decontamination is not mandatory and the calibration of Hopkins et al. (2003), for instance, is able to give a reliable estimation of the SFR. This implies, however, that galaxies should not be significantly different from the sample from which the calibration is derived. Extrapolation of these calibrations to galaxies at higher redshifts is also subject to a larger scatter.

[7] The old stellar population contamination in the *u*-band and L_{TIR}, and the stellar contamination at 8 µm (in Sect. 4.1.3) were estimated from a Bayesian analysis, but were not implemented in CIGALE.

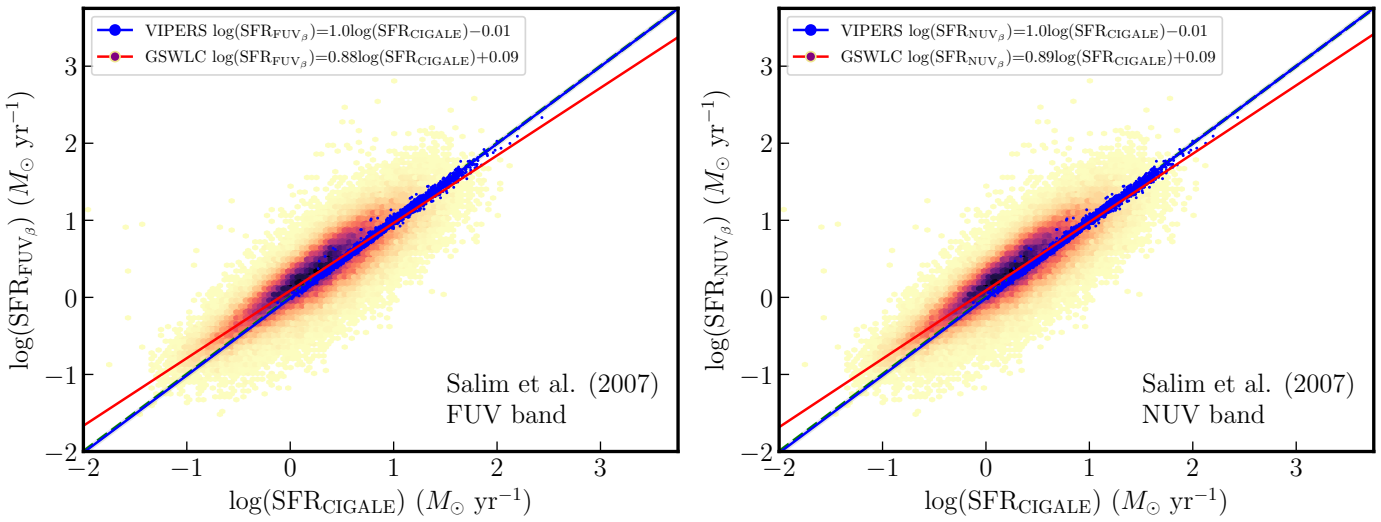


Fig. 7. SFR derived from the relations given in Salim et al. (2007) using GALEX FUV (*left*) and NUV (*right*), and the recalibrated attenuation law from β_{UV} (based on Eqs. (4) and (5) and VIPERS galaxies). There is a much better agreement with VIPERS (mean of 0.02 dex and a scatter of 0.03 dex for FUV and NUV, respectively) but also with GSWLC (−0.08 and 0.24 dex for FUV and NUV, respectively) considering that the attenuation prescription applied is based only on VIPERS galaxies.

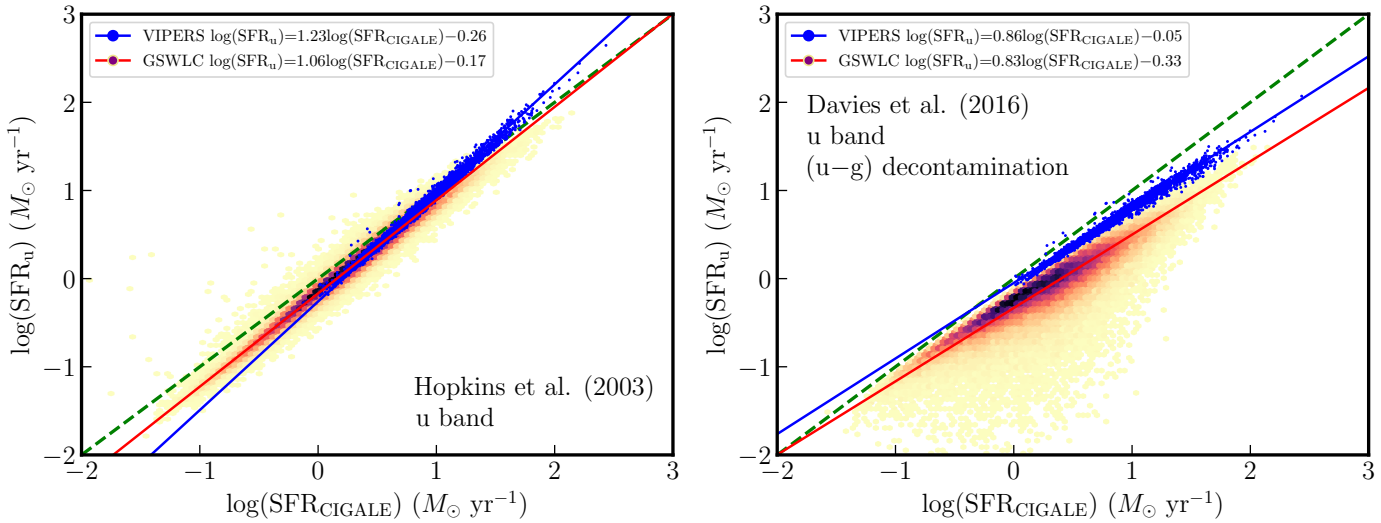


Fig. 8. Comparisons between the SFR from CIGALE and the literature using the *u*-band. *Left panel*: SFR derived from the relation given in Hopkins et al. (2003) using the *u*-band. *Right panel*: SFR derived from the calibrated relation given in Davies et al. (2016) using the *u*-band and the old population decontamination from the *u-g* color. While the calibration of Hopkins et al. (2003) is in good agreement with CIGALE (mean of 0.07 dex and scatter of 0.08 dex for VIPERS, 0.15 and 0.09 dex for GSWLC), the decontamination from the old stellar population luminosity proposed by Davies et al. (2016) leads to an underestimation of the SFR for VIPERS (0.18 and 0.06 dex) at high SFR, and to a strong underestimation for GSWLC (0.42 and 0.22 dex).

4.1.3. MIR and FIR indicators

The IR bands are often used as SFR tracers because their flux is related to high-mass stars through the emission of PAHs found around H II regions, and to the emission of dust. We used the calibrations of Kennicutt (1998), Wu et al. (2005), Pérez-González et al. (2006), Relaño et al. (2007), Zhu et al. (2008), Rieke et al. (2009), Gilbank et al. (2010), Young et al. (2014), Davies et al. (2016) and Brown et al. (2017), written in Appendix B.3.

At $z = 0$, the emission of PAHs excited by the UV radiation from OB stars is the main contributor to the luminosity at $\lambda = 8$ µm, followed by the emission from very small grains (VSGs) and stellar emission. Even if the PAH emission is correlated with metallicity (Schreiber et al. 2018), the luminosity at 8 µm remains roughly correlated with the SFR and useful due to its strength in star-forming galaxies. A better comprehension of PAH physics is crucial for future observations with JWST (Shipley et al. 2016), whose MIR bands from 5.6 to 25.5 µm were calibrated as SFR indicators (Battisti et al. 2015; Senarath et al. 2018).

Before calibrating the 8-µm emission as an SFR tracer, we removed the stellar component from $L_{8\,\mu m}$. Using CIGALE, we estimated this contamination as the ratio of the flux from the old and young stellar populations to the total luminosity in the *Spitzer* 8 µm filter. Galaxies with stellar contamination higher than 50% (72 galaxies) were found to have unreliable SED in the IR part of the spectrum and were not taken into account when dealing with SFR tracers at $\lambda \geq 8$ µm.

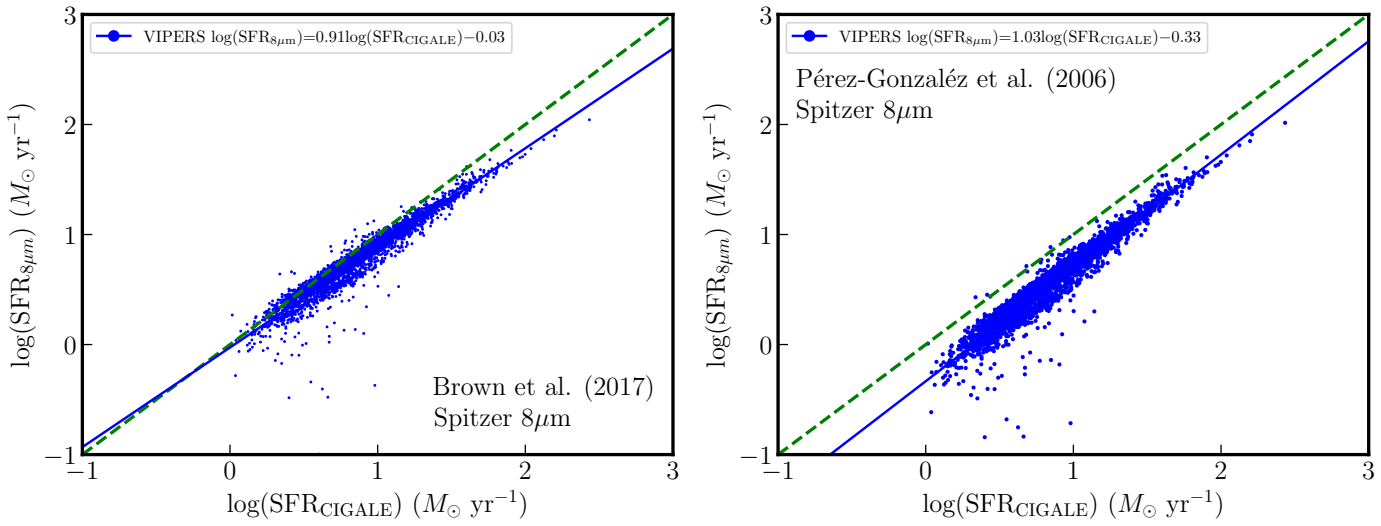


Fig. 9. Comparisons between the SFR from CIGALE and the literature at 8 μm. *Left panel*: SFR derived from the relations given in Brown et al. (2017) using *Spitzer* 8 μm from CIGALE (blue). *Right panel*: SFR derived from the relations given in Pérez-González et al. (2006) using *Spitzer* 8 μm from CIGALE. Both SFR calibrations show a disagreement with SFR from CIGALE (mean of 0.10 dex and scatter of 0.10 dex for Brown et al. 2017, 0.29 and 0.11 dex for Pérez-González et al. 2006), which could originate from the sample from which the calibration was established and from the different PAH properties of the galaxies.

The average stellar contamination in the 8 μm is 5%. This value is lower for the VIPERS sample than other samples such as Engelbracht et al. (2005) or Wu et al. (2005), which have a contamination of 10% for a sample of 34 nearby galaxies and a sample of 91 galaxies, respectively. In comparison, the estimated stellar contamination at 24 μm is, on average, equal to 0.2%.

Using different calibrations at 8 μm (Wu et al. 2005; Pérez-González et al. 2006; Young et al. 2014; Brown et al. 2017), we observed an underestimation of the SFR for each of them (Figs. 9, C.1 bottom). We note that Brown et al. (2017) did not remove the stellar component at 8 μm as it did not significantly change the fit parameters, contrary to the other calibrations. In addition to the stellar contamination, this discrepancy could also come from the sample of galaxies from which each SFR calibration was derived. For instance, the calibration of Brown et al. (2017) is based on 66 nearby star-forming galaxies for which the Hα flux ranges from $\sim10^{38}$ to $\sim10^{43}$ erg s^{-1}. Based on Hβ measurements for VIPERS galaxies, Hα could be as high as $\sim10^{44}$ erg s^{-1}, a luminosity at which the calibration of Brown et al. (2017) could be out of the range of applicability. The metallicity of galaxies could also impact the emission of PAHs, directly affecting the derived calibrations. An ideal SFR calibration at this wavelength requires a very good understanding of the PAHs' behavior with respect to the properties of the galaxy such as the metallicity, which is not yet achieved. This is underlined by the recent work of Gregg et al. (2022), who showed that the scatter of SFR-8 μm relation is related to the metallicity distribution.

In the mid-IR range, the 24-μm emission represents the dust heated by VSGs with a stable temperature. It is a reliable SFR tracer as this emission traces the interior of H II regions powered by high-mass stars. Two advantages of this band are: (1) it does not require any stellar subtraction, and (2) the attenuation is low enough to be omitted.

In GSWLC, the *Spitzer* data were not included, but the similarity between the 24-μm and WISE-4 filters makes it possible to find a relation between the luminosity in both bands (Jarrett et al. 2013). We compared the rest-frame luminosities and showed that $L_{24\,\mu m}$ is higher than L_{W4} by ∼8% for star-forming galaxies. We applied this 8% correction to L_{W4} when calibrations based on $L_{24\,\mu m}$ were used, bearing in mind that the impact on the SFR remains negligible.

Calzetti et al. (2010) listed several calibrations at 24 μm that have been proposed in the literature. Relations assuming a linear behavior work relatively well for VIPERS and GSWLC (Wu et al. 2005; Zhu et al. 2008; Rieke et al. 2009). The calibration giving the smallest scatter is given by Rieke et al. (2009), which, however, assumes a nonlinear behavior at $L_{24\,\mu m} > 5 \times 10^{43}$ erg s^{-1} (Fig. 10 left). The assumption of linearity induces an overestimation at high SFR and an underestimation at low SFR, for GSWLC.

Several works have shown that $L_{24\,\mu m}$ may not be directly proportional to the SFR. It could originate from different dust attenuation corrections at high SFR (Buat et al. 2007), a higher dust temperature inside H II regions leading to higher $L_{24\,\mu m}$, an underestimation of Paα from which $SFR_{24\,\mu m}$ may be calibrated, or self-absorption at 24 μm (Rieke et al. 2009). At low luminosity, galaxies become transparent and $L_{24\,\mu m}$ cannot reliably trace the SFR as a significant part comes from unabsorbed UV emission (Calzetti et al. 2010). Several authors calibrated their SFR in such a way (Wu et al. 2005; Pérez-González et al. 2006; Alonso-Herrero et al. 2006; Calzetti et al. 2007; Relaño et al. 2007; Zhu et al. 2008). For the VIPERS and GSWLC samples, a better agreement is indeed found when nonlinear relations are used; the best fit is given by the calibration of Zhu et al. (2008), which holds even outside the luminosity range for which their relation was calibrated (Fig. 10, right).

We also note that calibrations based on the observations of entire galaxies give better SFR estimations compared to those based on H II regions. This might be due to different dust temperatures between H II regions and galaxies, leading to a higher calibration constant in the case of entire galaxies (Calzetti et al. 2010). To test this, we used a subsample of 441 VIPERS galaxies having *Herschel* counterparts and we modeled the SED as a modified black-body (MBB, Casey 2012). Taking into account fits for which the uncertainty on T_{dust} is smaller than 50% (70 galaxies), T_{dust} ranges from 14.0 ± 1.4 to 46.5 ± 16.2 K, with an average equal to 27.7 ± 1.4 K. In comparison, the dust

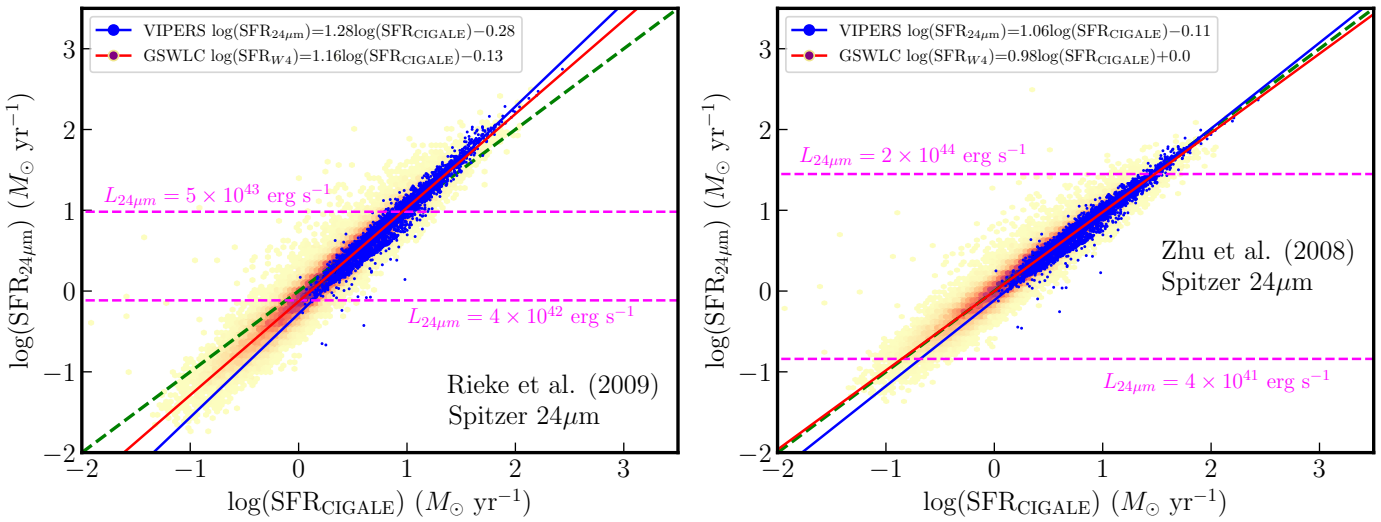


Fig. 10. Comparisons between the SFR from CIGALE and the literature at 24 μm. *Left panel*: SFR derived from the relations given in Rieke et al. (2009) using *Spitzer* 24 μm from CIGALE (blue). The continuous magenta line represents the limit above which a nonlinear correction is used. *Right panel*: SFR derived from the relations given in Zhu et al. (2008) using *Spitzer* 24 μm. The dashed magenta lines represent the domain of applicability, as defined by Calzetti et al. (2010). The small discrepancy observed using Rieke et al. (2009) (mean of 0.004 dex and scatter of 0.13 dex for VIPERS, 0.07 and 0.16 dex for GSWLC) may originate from the hypothesis of linearity (the nonlinearity correction for Rieke et al. (2009) is small), while a nonlinear calibration such as Zhu et al. (2008) gives a better agreement (mean of 0.04 dex and scatter of 0.08 dex for VIPERS, 0.01 and 0.12 dex for GSWLC).

temperature of H II regions in the Milky Way is similar (Anderson et al. 2014; Figueira et al. 2017). Therefore, the difference between entire-galaxy- and H II-region-based calibrations may not come entirely from a difference in temperature. An example is shown in Fig. C.2 (top left) where the Relaño et al. (2007) calibration based on H II regions shows an underestimation of the SFR for VIPERS galaxies. The calibration of Brown et al. (2017) shown in Fig. C.2 (right) also underestimates the SFR of VIPERS galaxies at high luminosity, despite being calibrated on entire galaxies.

We estimated the SFR from $L_{\rm TIR}$ (measured with CIGALE for VIPERS and using the WISE-4 band for GSWLC, with the BOSA templates, Boquien & Salim 2021) following the calibration of Kennicutt (1998), and Fig. 11 shows that there is a rather good agreement with the SFR from CIGALE. At this redshift, this correlation is expected since our samples, both at low and intermediate z, are composed of star-forming galaxies and should not contain outliers. In Sect. 5.1, we show that the scatter in $L_{\rm TIR}$ for VIPERS should be around ~0.2 dex, and a similar scatter be added to the SFR derived from $L_{\rm TIR}$. For GSWLC, the scatter in $L_{\rm TIR}$ and SFR from BOSA templates is around 0.15 and 0.17 dex (Boquien & Salim 2021). In the next section, we show that part of the dust emission is due to the old stellar population but, as for the *u*-band, calibrations usually do not take this into account. This could explain why the SFR is slightly overestimated using the calibration of Kennicutt (1998), which assumes a population of young stars.

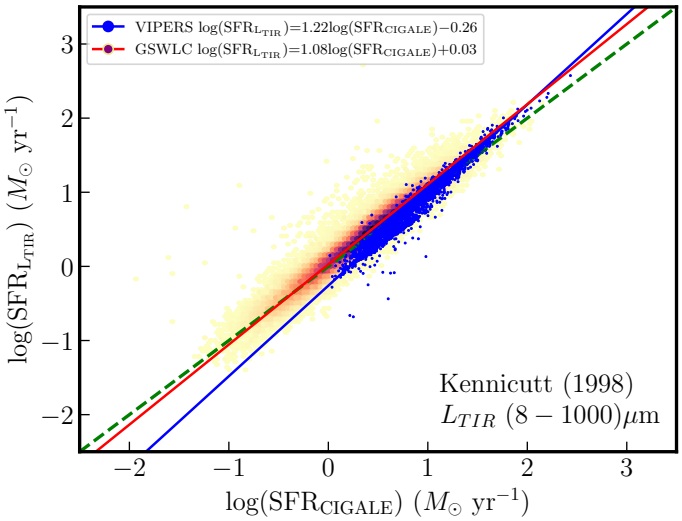


Fig. 11. SFR derived from the relations given in Kennicutt (1998) using CIGALE for VIPERS (blue) and WISE-4 for GSWLC (density plot). Blue lines and red lines are the fits for VIPERS and GSWLC, respectively. The agreement between the calibration and CIGALE SFRs is good (mean of 0.04 dex and scatter of 0.11 dex for VIPERS, 0.04 and 0.13 dex for GSWLC).

4.1.4. Composite SFR indicators

Previously, we used SFR calibrations based on a single band only (two close bands in the case of attenuation correction in the UV). While this method is practical, since just one band is needed, it requires correction for dust attenuation in the UV part of the spectrum. Such corrections depend on the dust attenuation recipe used, which also depends on galaxies' properties, such as inclination (Battisti et al. 2017), axis ratio (Wild et al. 2011), optical opacity (Salim et al. 2018), dust luminosity (De Barros et al. 2016), or redshift (Bogdanoska & Burgarella 2020). In addition, these laws are averaged over samples of galaxies that might be different from the studied sample.

A popular method to correct for dust attenuation without relying on attenuation laws is to use a direct tracer of young high-mass stars (UV, Hα, [O II]) and an indirect tracer that takes into account the flux absorbed and re-emitted in the infrared ($L_{\rm TIR}$, 8 μm, 24 μm). Appendix B.5 includes the laws used in this subsection: Bell et al. (2005), Kennicutt et al. (2009), Arnouts et al. (2013), Boquien et al. (2014), and Clark et al. (2015).

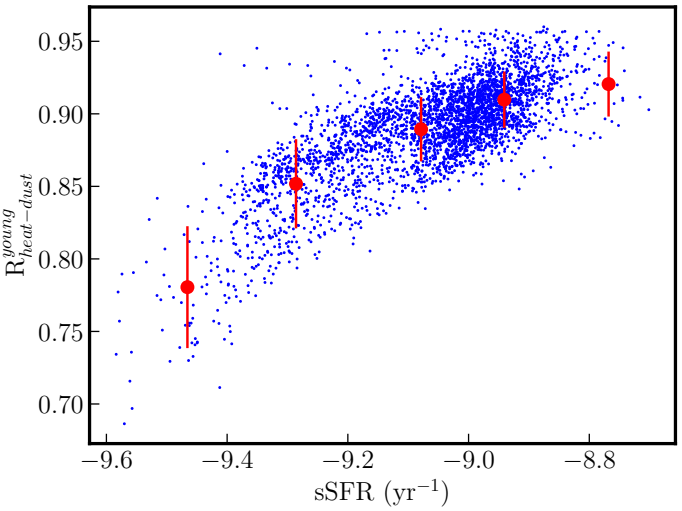


Fig. 12. Fraction of dust heated by the young stellar population with respect to the sSFR for VIPERS, where each bin (red points) represents the median for ∼420 galaxies and uncertainties are estimated as the standard deviation. The fraction of dust heated by the young stellar population increases as the stellar activity of the galaxy increases.

In Bell et al. (2005), the SFR was calibrated with the PEGASE population synthesis model (Fioc & Rocca-Volmerange 1997) using the FUV band and $L_{\rm TIR}$. While slightly overestimated, the SFRs show a very good agreement with CIGALE values (Fig. C.2 middle-left). Clark et al. (2015) calibrated the SFR using the FUV and 24-µm bands from Hirashita et al. (2003), Buat et al. (2008), and Jarrett et al. (2013), but took into account that, in addition to OB stars, the old stellar population can also heat the dust, overestimating the SFR estimation.

To estimate this quantity for VIPERS galaxies, we computed the absorbed luminosity of the young and old stellar population relatively to $L_{\rm dust}$. The fraction of dust emission due to the young or old stellar population, depending on the component that is considered, is estimated following

$$R_{\rm heat\text{-}dust} = \frac{\int_{91.2\ \rm nm}^{+\infty} L^{\rm non\text{-}att}_{\rm stellar} {\rm d}\lambda}{\int_{91.2\ \rm nm}^{+\infty} L_{\rm dust} {\rm d}\lambda}. \quad (6)$$

The integration is done from 91.2 nm onward, corresponding to the range in which the absorption is due to dust.

For GSWLC galaxies, we estimated $R^{\rm old}_{\rm heat\text{-}dust}$ using the relation between *s*SFR and the $R^{\rm young}_{\rm heat\text{-}dust}$ parameter established by Nersesian et al. (2019) for 814 nearby galaxies. The fraction of dust emission due to the old stellar population is

$$R^{\rm old}_{\rm heat\text{-}dust} = \begin{cases} 11\% & \text{(VIPERS)} \\ 45\% & \text{(GSWLC)} \end{cases}. \quad (7)$$

As expected, the fraction of dust heated by the old stellar population is lower for intermediate redshift galaxies due to the higher number of young stars compared to local galaxies. This is also what is observed in Nersesian et al. (2019), where more than 80% of dust emission in early-type galaxies (E to S0) is due to old stellar population and decreases to ∼40% for late-type and irregular galaxies. In Fig. 12 we show how the fraction of dust emission due to the young stellar population increases with the specific star formation rate (sSFR) for the VIPERS sample.

Other studies such as De Looze et al. (2014) and Viaene et al. (2016) derived such a relation between $R^{\rm young}_{\rm heat\text{-}dust}$ and sSFR, whose shape resembles the relation of Nersesian et al. (2019) but gives a higher $R^{\rm young}_{\rm heat\text{-}dust}$ at a lower sSFR. Applied to GSWLC, these relations would cause the fraction of dust heated by young stars to increase by ∼20%, giving a contamination on the order of 25%. Nersesian et al. (2019) attributes this offset to the different methods used to retrieve this fraction. Such low contamination was observed by Buat et al. (2011b) for a sample of local galaxies from AKARI with $R^{\rm old}_{\rm heat\text{-}dust} = 17\%$, but the contamination reaches ∼10% for sSFR similar to VIPERS.

Other works (e.g., Hirashita et al. 2003; Bell 2003; Hao et al. 2011) found values on the order of 30% to 50%. This underlines the fact that an accurate derivation is not trivial and depends on the method and stellar population templates used to derive this fraction. The main conclusion, in agreement with most of the studies, is that the contamination of dust emission by the old stellar population can be significant, even for blue star-forming galaxies. Using the values of contamination that we found (Eq. (6)) in the calibration proposed by Clark et al. (2015), we obtain a good agreement with CIGALE (Fig. 13 top left).

Instead of UV, Kennicutt et al. (2009) used the [O II] spectral line as a direct tracer of young high-mass stars and different bands to represent the PAH or dust emission (8, 24 µm and $L_{\rm TIR}$, see Fig. 13). Using the 8-µm band as a complement of the blue band leads to a similar underestimation of the SFR as in Brown et al. (2017), which may originate from the inadequacy of the 8-µm emission as a reliable tracer of SFR due to its dependence on metallicity. There is a good agreement when using $L_{\rm TIR}$ as a tracer of obscured SFR for the VIPERS galaxies but the best agreement, both for VIPERS and GSWLC, is reached when using 24 µm as a tracer of dust emission.

Similarly to Bell et al. (2005), Arnouts et al. (2013) used a relation between $L_{\rm NUV}$ and $L_{\rm TIR}$ to compute the SFR where $L_{\rm TIR}$ is estimated from the NUVrK$_{\rm s}$ diagram. Briefly, the infrared excess, defined as IRX = $L_{\rm TIR}/L_{\rm NUV}$, is found to be constant along with stripes in the NUVrK diagram, and can be parametrized using the vector perpendicular to those stripes (the NRK vector) and z. Prior to estimating the SFR, we only kept galaxies at $z > 0.1$ (19 441 galaxies, 21% of the GSWLC sample) because the evolution of IRX with respect to z is not constrained around $z \sim 0$. We also removed the passive galaxies from this GSWLC subsample (NRK$_{\rm sSFR} > 1.9$, 3 galaxies).

The SFR given by the NRK method for VIPERS galaxies has a scatter of 0.14 dex and is slightly overestimated at low SFR by around 0.1 dex (Fig. C.2 middle right). In addition, 265 VIPERS galaxies (8% of the sample) are found to have catastrophic SFR estimations ($|{\rm SFR_{CIGALE}} - {\rm SFR_{NrK}}| > 3\sigma$, Arnouts et al. 2013). For GSWLC, the SFR estimation based on the NUVrK diagram underestimates the SFR by ∼0.21 dex, with catastrophic estimations for 1558 GSWLC galaxies (8% of the sample). For both samples, the offsets are less than the accuracy of the method derived by Arnouts et al. (2013) to recover $L_{\rm TIR}$, which is close to 0.3 dex for the low-z sample and 0.21 dex for $0.2 < z < 1.3$. Additionally, Arnouts et al. (2013) showed that the observed stripes (with constant IRX) can be only reproduced using a two-component dust attenuation law (birth clouds + ISM), whereas the dust attenuation correction for GSWLC is based on a modified Calzetti attenuation law.

Using eight nearby galaxies from the KINGFISH sample, Boquien et al. (2016) derived the fraction of IR luminosity that has to be added to the attenuated $L_{\rm FUV}$ to obtain a reliable estimation of the SFR. Based on CIGALE estimations, they found that the coefficient that should be applied to $L_{24\,\mu\rm m}$ depends on the sSFR and can vary by an order of magnitude. This shows that it is generally not correct to use the same single value for

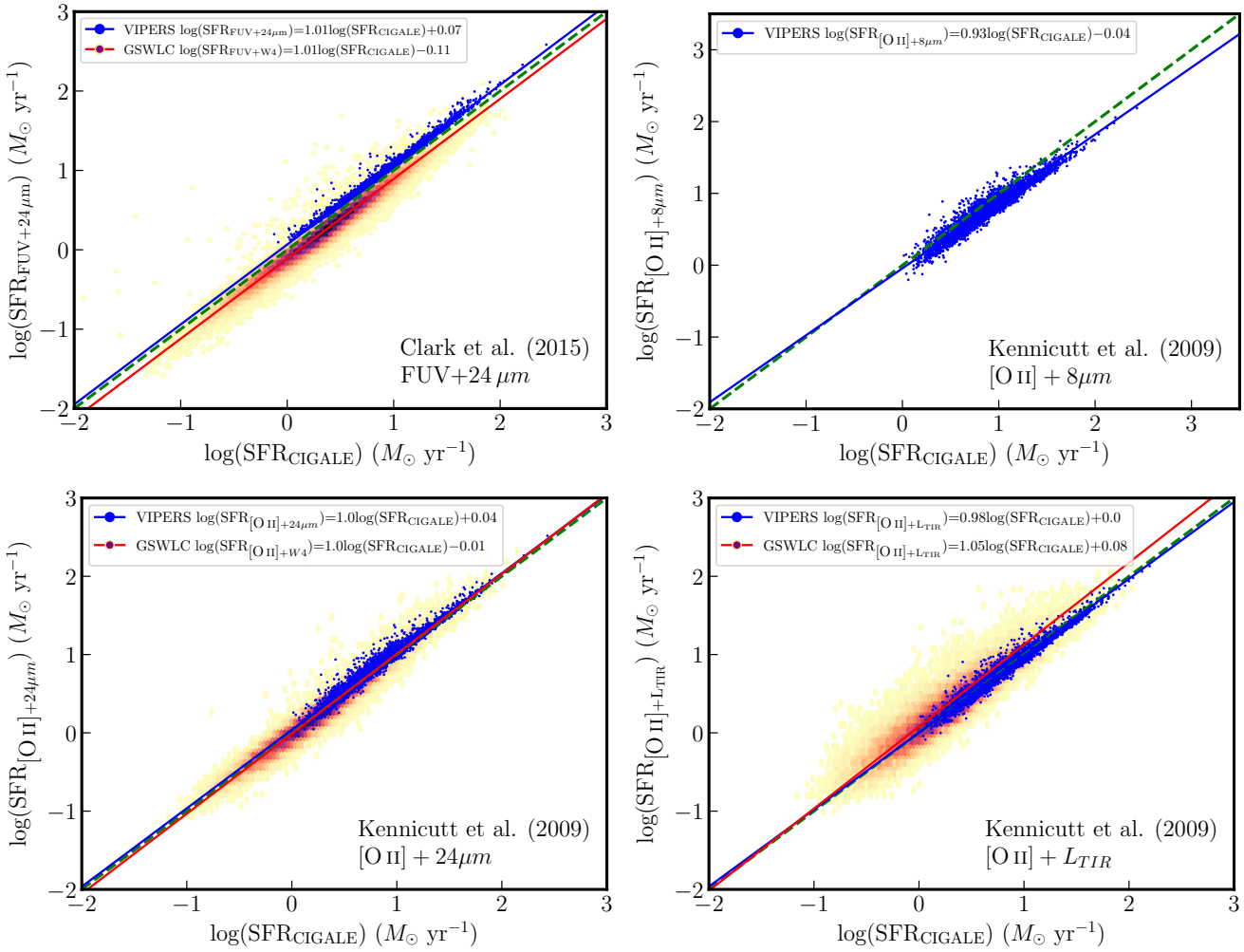


Fig. 13. SFR derived from the relations given in Clark et al. (2015) using GALEX FUV and $L_{24\,\mu m}$ or L_{W4} using the old stellar population contamination (Eq. (7)) (*top left*, mean of −0.08 dex and scatter of 0.03 dex for VIPERS, 0.12 and 0.10 dex for GSWLC). SFR derived from the relations given in Kennicutt et al. (2009) using [O II] associated with 8 µm (*top right*, mean of 0.12 dex and scatter of 0.09 dex for VIPERS), 24 µm (*bottom left*, mean of −0.04 dex and scatter of 0.06 dex for VIPERS, 0.02 and 0.10 dex for GSWLC), and L_{TIR} (bottom right, mean of 0.01 dex and scatter of 0.07 dex for VIPERS, −0.06 and 0.18 dex for GSWLC).

all the galaxies in a sample. However, without resolved observations at NIR wavelength, we are forced to use a simple value representing the whole sample. Using the relation of Hao et al. (2011) to scale $L_{24\,\mu m}$ and the conversion factor from FUV to SFR from Boquien et al. (2014), we found a good agreement with the CIGALE SFR (see Fig. 14 middle).

Composite calibrations offer a way to estimate the total SFR (obscured + unobscured), which is very a convenient method as dust attenuation in the blue part of the spectrum can carry significant uncertainties. Nonetheless, two bands or more are required to estimate the SFR, which are not necessarily obtainable for every galaxy. In addition, the monochromatic data must be k-corrected when $z > 0$, which involves SED fitting from which we can directly obtain an estimation of the SFR. As a consequence, the usefulness of this method really depends on the availability of multiwavelength data for the galaxies considered.

4.2. SFR from spectral lines

4.2.1. Hβ line

Toward local galaxies, the Hβ line is mostly used to correct for dust attenuation through the Balmer decrement but generally not as an SFR indicator, as Hα is available. When the redshift increases, Hα is shifted out the optical window and is more difficult to observe. Making use of Hβ as an SFR tracer relies on the assumption that it can be related to Hα through the intrinsic Balmer decrement. While this value can be different based on the temperature and electronic density of the H II region, it is generally assumed to be equal to 2.86.

For VIPERS, the SFR obtained from Hβ and the Hα calibration from Kennicutt (1998), assuming a Balmer decrement, reproduces the SFR given by CIGALE with a scatter of 0.19 dex, but an overestimation of the SFR can be observed around ∼100 $M_\odot$ yr^{-1} (Fig. 15). Different electron density (n_e) and electron temperature (T_e) values for H II regions translates into different values of the Balmer decrement. For $n_e = 10^2$ cm^{-3} and $T_e = 5000, 10\,000, 20\,000$ K, the Balmer decrement ranges from 3.03 to 2.74 (Hummer & Storey 1987) but cannot explain the deviation observed. We checked if these highly active galaxies could be Seyfert 2 but most of them are located in the star-forming part of the BPT diagram (Fig. 2). We checked the evolution of the S/N ratio of fluxes and EWs of the VIPERS star-forming galaxies with respect to the redshift but no change is observed, indicating that a selection bias at high luminosity cannot explain the observed overestimation. Such an overestimation

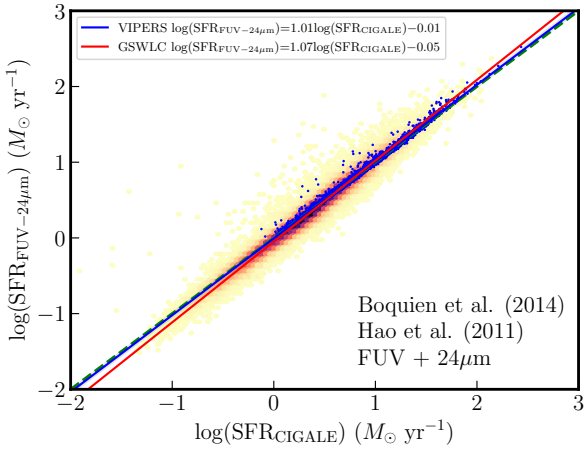


Fig. 14. SFR derived from the relation given in Boquien et al. (2014) using the coefficient of Hao et al. (2011). There is an excellent agreement with SFR from CIGALE for VIPERS (mean of −0.01 dex and scatter of 0.03 dex) and GSWLC (0.02 and 0.10 dex).

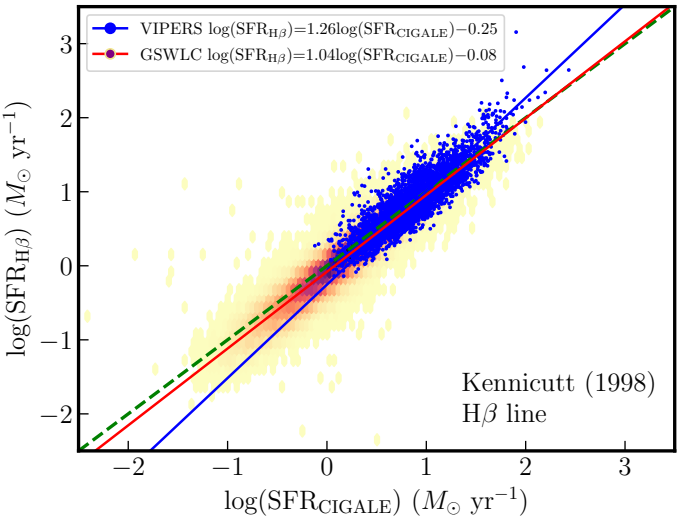


Fig. 15. SFR derived from Hβ (Kennicutt 1998) assuming (Hα/Hβ)$_{int}$ = 2.86 vs. SFR derived from CIGALE. A good agreement is observed for GSWLC (mean of 0.07 dex and scatter of 0.19 dex), while there is an overestimation at high SFR for VIPERS (−0.01 and 0.19 dex).

is also seen when using a stellar absorption correction of 3 and 4 Å. A more detailed study would require Hα measurements in order to see if this overestimation is also observed. For GSWLC, the agreement with CIGALE SFR is excellent (scatter of 0.19 dex).

4.2.2. [O II]λ 3727 line

The [O II] line is often used as an SFR tracer as it originates from the same location as Hα, with a similar timescale. At $z \sim 0.7$, Maier et al. (2015) consider the SFR calibration based on [O II] to be the second best one after Hα using the calibration of Gilbank et al. (2010). However, [O II] suffers from two main disadvantages: high dust attenuation and a dependence on metallicity. While dust attenuation can be corrected easily in this work as CIGALE estimates the attenuation in specific bands, the metallicity is more difficult to constrain. Several studies have been performed at low redshifts to estimate the metallicity using the Hα, Hβ, [N II], [S II], [O II], and [O III] lines (e.g., Kewley & Dopita 2002; Zhuang & Ho 2019). Since only the three bluest lines (Hβ, [O II] and [O III]) are available in VIPERS, we based our metallicity estimation on R_{23} (Pagel et al. 1979), defined as:

$$R_{23} = \frac{[\mathrm{OII}]\lambda3727 + [\mathrm{OIII}]\lambda\lambda4959,5007}{\mathrm{H}\beta}, \quad (8)$$

and the calibration of Zaritsky et al. (1994, hereafter Z94):

$$\log(\mathrm{O/H}) + 12 = \begin{cases} 9.265 - 0.33x - 0.202x^2 \\ \qquad - 0.207x^3 - 0.333x^4, \\ x = \log(R_{23}), \\ \\ \text{Valid for } \log(\mathrm{O/H}) + 12 > 8.4. \end{cases} \quad (9)$$

Diagnostics based on R_{23} are problematic because this parameter is double-valued. Therefore, this method is often used in combination with a first estimation of the metallicity to break the degeneracy (Kewley & Dopita 2002). Since we did not have another reliable method to make the first estimation, we based our choice of the R_{23} branch on the [O III]λ5007/[O II]λ3727 ratio. In Nagao et al. (2006), this ratio was proposed to distinguish between the two branches, where the high-metallicity branch is associated with [O III]λ5007/[O II]λ3727 < 2 (Fig. 16). We remind the reader that the estimation of metallicity for GSWLC is based on the [O II]+[O III] sample (see Table 3). Based on this criterion, we found that five GSWLC (0.02%) and 76 VIPERS (2%) galaxies are part of the lower metallicity branch. These galaxies were excluded from SFR comparisons and we focused on high-metallicity galaxies, which are predominant in our sample.

In addition, the R_{23} parameter depends on the [OIII]λ5007/Hβ ratio, which increase with redshift (Sect. 3.1.1). For increasing ionization parameters ranging from −3.2 (typical value for SDSS galaxies, Liang et al. 2006) to −2.3, the metallicity is overestimated by 0.1 dex at most (Cullen et al. 2016), which corresponds to the uncertainty of the R_{23} method. This dependence is, therefore, not problematic at $z < 1$, but should be considered when estimating and comparing the metallicity over a higher and wider range of redshift.

To estimate the SFR from the [O II] line, we first used the initial calibration of Kennicutt (1998). Despite assuming an average reddening based on the sample used by Kennicutt (1998), the agreement is good with a scatter of 0.19 dex for VIPERS and a mean difference of 0.11 dex (Fig. 17), while the SFR is slightly underestimated at high SFR for GSWLC.

To improve this relation, we used the Hα calibration of Kennicutt (1998) and converted it to a [O II] SFR calibration,taking the correction-attenuated [O II]/Hα ratio as a conversion factor between the Hα-SFR and [O II]-SFR relations. Here, the Hα flux comes from the Hβ flux, scaled by the Balmer decrement for both samples for consistency, even if Hα is available for GSWLC. The dependence of the attenuated [O II]/Hα with the color excess $E(B-V)$, estimated with CIGALE, is shown in Fig. 18 and disappears when the dust attenuation is correctly taken into account, with an average [O II]/Hα equal to 1.16. Using this new calibration, the scatter is reduced from 0.19 to 0.17 dex at the cost of an increase in the slope (Fig. 18 right). We note that Hα for VIPERS is derived from Hβ, and so any deviation, as observed in Fig. 15, would increase the uncertainty of this new [O II] SFR calibration. For GSWLC, the scatter slightly increases but the slope gets closer to one when the proper attenuation is taken into account.

Based on the Z94 calibration, we estimated the metallicity dependence on the [O II]/Hα ratio. Figure 19 (left) shows

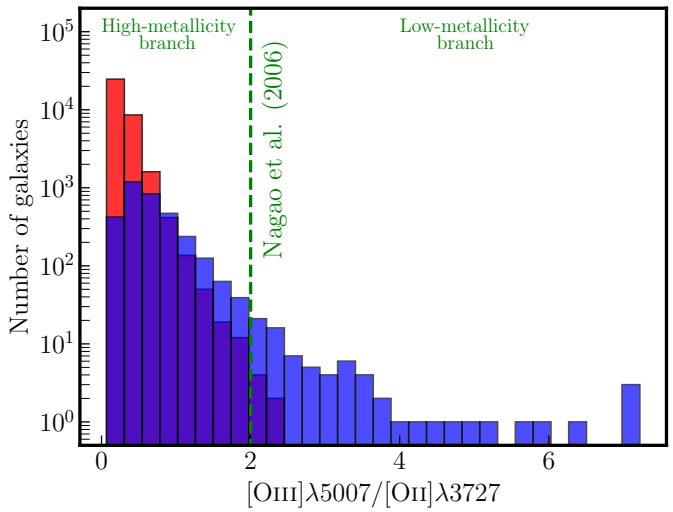


Fig. 16. Histogram of [O III]λ5007/[O II]λ3727 for the GSWLC (red) and the VIPERS star-forming (blue) samples. The boundary between the lower and upper branch in the R_{23} diagnostic from Nagao et al. (2006) is shown as a dashed green line. Most of the galaxies are found on the high-metallicity branch (99.98% for GSWLC and 98% for VIPERS).

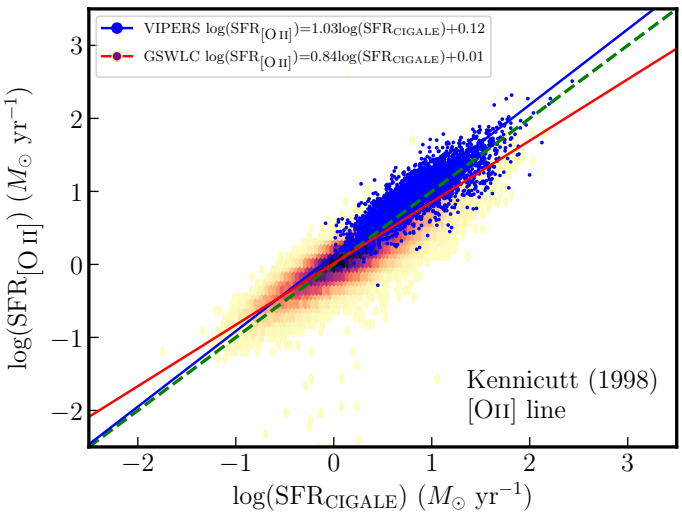


Fig. 17. SFR derived from [O II] using the direct calibration from Kennicutt (1998). A good agreement is observed for VIPERS (mean of −0.11 dex and scatter of 0.19 dex), whereas the SFR for GSWLC is underestimated at high SFR (0.08 and 0.23 dex).

this dependence for VIPERS and GSWLC. For GSWLC, the observed distribution is similar to the one found by Zhuang & Ho (2019) using the Z94 and Kewley & Dopita (2002) methods. The higher dispersion observed for VIPERS galaxies could originate from a higher dispersion of ionization parameters, modifying the shape of the [O II]/Hα ratio versus log(O/H)+12 established from theoretical models (Kewley et al. 2004). The fit of [O II]/Hα versus 12+log(O/H) is given by:

$$[\mathrm{O\,II}]/\mathrm{H}\alpha = \begin{cases} (-1.82 \pm 0.08)x + (17.07 \pm 0.70)\ \text{(VIPERS)}, \\ (-1.79 \pm 0.07)x + (16.99 \pm 0.65)\ \text{(GSWLC)}, \\ (-1.75 \pm 0.25)x + (16.73 \pm 2.23), \\ \text{(Kewley et al. 2004)}. \\ \\ x = 12 + \log(\mathrm{O/H}). \end{cases} \tag{10}$$

The fit for GSWLC and the relation for VIPERS are found to be in agreement within the uncertainties when compared with Kewley et al. (2004). We applied this metallicity calibration for galaxies that are part of the upper R_{23} branch. Compared to the original law of Kennicutt (1998), we observe a slight decrease in the scatter, as well as an increase in the slope, when a metallicity correction is applied (Fig. 19 right). We observed an improvement of the SFR estimation for GSWLC when the metallicity correction is taken into account.

Known methods to estimate the metallicity are mainly based on studies performed in local galaxies due to the availability of good estimators such as Hα and [N II]. Following Kewley et al. (2004), we estimated the metallicity using other calibrations: McGaugh (1991), Kobulnicky et al. (1999), Pilyugin (2001), and Tremonti et al. (2004), all based on R_{23}.

We did not use the calibration of Charlot & Longhetti (2001) because more than 92% of the galaxies in our sample are characterized by [O II]/[O III]λ5007 $>$ 0.8. This means that the metallicity will be estimated through the [O III]/Hβ ratio, which is more sensitive to the ionization parameter rather than the metallicity. The resulting metallicity shows a very high dispersion, in addition to being uncorrelated with the abundance, contrary to the previous calibrations of Kewley et al. (2004) and Zhuang & Ho (2019).

Figure 20 shows the relation between [O II]/Hα and metallicity from McGaugh (1991), Kobulnicky et al. (1999), Pilyugin (2001), and Tremonti et al. (2004). The shape of the distribution of galaxies is in agreement with the one based on the [N II]/[O II] from Kewley & Dopita (2002), and the one from Z94 (Fig. 19). The lower slope with McGaugh (1991) is attributed to the different stellar atmosphere and models used for the calibration (Kewley & Dopita 2002). We applied these different metallicity corrections but none of them were found to significantly improve the estimation of the SFR compared to Z94.

Similarly, as for the NUV band, Rosa-González et al. (2002) proposed a calibration based on the [O II] luminosity, where the attenuation and metallicity are directly taken into account. This calibration overestimates the SFR by an offset of ∼0.45 dex for both samples (Fig. C.2 bottom left). It is not surprising to observe a large discrepancy as the dust and metallicity corrections might be significantly different between VIPERS and the sample used in Rosa-González et al. (2002).

Gilbank et al. (2010) estimates the SFR from [O II], assuming a constant attenuation of 1 mag at Hα and a general correction that takes into account the metallicity from the mass metallicity relation. Despite these strong assumptions, we found a surprisingly good agreement (Fig. C.2 bottom right) and note that this relation gives a better agreement with CIGALE SFR for GSWLC than the metallicity-corrected [O II] calibration. The attenuation correction is an average value that is often used in the local Universe and we note that the metallicity correction for the calibration of Gilbank et al. (2010) is based on the SDSS DR4. This could explain why the agreement does not strongly deviate from CIGALE SFR for GSWLC, as for the calibration of Rosa-González et al. (2002), but gives a worse agreement for VIPERS.

4.2.3. [O III]λ5007 line

The [O III]λ5007 line is not widely used as an SFR indicator, as only a rough estimation of the SFR can be obtained (Teplitz et al. 2000; Kennicutt et al. 2009). Similarly as for [O II], we used the

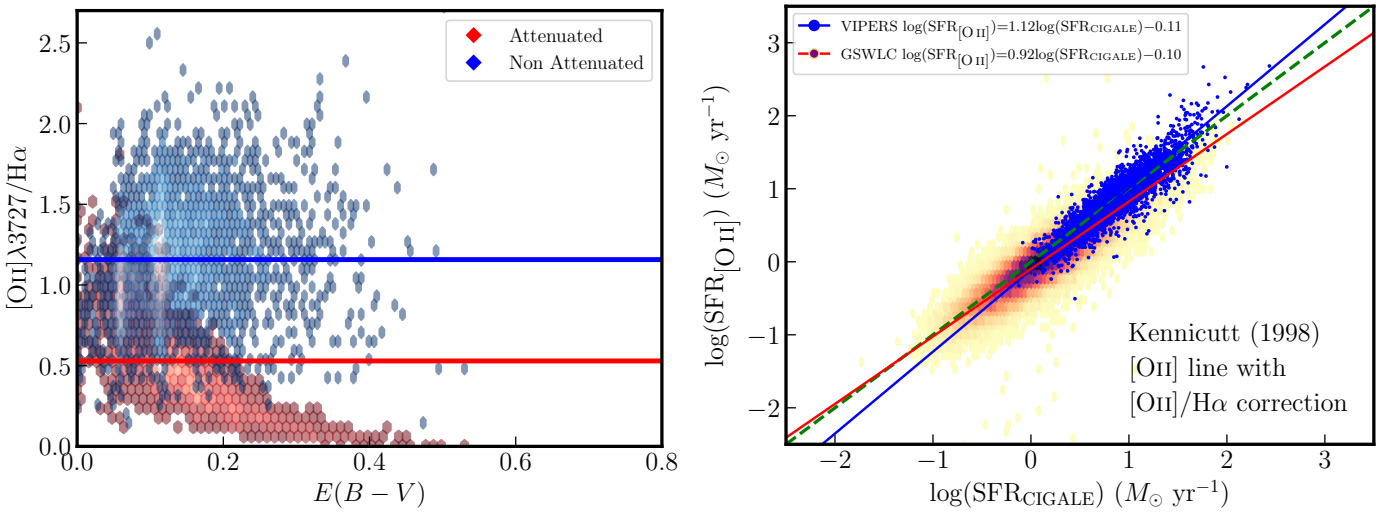


Fig. 18. SFR derivation from [O II] using Kennicutt (1998) and a reddening correction. *Left panel*: [O II]/Hα ratio (assuming Hα = 2.86Hβ) as a function of the color excess, without (red) and with (blue) dust attenuation correction; the continuous lines represent the average ratio. *Right panel*: SFR derived from [O II] using the Hα calibration of Kennicutt (1998) and the attenuation-corrected [O II]/Hα ratio. For VIPERS and GSWLC, the slope increases in comparison with the direct [O II] calibration, but the scatter decreases (mean of 0.01 dex and scatter of 0.17 dex for VIPERS, 0.12 and 0.22 dex for GSWLC).

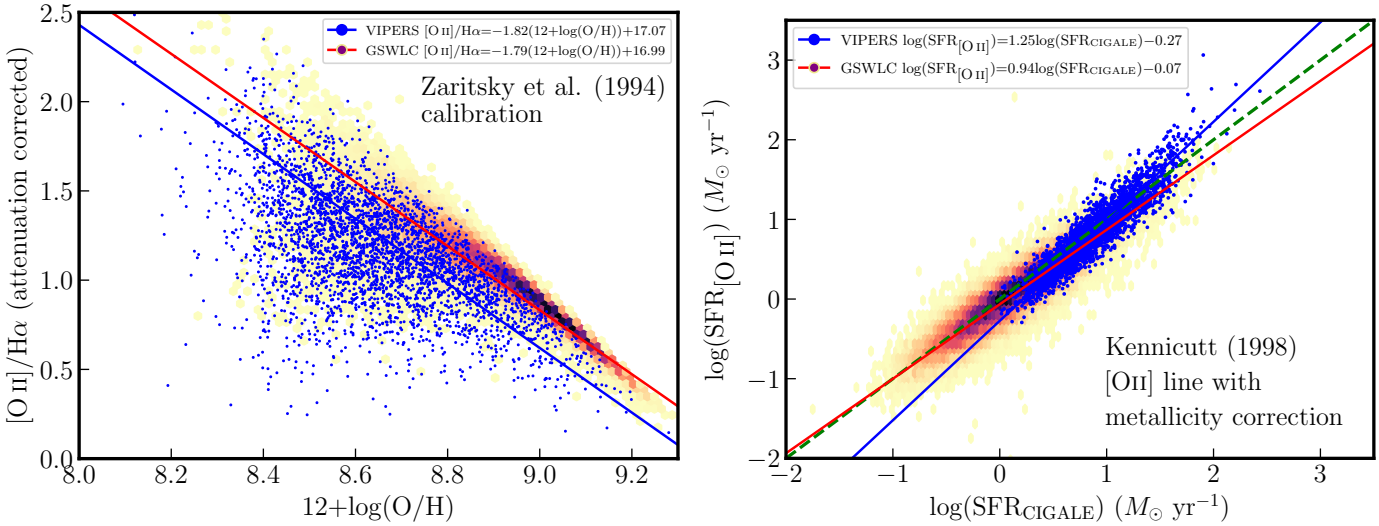


Fig. 19. SFR derivation from [O II] using Kennicutt (1998) and a metallicity correction. *Left panel*: [O II]/Hα ratio (assuming Hα = 2.86Hβ) corrected for dust attenuation versus metallicity estimated using the Zaritsky et al. (1994) calibration for the VIPERS (blue) and GSWLC (density) samples, with their associated linear fit. *Right panel*: SFR derived from [O II] using the Hα calibration of Kennicutt (1998) and the attenuation-corrected [O II]/Hα expressed as a function of metallicity. The slope increases for both samples and the scatter decreases compared to the direct [O II] calibration (mean of 0.05 dex and scatter of 0.17 dex for VIPERS, 0.06 and 0.20 dex for GSWLC).

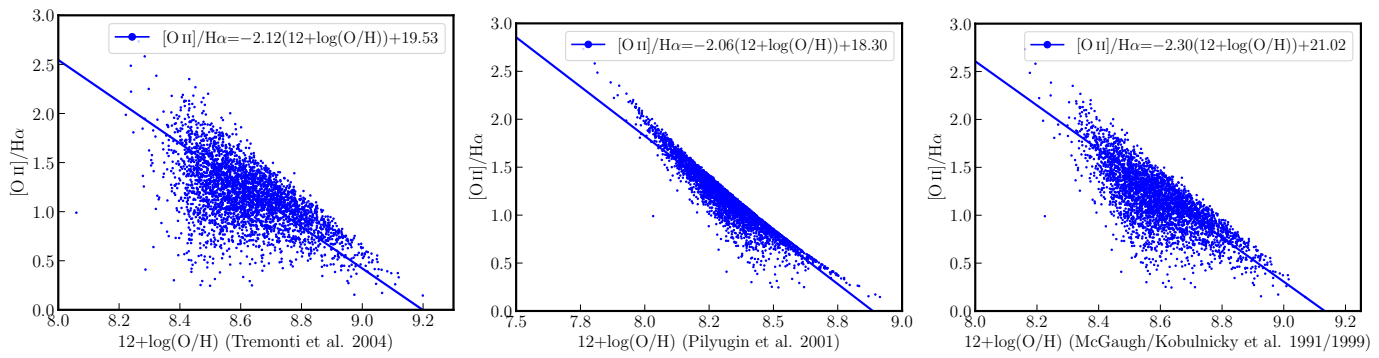


Fig. 20. [O II]/Hα versus metallicity for VIPERS, estimated with the R_{23} calibrations of Tremonti et al. (2004; *left*), Pilyugin (2001; *middle*), and McGaugh (1991; *right*). Compared to Z94, there is a good agreement with Tremonti et al. (2004) and McGaugh (1991; mean difference of 0.03 and 0.06 dex) but above the typical uncertainty for metallicity based on R_{23} (0.1 dex) for McGaugh (1991; mean difference of 0.3 dex).

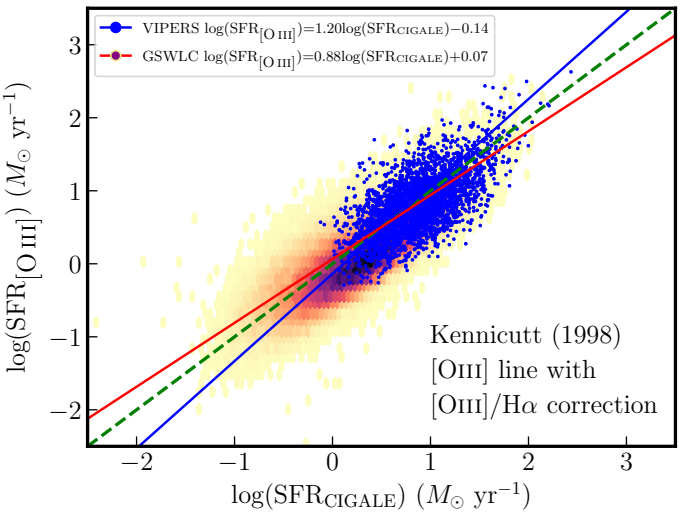


Fig. 21. SFR derived from Hα SFR calibration of Kennicutt (1998) and the attenuation-corrected [O III]/Hα ratio. Estimation of SFR with [O III] leads to a significant scatter for VIPERS (mean of −0.04 dex and scatter of 0.31 dex) and GSWLC (−0.17 and 0.32 dex).

Kennicutt (1998) calibration and converted it into a [O III]-SFR calibration using the average value [O III]/Hα corrected for attenuation. Compared to other line calibrators, the SFR estimation using [O III] shows a large scatter of 0.3 dex for VIPERS and GSWLC (Fig. 21). We also estimated the SFR using the general calibration from Villa-Vélez et al. (2021) but we found a similar scatter for VIPERS and a mean difference of 0.5 dex for GSWLC.

The [O III]/Hα ratio is equal to 0.72 and 0.21 for VIPERS and GSWLC, respectively, but others works found different ratios at different redshifts: 1 (Teplitz et al. 2000, $3.3 < z < 3.4$), 0.79 (Hippelein et al. 2003, $0.4 < z < 0.64$), 1.05 (Ly et al. 2007, $0.07 < z < 1.47$), 1.23 (Straughn et al. 2009, $0.1 < z < 1.1$), and 0.86 (Villa-Vélez et al. 2021, $1.4 < z < 1.68$). Due to this wide range of values, a direct calibration (i.e., an SFR only proportional to the luminosity) of the SFR encompassing a large range of redshift, such as for [O II], cannot be obtained.

To derive a calibration over a wide range of redshift, a metallicity correction should be included. Figure 22 (left) shows the dependence of [O III]/Hα with respect to the metallicity, using the calibration of Z94. The results of the fit are

$$\text{[O III]/H}\alpha = \begin{cases} -140.6304 + 57.9913x - 7.5446x^2 \\ \qquad + 0.3157x^3 \text{ (VIPERS)}, \\ 2281.0376 - 750.5980x + 82.3943x^2 \\ \qquad - 3.0170x^3 \text{ (GSWLC)} \\ \\ \qquad x = 12 + \log(\text{O/H}). \end{cases} \tag{11}$$

We applied this metallicity correction to the Kennicutt (1998) relation and the resulting SFR estimation can be seen in Fig. 22 (right). The scatter is reduced to 0.26 and 0.20 dex for VIPERS and GSWLC, respectively, compared to 0.3 dex when no correction is applied.

In addition to the metallicity, the coefficient used to convert $L_{[\text{O III}]}$ to SFR also depends on the ionization parameter. In addition to a general [O III]-SFR calibration, Villa-Vélez et al. (2021) established a grid where linear calibrations are given depending on the metallicity and ionization parameter. Based on the [O III]/[O II] ratio and the [O III]/[O II] versus the ionization parameter q for $Z = Z_\odot$ in Kewley & Dopita (2002), we estimated a dimensionless ionization parameter U ($U = q/c$) ranging from −3.5 to −2.2. Using the Z94 calibration, the metallicity ranges from 0.8 to 1.04 $Z_\odot$ so we used the grid values from Villa-Vélez et al. (2021) (shown in their Table 5) at $Z = Z_\odot$ to estimate the SFR based on the estimated U for each galaxy. The SFR comparison is presented in Fig. 23 and they show a good agreement, with a scatter of ∼0.24 dex for VIPERS and GSWLC, despite the fact that we considered the model of Kewley & Dopita (2002) at $Z = Z_\odot$ for every galaxy in VIPERS and GSWLC. We note that the scatter for VIPERS is lower when using the grid of Villa-Vélez et al. (2021) compared to the calibration including a metallicity correction. This confirms that metallicity and the ionization parameter have to be included in a calibration based on [O III].

Some other works have also shown that the [O III] line can trace the SFR of galaxies, but with a significant scatter (Moustakas et al. 2006; Suzuki et al. 2016), as in this work where [O III] is one of the poorest SFR tracers. It is fundamental to better understand what impacts the SFR estimation based on [O III] regarding future observations, as JSWT will be able to detect the [O III] line with $S/N > 20$ at redshifts similar to those of the *Hubble* Deep Field (Chevallard et al. 2019).

5. Discussion

5.1. Derivation of rest-frame luminosity

In this paper, we used the CIGALE SED fitting tool to derive the rest-frame luminosities used for the SFR calibrations. Because SFR comparisons depend on templates and parameters used for CIGALE to model the spectra, we performed an additional test using SEDs reconstructed previously with the *hyperz* tool. Based on the two sets of SED results, we estimated the impact of different templates on the rest-frame luminosity estimations.

The scatter calculated between the absolute magnitudes from *hyperz* and CIGALE is on the order of 0.29 mag for the *ugriz* bands, which corresponds to a scatter of 0.12 dex for the rest-frame luminosity. This low value is mostly due to the excellent coverage of the optical part of the spectra. For the K_s and NUV band, there is a slight increase to 0.34 mag, corresponding to a scatter of 0.14 dex. For the FUV band, the scatter increases to 0.62 mag, corresponding to 0.25 dex in luminosity. This results from the partial and poor coverage at NUV and FUV wavelengths (39% and 84% of galaxies have no NUV and no FUV measurements, respectively), increasing the uncertainty in the UV. This increase is also seen in a mock analysis where the scatter between the true and recovered FUV rest-frame luminosity is higher compared to the other bands (0.06 dex for L_{FUV} and 0.02 dex for the g-band, for instance). The test shows that the choice of templates can significantly influence the absolute magnitude estimation, especially with a poor coverage of photometric measurements, causing the recovery of the SED from the broad band photometry to be less constrained. However, we are more confident with estimations obtained using the CIGALE tool due to the use of Bayesian analysis, rather than *hyperz* where only the best SED is taken into account.

Due to the lack of coverage in the MIR and FIR ranges of wavelength, the dust attenuations' true values are unknown. The low values of dust attenuation used in our fitting process impact the estimation of the blue bands' luminosities, affecting the estimation of IR luminosities due to the principle of energy-balance. We use a subsample of 441 galaxies for which *Herschel* data are

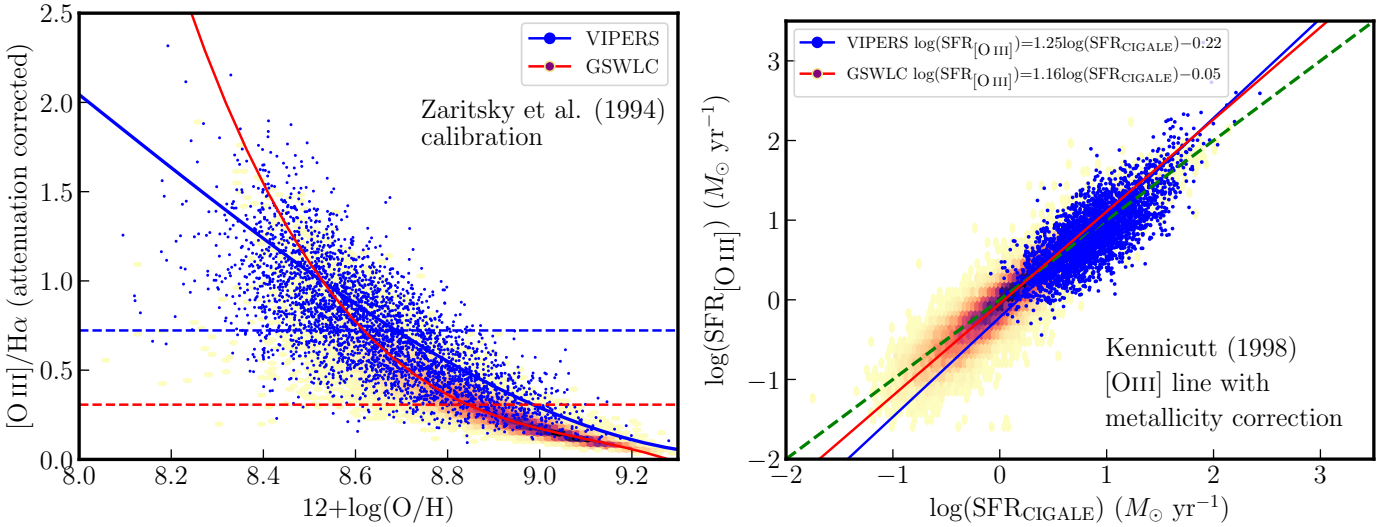


Fig. 22. SFR derived from Hα SFR calibration of Kennicutt (1998) and a metallicity correction. *Left*: [O III]/Hα ratio (assuming Hα = 2.86Hβ) corrected for dust attenuation versus metallicity estimated using the Zaritsky et al. (1994) calibration for the VIPERS (blue) and GSWLC (density) samples, with their associated linear fit. *Right panel*: SFR derived from [O III] using the Hα calibration of Kennicutt (1998) and the attenuation-corrected [O III]/Hα expressed as a function of metallicity (Eq. (11)). Taking into account the metallicity decreases the scatter for both samples (mean of 0.05 dex and scatter of 0.26 dex for VIPERS, 0.04 and 0.20 dex for GSWLC).

available to quantify this influence. We performed two runs similar to the one discussed in Sect. 3.2 using input data from FUV to *Herschel*-500 µm on one side and from u to K_s band on the other side. Comparing the rest-frame luminosity between both runs, we find that the scatter decreases from 0.08 to 0.02 dex (FUV to r-band), then increases from 0.02 to 0.06 dex up to K_s, and finally drastically increases for the 8- and 24-µm bands, and $L_{\rm TIR}$, with a scatter of 0.2 dex. This is the consequence of the energy-balance principle used in CIGALE, where energy attenuated by dust is re-emitted in the infrared wavelengths. In practice, by increasing or decreasing the attenuation in the bluer bands, the observed energy emitted by the stellar population becomes lower or higher, respectively, and finally the luminosity emitted by the dust increases or decreases, respectively, affecting the luminosity in the MIR.

The scatter estimated for the different calibrations, shown in Table E, does not take into account this effect on templates, and is systematically small for calibrations based on photometric bands and spectral lines coming directly from observations, and is smaller compared to GSWLC for which k-corrections are smaller. We suggest that a lower limit on the scatter from FUV to 24 µm should take this factor into account, which, as a first estimation from the scatter from CIGALE versus *hyperz* and CIGALE (FUV-500 µm) versus CIGALE(u-K_s), is equal to 0.26 (FUV), 0.14 (NUV), 0.12 (ugriz), 0.15 (K_s), and 0.20 dex (8, 24 µm and $L_{\rm TIR}$). The variation of this scatter from FUV to $L_{\rm TIR}$ is shown in Fig. 24.

5.2. SFR calibrations for star-forming galaxies from z = 0 to z = 0.9

Comparing two estimates of the same physical parameter given by two different methods can be done using the mean and the scatter between these two estimates. However, it might be difficult to estimate which estimate is closest to the true value when one method gives a significant scatter and a small mean while the other gives a small scatter and a significant mean. In addition, a small value for the mean difference does not necessarily translate as a small offset if the estimates are rotated around $y = x$ (Fig. 6, right). Therefore, we chose to use a test giving a unique number, measuring the precision and accuracy of a method, instead of separately comparing the mean and scatter.

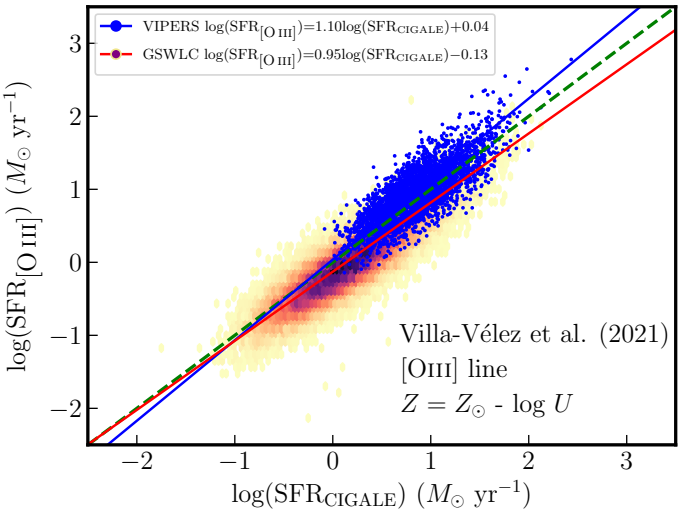


Fig. 23. SFR derived from [O III] using the calibration factors at $Z = Z_\odot$ and depending on U proposed by Villa-Vélez et al. (2021). U was estimated based on [O III]/[O II] and the model of Kewley & Dopita (2002) at $Z = Z_\odot$. The agreement is good with CIGALE SFR (mean of 0.09 dex and scatter of 0.24 dex for VIPERS, 0.19 and 0.24 dex for GSWLC).

To estimate the reliability of SFR calibrations, we computed the concordance correlation coefficient (CCC, Lin 1989). This coefficient is used to compare gold standard measurements (the true SFR estimated with CIGALE in this work) and a new set of measurements obtained with another method (here: another SFR calibration from the literature). The CCC is a combination of the Pearson coefficient, measuring the dispersion from a straight line, and another factor that measures how much the relationship is close to the identity. For the Pearson coefficient, the CCC ranges from -1 to 1. We estimated the CCC for each relation with VIPERS and GSWLC separately.

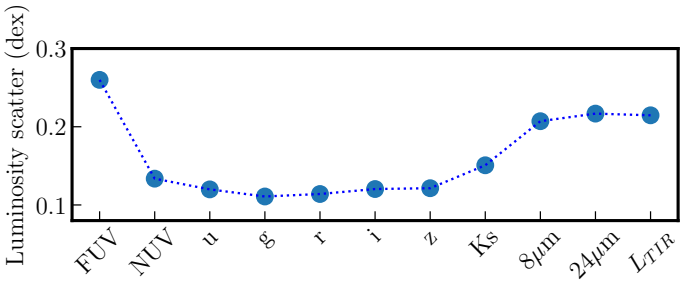


Fig. 24. Evolution of the scatter along different wavelengths ranging from FUV to $L_{\rm TIR}$.

To estimate which relation works the best over the entire redshift range ($0 \leq z \leq 0.9$), we employed the CCC, using both samples at low and intermediate redshifts (referred to as $\rm CCC_{GV}$). Because of the different sample sizes between GSWLC and VIPERS, we constructed a sample of GSWLC galaxies with the same number of galaxies as VIPERS by performing 1000 samplings without replacement, where the median SFR of each sampling should not differ by more than log(SFR) = 0.1 compared to the total GSWLC sample. The CCC and $\rm CCC_{GV}$ are shown in Table E, where the best relation for VIPERS ($0.5 \leq z \leq 0.9$) and GSWLC ($z \leq 0.3$) are underlined in blue, and in magenta for VIPERS and GSWLC simultaneously ($0 \leq z \leq 0.9$). Given that VIPERS measurements are more affected by extrapolations compared to GSWLC, we performed a comparison per band only.

5.2.1. Calibration from the UV bands and the *u*-band

For the FUV band, the relation of Brown et al. (2017) using the Hao et al. (2011) attenuation law gives the best agreement for VIPERS (CCC = 0.99), GSWLC (CCC = 0.88), and both ($\rm CCC_{GV}$ = 0.94). The relation given by Salim et al. (2007), despite giving a worse agreement for GSWLC (0.86), is equally good for VIPERS (0.99) and both samples (0.94). It is reassuring to find a good agreement with another calibration from the literature given the higher uncertainty of the FUV and NUV luminosity. For the *u*-band, a good agreement is found for VIPERS with Zhou et al. (2017), (0.97), and for GSWLC (0.94) with Hopkins et al. (2003) and Davies et al. (2016). However, the relation of Hopkins et al. (2003) gives the best agreement for $0 \leq z \leq 0.9$ with a CCC of 0.97.

5.2.2. Calibration from MIR bands

In agreement with the literature (e.g., Schreiber et al. 2018; Gregg et al. 2022), 8 μm only gives a rough estimation of the SFR, the best calibration being given by Brown et al. (2017) with a CCC of 0.91, while the others relations give a poor CCC when applied to the VIPERS sample (<0.78). All the calibrations tested at 24 μm give a high and close $\rm CCC_{GV}$, the highest being given by the relation of Zhu et al. (2008), which is when the nonlinearity of L_{24} versus SFR is taken into account and the calibration is established for the whole galaxy.

5.2.3. Calibrations from multiple bands

Between all the calibrations, composite tracers give the best $\rm CCC_{GV}$ with the calibration of Boquien et al. (2014), with the weighting coefficient for L_{24} from Hao et al. (2011) giving the highest one ($\rm CCC_{GV}$ = 0.99). This is not surprising as no attenuation law has to be used, and these composite calibrations retrieve the unobscured and obscured SFR of galaxies.

5.2.4. Calibrations from spectral lines

For spectral lines, Hβ is a good tracer, in particular for GSWLC (CCC = 0.92) given its relation with Hα. For VIPERS, the lower CCC of 0.87 for VIPERS might come from our treatment of the stellar absorption, taken to be equal to 2 Å for each galaxy, while this correction was done automatically for GSWLC. Given the assumptions on Hβ, we would need Hα measurements to understand if this lower CCC is due to a deviation from the Kennicutt (1998) calibration or due to the corrections and conversion factor with Hβ.

The [O II] line gives a reliable estimation of SFR, and the agreement improves when the samples are corrected for reddening and metallicity. When this last correction is applied, the [O II] line has the same $\rm CCC_{GV}$ as Hβ. We note that the calibration of Gilbank et al. (2010) gives a slightly better estimation compared to the one corrected for metallicity for GSWLC galaxies (CCC = 0.91). The assumptions for the attenuation ($A_{\rm H\alpha}$ = 1 mag) and metallicity corrections (derived from SDSS DR4) in the calibration of Gilbank et al. (2010) naturally explains this good agreement and, at the same time, the worse agreement with VIPERS, for which $A_{\rm H\alpha}$ and metallicity are found to be different. In agreement with our work and Gilbank et al. (2010), Kewley & Dopita (2002) tested their [O II] calibration based on the Nearby Field Galaxies Survey (NFGS) from Hicks et al. (2002) and Tresse et al. (2002) at $0.5 < z < 1.6$, and showed that the [O II] line is a reliable tracer of SFR (~0.17 dex) when the metallicity is taken into account.

The same applies to the SFR estimated with [O III] where the metallicity correction improves the estimation, increasing $\rm CCC_{GV}$ from 0.81 to 0.91. The relation of Villa-Vélez et al. (2021) gives a slightly better estimation for VIPERS when the metallicity and the ionization parameter are included. A more extended grid associated with models to derive the ionization parameter would be useful, with the aim of giving a better estimation of the SFR from the [O III] spectral line.

5.2.5. Calibrations from GSWLC and VIPERS

Using both GSWLC and VIPERS, we derived our own set of SFR calibrations for single-band tracers. We remind the reader that these calibrations were obtained for star-forming galaxies selected through the BPT diagram, and whose SFR and attenuation-corrected rest-frame luminosities were estimated using CIGALE, assuming a Chabrier (2003) IMF (Table 6).

The FUV and NUV calibrations are close to the those established by Salim et al. (2007) at low redshifts. For the *u*-band, we did not apply any correction for the old stellar population contamination as it is difficult to accurately remove. However, it implies that the *u*-band SFR calibration is restricted to star-forming galaxies that have similar contamination. If using a *u*-band luminosity that had been decontaminated of the old stellar population, we found that a factor of 0.64 should be applied to L_u in order to recover the luminosity contribution from young stars. For 8 μm, we removed the stellar contamination (~5% in average) as explained in Sect. 4.1.3. Contrary to the other bands, this calibration is obtained using VIPERS data only, and extrapolation to the local Universe should be considered with caution. At 24 μm, the WISE-4 luminosity from GSWLC is converted into a 24-μm luminosity (Sect. 4.1.3) before performing the fit.

Table 6. SFR calibrations, based on the Chabrier (2003) IMF, for each band and line.

$$\log[\mathrm{SFR}_{\mathrm{band}}\ (M_\odot\ \mathrm{yr}^{-1})] = A \times \log[L_{\mathrm{band}}(\mathrm{units})] + B$$

Rest-frame band [(1)]	A	B	Luminosity range	Unit
FUV	1.04 ± 0.01	-21.99 ± 0.02	$2.1 \times 10^{19} < L < 4.7 \times 10^{23}$	W Hz^{-1}
NUV	1.03 ± 0.01	-21.81 ± 0.01	$3.9 \times 10^{19} < L < 4.3 \times 10^{23}$	W Hz^{-1}
u-band	1.11 ± 0.0	-23.62 ± 0.01	$8.3 \times 10^{19} < L < 4.5 \times 10^{23}$	W Hz^{-1}
8 μm	0.85 ± 0.01	-18.53 ± 0.14	$3.9 \times 10^{21} < L < 4.4 \times 10^{24}$	W Hz^{-1}
24 μm	0.81 ± 0.0	-18.22 ± 0.01	$7.3 \times 10^{20} < L < 2.6 \times 10^{25}$	W Hz^{-1}
L_{TIR}	0.99 ± 0.01	-9.97 ± 0.03	$3.7 \times 10^{8} < L < 4.8 \times 10^{12}$	$L_\odot$
Hβ	0.94 ± 0.01	-38.34 ± 0.04	$9.3 \times 10^{38} < L < 1.0 \times 10^{44}$	erg s^{-1}
[O II]λ3727	0.96 ± 0.01	-39.69 ± 0.07	$6.4 \times 10^{39} < L < 1.1 \times 10^{44}$	erg s^{-1}
[O III]λ5007	0.89 ± 0.01	-35.94 ± 0.35	$4.4 \times 10^{38} < L < 6.1 \times 10^{43}$	erg s^{-1}

Notes. [(1)]The rest-frame fluxes are corrected for attenuation.

Calibrations based on the u-band, and 8 and 24 μm are found to be nonlinear as the luminosity does not directly trace the SFR, and some other effects have to be taken into account: old-stellar population contamination and variation due to stellar evolution for the u-band, metallicity dependence of the PAHs at 8 μm, and self-absorption and transparency for the 24-μm band. On the contrary, the linearity of the SFR calibration based on L_{TIR} shows that this property is a reliable and direct tracer of the SFR up to $z \sim 0.9$. For the [O II] and [O III] lines, the metallicity is already included, so no additional corrections are needed in order to use them. The strong nonlinearity of the SFR-[O III] calibration may reflect the dependence on metallicity and the ionization parameter suffered by this spectral line.

6. Conclusions

We used VIPERS, a spectroscopic survey based on CFHTLS galaxies, with $0.5 < z < 0.9$ and measurements from FUV to FIR bands including Hβ, [O II]λ3727 and [O III]$\lambda\lambda$4959,5007 spectral lines. We tested different SFR recipes from the literature, mainly calibrated on local galaxies, to check how consistent those calibrations are at intermediate redshifts. For comparison purposes, we used GSWLC, a catalog of local galaxies based on SDSS data merged with GALEX and WISE ($z < 0.3$) data. For both the VIPERS and GSWLC catalogs, the physical parameters were derived using the CIGALE code, in particular the SFR, which is considered to be the reference SFR in this work. The main conclusions are:

– In the blue part of the spectrum, the FUV and NUV bands can be excellent tracers of SFR up to $z \sim 0.9$, using the calibrations of Brown et al. (2017; scatter of 0.05 and 0.25 dex for VIPERS and GSWLC, respectively for the FUV band) and Salim et al. (2007; scatter of 0.03 and 0.24 dex for VIPERS and GSWLC, respectively for the NUV band). The attenuation should be adequately corrected and we calibrated the $A_{\mathrm{UV}} - \beta_{\mathrm{UV}}$ relation for VIPERS for the FUV and NUV bands.

– We estimated the contamination by the old stellar population in the u-band to be on the order of 36%. Up to $z \sim 0.9$, the calibration of Hopkins et al. (2003), taking into account the contamination and stellar evolution through a nonlinear calibrations, gives the best SFR estimations (scatter of 0.08 and 0.09 dex for VIPERS and GSWLC, respectively) up to $z \sim 0.9$. However, such calibrations should be limited to galaxies suffering roughly from the same old stellar population contamination.

– The luminosity at 8 μm, dominated by PAH emission, is correlated with the SFR, but calibrations tested in this work underestimate the SFR compared to the one obtained with CIGALE. The calibration giving the best agreement with CIGALE is given by Brown et al. (2017) (scatter of 0.10 dex with a mean difference of 0.10 dex). More work is needed to understand PAH physics and how PAHs are impacted by metallicity to derive, if possible, more accurate calibrations. This is particularly important in the context of future JWST observations.

– 24 μm is an excellent SFR tracer, and previous calibrations are found to work very well, in particular when the calibrations are based on whole galaxies and take into account the nonlinear behavior of $L_{24\,\mu\mathrm{m}}$ with respect to the SFR. The calibration of Zhu et al. (2008) gives the best agreement (scatter of 0.08 dex with a mean difference of 0.12 dex). If WISE-4 observations are able to reliably estimate the SFR, this is not true beyond the local Universe, as they are not sensitive enough and can only be considered as upper limits.

– Composite tracers are part of the best SFR indicators as they do not rely on attenuation prescriptions and are able to associate unobscured and obscured SFRs. Up to $z \sim 0.9$, the calibration of Boquien et al. (2014)/Hao et al. (2011) is in good agreement with CIGALE (scatter of 0.03 and 0.10 dex for VIPERS and GSWLC). However, the need for two bands, or more, make them less practical than single-band SFR calibrations. For VIPERS and GSWLC, we estimated the dust emission to be contaminated by the old stellar population by 11% and 45% for VIPERS and GSWLC, respectively.

– Estimation of rest-frame luminosity from CIGALE is impacted from the choice of templates and wavelength coverage of the SED. By comparing our CIGALE luminosity estimations with those from *hyperz* and CIGALE runs, with and without IR coverage, the impact ranges from 0.12 to 0.26 dex depending on the band considered.

– The spectral line Hβ gives a reliable estimation of the SFR up to $z \sim 0.9$ (scatter of 0.19 dex for VIPERS and GSWLC), and is therefore a good alternative when Hα is not observed.

In GSWLC and VIPERS, the [O II] and [O III] lines' strengths are higher and easier to observe, making an SFR calibration based on them particularly important for future surveys. The [O II] spectral line gives also a good estimation of the SFR, reaching an equivalent accuracy compared to Hβ when the metallicity dependence, through the R_{23} parameter in this work, is taken into account (scatter of 0.17 and 0.20 dex for VIPERS

and GSWLC, respectively). The [O III] is one of the least accurate SFR indicators, the calibrations being different between local and intermediate redshift galaxies in addition to showing a high scatter (scatter of 0.31 and 0.32 dex for VIPERS and GSWLC, respectively). A correction for metallicity is mandatory to reliably recover the SFR (scatter of 0.26 and 0.20 dex for VIPERS and GSWLC, respectively). In addition, this calibration also depends on the ionization parameter of the galaxies considered. Calibrations using the metallicity-ionization parameter grid proposed by Villa-Vélez et al. (2021) gives good SFR estimations (scatter of 0.24 dex for VIPERS and GSWLC).

– We calibrated the FUV, NUV, u-, 8-µm, and 24 µm bands, $L_{\rm TIR}$, and the Hβ, [O II]λ3727 and [O III]λ5007 spectral lines, based on the SFR derived with CIGALE in the range $0 < z < 0.9$ for star-forming galaxies. Those relations are in the form $\log[\mathrm{SFR}_{\rm band}\ (M_\odot\ \mathrm{yr}^{-1})] = A \times \log[L_{\rm band}] + B$ where the luminosity in the band $L_{\rm band}$ has to be corrected for dust attenuation. We did not account for old stellar population correction for the u-band and $L_{\rm TIR}$, but this contribution can be removed based on the average values given in this work. The [O II]λ3727 and [O III]λ5007 calibration are not corrected for metallicity.

Acknowledgements. We thank the anonymous referee for the useful comments and suggestions. This research was supported by the Polish National Science Centre via grants UMO-2018/30/M/ST9/00757 and UMO-2018/30/E/ST9/00082, and by Polish Ministry of Science and Higher Education grant DIR/WK/2018/12. M.F. acknowledges support from the First TEAM grant of the Foundation for Polish Science No. POIR.04.04.00-00-5D21/18-00 (PI: A. Karska). This paper uses data from the VIMOS Public Extragalactic Redshift Survey (VIPERS). VIPERS has been performed using the ESO Very Large Telescope, under the "Large Programme" 182.A-0886. The participating institutions and funding agencies are listed at http://vipers.inaf.it. We thank B. Garilli for the line measurements for the VIPERS sample. MB gratefully acknowledges support by the ANID BASAL project FB210003 and the FONDECYT regular grant 1211000.

References

Ahn, C. P., Alexandroff, R., Allende Prieto, C., et al. 2014, ApJS, 211, 17
Alonso-Herrero, A., Rieke, G. H., Rieke, M. J., et al. 2006, ApJ, 650, 835
Anderson, L. D., Bania, T. M., Balser, D. S., et al. 2014, ApJS, 212, 1
Arnouts, S., Le Floc'h, E., Chevallard, J., et al. 2013, A&A, 558, A67
Baes, M., Verstappen, J., De Looze, I., et al. 2011, ApJS, 196, 22
Baldwin, J. A., Phillips, M. M., & Terlevich, R. 1981, PASP, 93, 5
Battisti, A. J., Calzetti, D., Johnson, B. D., & Elbaz, D. 2015, ApJ, 800, 143
Battisti, A. J., Calzetti, D., & Chary, R. R. 2017, ApJ, 851, 90
Bell, E. F. 2003, ApJ, 586, 794
Bell, E. F., Papovich, C., Wolf, C., et al. 2005, ApJ, 625, 23
Berman, L. 1936, MNRAS, 96, 890
Berta, S., Lutz, D., Santini, P., et al. 2013, A&A, 551, A100
Bianchi, L., Conti, A., & Shiao, B. 2014, Adv. Space Res., 53, 900
Blanton, M. R., Bershady, M. A., Abolfathi, B., et al. 2017, AJ, 154, 28
Bogdanoska, J., & Burgarella, D. 2020, MNRAS, 496, 5341
Boissier, S. 2013, in Star Formation in Galaxies, eds. T. D. Oswalt, & W. C. Keel, 6, 141
Boissier, S., Prantzos, N., Boselli, A., & Gavazzi, G. 2003, MNRAS, 346, 1215
Bolzonella, M., Miralles, J. M., & Pelló, R. 2000, A&A, 363, 476
Bolzonella, M., Kovač, K., Pozzetti, L., et al. 2010, A&A, 524, A76
Bongiorno, A., Mignoli, M., Zamorani, G., et al. 2010, A&A, 510, A56
Boquien, M., & Salim, S. 2021, A&A, 653, A149
Boquien, M., Buat, V., & Perret, V. 2014, A&A, 571, A72
Boquien, M., Kennicutt, R., Calzetti, D., et al. 2016, A&A, 591, A6
Boquien, M., Burgarella, D., Roehlly, Y., et al. 2019, A&A, 622, A103
Bouchet, P., Lequeux, J., Maurice, E., Prevot, L., & Prevot-Burnichon, M. L. 1985, A&A, 149, 330
Brinchmann, J., Charlot, S., White, S. D. M., et al. 2004, MNRAS, 351, 1151
Brown, M. J. I., Jarrett, T. H., & Cluver, M. E. 2014a, PASA, 31, e049
Brown, M. J. I., Moustakas, J., Smith, J. D. T., et al. 2014b, ApJS, 212, 18
Brown, M. J. I., Moustakas, J., Kennicutt, R. C., et al. 2017, ApJ, 847, 136
Bruzual, G., & Charlot, S. 2003, MNRAS, 344, 1000
Buat, V. 2015 Introduction to Cosmology, eds. M. Biernacka, K. Bajan, G. Stachowski, & P. Flin, 134
Buat, V., Takeuchi, T. T., Iglesias-Páramo, J., et al. 2007, ApJS, 173, 404
Buat, V., Boissier, S., Burgarella, D., et al. 2008, A&A, 483, 107
Buat, V., Giovannoli, E., Heinis, S., et al. 2011a, A&A, 533, A93
Buat, V., Giovannoli, E., Takeuchi, T. T., et al. 2011b, A&A, 529, A22
Buat, V., Boquien, M., Małek, K., et al. 2018, A&A, 619, A135
Buat, V., Ciesla, L., Boquien, M., Małek, K., & Burgarella, D. 2019, A&A, 632, A79
Burgarella, D., Buat, V., & Iglesias-Páramo, J. 2005, MNRAS, 360, 1413
Calzetti, D. 2013, in Secular Evolution of Galaxies, eds. J. Falcón-Barroso, & J. H. Knapen, (Cambridge, UK: Cambridge University Press) 419
Calzetti, D., Kinney, A. L., & Storchi-Bergmann, T. 1994, ApJ, 429, 582
Calzetti, D., Armus, L., Bohlin, R. C., et al. 2000, ApJ, 533, 682
Calzetti, D., Kennicutt, R. C., Engelbracht, C. W., et al. 2007, ApJ, 666, 870
Calzetti, D., Wu, S. Y., Hong, S., et al. 2010, ApJ, 714, 1256
Camps, P., & Baes, M. 2015, Astron. Comput., 9, 20
Cardelli, J. A., Clayton, G. C., & Mathis, J. S. 1989, ApJ, 345, 245
Casey, C. M. 2012, MNRAS, 425, 3094
Cassarà, L. P., Maccagni, D., Garilli, B., et al. 2016, A&A, 593, A9
Chabrier, G. 2003, PASP, 115, 763
Charlot, S., & Fall, S. M. 2000, ApJ, 539, 718
Charlot, S., & Longhetti, M. 2001, MNRAS, 323, 887
Chary, R., & Elbaz, D. 2001, ApJ, 556, 562
Chevallard, J., Curtis-Lake, E., Charlot, S., et al. 2019, MNRAS, 483, 2621
Ciesla, L., Boquien, M., Boselli, A., et al. 2014, A&A, 565, A128
Ciesla, L., Boselli, A., Elbaz, D., et al. 2016, A&A, 585, A43
Ciesla, L., Elbaz, D., & Fensch, J. 2017, A&A, 608, A41
Clark, C. J. R., Dunne, L., Gomez, H. L., et al. 2015, MNRAS, 452, 397
Cluver, M. E., Jarrett, T. H., Hopkins, A. M., et al. 2014, ApJ, 782, 90
Cluver, M. E., Jarrett, T. H., Dale, D. A., et al. 2017, ApJ, 850, 68
Colless, M., Dalton, G., Maddox, S., et al. 2001, MNRAS, 328, 1039
Colless, M., Peterson, B. A., Jackson, C., et al. 2003, ArXiv e-prints [arXiv:astro-ph/0306581]
Cullen, F., Cirasuolo, M., Kewley, L. J., et al. 2016, MNRAS, 460, 3002
da Cunha, E., Charlot, S., Dunne, L., Smith, D., & Rowlands, K. 2012, in The Spectral Energy Distribution of Galaxies – SED 2011, eds. R. J. Tuffs, & C. C. Popescu, IAU Symp., 284, 292
Dale, D. A., & Helou, G. 2002, ApJ, 576, 159
Dale, J. E., Ngoumou, J., Ercolano, B., & Bonnell, I. A. 2014, MNRAS, 442, 694
Davidzon, I., Bolzonella, M., Coupon, J., et al. 2013, A&A, 558, A23
Davies, L. J. M., Driver, S. P., Robotham, A. S. G., et al. 2016, MNRAS, 461, 458
Davies, L. J. M., Robotham, A. S. G., Driver, S. P., et al. 2018, MNRAS, 480, 768
De Barros, S., Reddy, N., & Shivaei, I. 2016, ApJ, 820, 96
De Looze, I., Fritz, J., Baes, M., et al. 2014, A&A, 571, A69
Donas, J., & Deharveng, J. M. 1984, A&A, 140, 325
Draine, B. T., Dale, D. A., Bendo, G., et al. 2007, ApJ, 663, 866
Draine, B. T., Aniano, G., Krause, O., et al. 2014, ApJ, 780, 172
Driver, S. P., Wright, A. H., Andrews, S. K., et al. 2016, MNRAS, 455, 3911
Driver, S. P., Andrews, S. K., da Cunha, E., et al. 2018, MNRAS, 475, 2891
Elbaz, D., Hwang, H. S., Magnelli, B., et al. 2010, A&A, 518, L29
Engelbracht, C. W., Gordon, K. D., Rieke, G. H., et al. 2005, ApJ, 628, L29
Ferland, G. J., Porter, R. L., van Hoof, P. A. M., et al. 2013, Rev. Mex. Astron. Astrofis., 49, 137
Figueira, M., Zavagno, A., Deharveng, L., et al. 2017, A&A, 600, A93
Fioc, M., & Rocca-Volmerange, B. 1997, A&A, 326, 950
Fritz, J., Franceschini, A., & Hatziminaoglou, E. 2006, MNRAS, 366, 767
Fukugita, M., Ichikawa, T., Gunn, J. E., et al. 1996, AJ, 111, 1748
García, P., Bronfman, L., Nyman, L.-Å., Dame, T. M., & Luna, A. 2014, ApJS, 212, 2
Garilli, B., Le Fèvre, O., Guzzo, L., et al. 2008, A&A, 486, 683
Garilli, B., Fumana, M., Franzetti, P., et al. 2010, PASP, 122, 827
Garilli, B., Guzzo, L., Scodeggio, M., et al. 2014, A&A, 562, A23
Gilbank, D. G., Baldry, I. K., Balogh, M. L., Glazebrook, K., & Bower, R. G. 2010, MNRAS, 405, 2594
Giovannoli, E., Buat, V., Noll, S., Burgarella, D., & Magnelli, B. 2011, A&A, 525, A150
Goranova, Y., Hudelot, P., & Magnard, F. 2009, The CFHTLS T0006 Release, http://terapix.iap.fr/cplt/table_syn_T0006.html
Goto, T., Okamura, S., Sekiguchi, M., et al. 2003, PASJ, 55, 757
Gregg, B., Calzetti, D., & Heyer, M. 2022, ApJ, 928, 120
Groves, B., Brinchmann, J., & Walcher, C. J. 2012, MNRAS, 419, 1402
Guzzo, L., & VIPERS Team 2013, The Messenger, 151, 41
Hao, C.-N., Kennicutt, R. C., Johnson, B. D., et al. 2011, ApJ, 741, 124
Hicks, E. K. S., Malkan, M. A., Teplitz, H. I., McCarthy, P. J., & Yan, L. 2002, ApJ, 581, 205
Hippelein, H., Maier, C., Meisenheimer, K., et al. 2003, A&A, 402, 65

Hirashita, H., Buat, V., & Inoue, A. K. 2003, A&A, 410, 83
Holden, B. P., Oesch, P. A., González, V. G., et al. 2016, ApJ, 820, 73
Hopkins, A. M., Miller, C. J., Nichol, R. C., et al. 2003, ApJ, 599, 971
Hummer, D. G., & Storey, P. J. 1987, MNRAS, 224, 801
Inoue, A. K. 2011, MNRAS, 415, 2920
Jarrett, T. H., Chester, T., Cutri, R., et al. 2000, AJ, 119, 2498
Jarrett, T. H., Masci, F., Tsai, C. W., et al. 2013, AJ, 145, 6
Jones, A. P., Köhler, M., Ysard, N., Bocchio, M., & Verstraete, L. 2017, A&A, 602, A46
Kauffmann, G., Heckman, T. M., Tremonti, C., et al. 2003, MNRAS, 346, 1055
Kennicutt, R. C., Jr 1983, ApJ, 272, 54
Kennicutt, R. C., Jr 1998, ARA&A, 36, 189
Kennicutt, R. C., Jr, & Evans, N. J. 2012, ARA&A, 50, 531
Kennicutt, R. C., Jr, Tamblyn, P., & Congdon, C. E. 1994, ApJ, 435, 22
Kennicutt, R. C., Jr, Hao, C.-N., Calzetti, D., et al. 2009, ApJ, 703, 1672
Kewley, L. J., & Dopita, M. A. 2002, ApJS, 142, 35
Kewley, L. J., Dopita, M. A., Sutherland, R. S., Heisler, C. A., & Trevena, J. 2001, ApJ, 556, 121
Kewley, L. J., Geller, M. J., & Jansen, R. A. 2004, AJ, 127, 2002
Kewley, L. J., Maier, C., Yabe, K., et al. 2013, ApJ, 774, L10
Kewley, L. J., Zahid, H. J., Geller, M. J., et al. 2015, ApJ, 812, L20
Kobulnicky, H. A., Kennicutt, Jr., R. C., & Pizagno, J. L. 1999, ApJ, 514, 544
Komatsu, E., Smith, K. M., Dunkley, J., et al. 2011, ApJS, 192, 18
Kroupa, P. 2002, Science, 295, 82
Lamareille, F. 2010, A&A, 509, A53
Lamareille, F., Brinchmann, J., Contini, T., et al. 2009, A&A, 495, 53
Lang, D., Hogg, D. W., & Schlegel, D. J. 2016, AJ, 151, 36
Le Fèvre, O., Saisse, M., Mancini, D., et al. 2003, in Proc. SPIE, eds. M. Iye, & A. F. M. Moorwood, SPIE Conf. Ser., 4841, 1670
Le Fèvre, O., Vettolani, G., Garilli, B., et al. 2005, A&A, 439, 845
Liang, Y. C., Yin, S. Y., Hammer, F., et al. 2006, ApJ, 652, 257
Lilly, S. J., Tresse, L., Hammer, F., Crampton, D., & Le Fevre, O. 1995, ApJ, 455, 108
Lin, L. I.-K. 1989, Biometrics, 45, 255
Lo Faro, B., Buat, V., Roehlly, Y., et al. 2017, MNRAS, 472, 1372
Ly, C., Malkan, M. A., Kashikawa, N., et al. 2007, ApJ, 657, 738
Madau, P., & Dickinson, M. 2014, ARA&A, 52, 415
Madau, P., Ferguson, H. C., Dickinson, M. E., et al. 1996, MNRAS, 283, 1388
Madden, S. C., Galliano, F., Jones, A. P., & Sauvage, M. 2006, A&A, 446, 877
Magdis, G. E., Daddi, E., Béthermin, M., et al. 2012, ApJ, 760, 6
Magnelli, B., Lutz, D., Berta, S., et al. 2010, A&A, 518, L28
Maier, C., Ziegler, B. L., Lilly, S. J., et al. 2015, A&A, 577, A14
Małek, K., Buat, V., Roehlly, Y., et al. 2018, A&A, 620, A50
Maraston, C. 2005, MNRAS, 362, 799
Martin, D. C., Fanson, J., Schiminovich, D., et al. 2005, ApJ, 619, L1
McCarthy, P. J., Yan, L., Freudling, W., et al. 1999, ApJ, 520, 548
McGaugh, S. S. 1991, ApJ, 380, 140
Meurer, G. R., Heckman, T. M., & Calzetti, D. 1999, ApJ, 521, 64
Miller, N. A., & Owen, F. N. 2002, AJ, 124, 2453
Moustakas, J., & Kennicutt, R. C., Jr 2006, ApJS, 164, 81
Moustakas, J., Kennicutt, R. C., Jr, & Tremonti, C. A. 2006, ApJ, 642, 775
Moutard, T., Arnouts, S., Ilbert, O., et al. 2016a, A&A, 590, A103
Moutard, T., Arnouts, S., Ilbert, O., et al. 2016b, A&A, 590, A102
Nagao, T., Maiolino, R., & Marconi, A. 2006, A&A, 459, 85
Nersesian, A., Xilouris, E. M., Bianchi, S., et al. 2019, A&A, 624, A80
Noll, S., Burgarella, D., Giovannoli, E., et al. 2009, A&A, 507, 1793
Nordon, R., Lutz, D., Shao, L., et al. 2010, A&A, 518, L24
Nordon, R., Lutz, D., Genzel, R., et al. 2012, ApJ, 745, 182
O'Donnell, J. E. 1994, ApJ, 422, 158
Oke, J. B. 1974, ApJS, 27, 21
Pagel, B. E. J., Edmunds, M. G., Blackwell, D. E., Chun, M. S., & Smith, G. 1979, MNRAS, 189, 95
Peek, J. E. G., & Schiminovich, D. 2013, ApJ, 771, 68
Pérez-González, P. G., Kennicutt, Jr., R. C., Gordon, K. D., et al. 2006, ApJ, 648, 987
Pforr, J., Maraston, C., & Tonini, C. 2012, MNRAS, 422, 3285
Pilyugin, L. S. 2001, A&A, 369, 594
Pope, A., Chary, R.-R., Alexander, D. M., et al. 2008, ApJ, 675, 1171
Popescu, C. C., Tuffs, R. J., Dopita, M. A., et al. 2011, A&A, 527, A109
Prescott, M., Baldry, I. K., & James, P. A. 2009, MNRAS, 397, 90
Prevot, M. L., Lequeux, J., Maurice, E., Prevot, L., & Rocca-Volmerange, B. 1984, A&A, 132, 389
Relaño, M., Lisenfeld, U., Pérez-González, P. G., Vílchez, J. M., & Battaner, E. 2007, ApJ, 667, L141
Rieke, G. H., Alonso-Herrero, A., Weiner, B. J., et al. 2009, ApJ, 692, 556
Rosa-González, D., Terlevich, E., & Terlevich, R. 2002, MNRAS, 332, 283
Salim, S., Rich, R. M., Charlot, S., et al. 2007, ApJS, 173, 267
Salim, S., Lee, J. C., Janowiecki, S., et al. 2016, ApJS, 227, 2
Salim, S., Boquien, M., & Lee, J. C. 2018, ApJ, 859, 11
Salpeter, E. E. 1955, ApJ, 121, 161
Schlegel, D. J., Finkbeiner, D. P., & Davis, M. 1998, ApJ, 500, 525
Schreiber, C., Elbaz, D., Pannella, M., et al. 2018, A&A, 609, A30
Scodeggio, M., Guzzo, L., Garilli, B., et al. 2018, A&A, 609, A84
Searle, L., Sargent, W. L. W., & Bagnuolo, W. G. 1973, ApJ, 179, 427
Senarath, M. R., Brown, M. J. I., Cluver, M. E., et al. 2018, ApJ, 869, L26
Shipley, H. V., Papovich, C., Rieke, G. H., Brown, M. J. I., & Moustakas, J. 2016, ApJ, 818, 60
Shirley, R., Roehlly, Y., Hurley, P. D., et al. 2019, MNRAS, 490, 634
Shirley, R., Duncan, K., Campos Varillas, M. C., et al. 2021, MNRAS, 507, 129
Smolčić, V., Schinnerer, E., Zamorani, G., et al. 2009, ApJ, 690, 610
Stalevski, M., Fritz, J., Baes, M., Nakos, T., & Popović, L. Č. 2012, MNRAS, 420, 2756
Stalevski, M., Ricci, C., Ueda, Y., et al. 2016, MNRAS, 458, 2288
Steidel, C. C., Rudie, G. C., Strom, A. L., et al. 2014, ApJ, 795, 165
Straughn, A. N., Pirzkal, N., Meurer, G. R., et al. 2009, AJ, 138, 1022
Suzuki, T. L., Kodama, T., Sobral, D., et al. 2016, MNRAS, 462, 181
Talia, M., Cimatti, A., Pozzetti, L., et al. 2015, A&A, 582, A80
Teplitz, H. I., Malkan, M. A., Steidel, C. C., et al. 2000, ApJ, 542, 18
Tremonti, C. A., Heckman, T. M., Kauffmann, G., et al. 2004, ApJ, 613, 898
Tresse, L., Maddox, S. J., Le Fèvre, O., & Cuby, J. G. 2002, MNRAS, 337, 369
Viaene, S., Baes, M., Bendo, G., et al. 2016, A&A, 586, A13
Villa-Vélez, J. A., Buat, V., Theulé, P., Boquien, M., & Burgarella, D. 2021, A&A, 654, A153
Wild, V., Charlot, S., Brinchmann, J., et al. 2011, MNRAS, 417, 1760
Wilkins, S. M., Gonzalez-Perez, V., Lacey, C. G., & Baugh, C. M. 2012, MNRAS, 424, 1522
Wright, E. L., Eisenhardt, P. R. M., Mainzer, A. K., et al. 2010, AJ, 140, 1868
Wu, H., Cao, C., Hao, C.-N., et al. 2005, ApJ, 632, L79
Wuyts, S., Labbé, I., Förster Schreiber, N. M., et al. 2008, ApJ, 682, 985
York, D. G., Adelman, J., Anderson, J. E., Jr, et al. 2000, AJ, 120, 1579
Young, J. E., Gronwall, C., Salzer, J. J., & Rosenberg, J. L. 2014, MNRAS, 443, 2711
Yuan, H. B., Liu, X. W., & Xiang, M. S. 2013, MNRAS, 430, 2188
Zaritsky, D., Kennicutt, R. C., Jr, & Huchra, J. P. 1994, ApJ, 420, 87
Zhou, Z., Zhou, X., Wu, H., et al. 2017, ApJ, 835, 70
Zhu, Y.-N., Wu, H., Cao, C., & Li, H.-N. 2008, ApJ, 686, 155
Zhuang, M.-Y., & Ho, L. C. 2019, ApJ, 882, 89

Appendix A: CIGALE results

A.1. Mock analysis

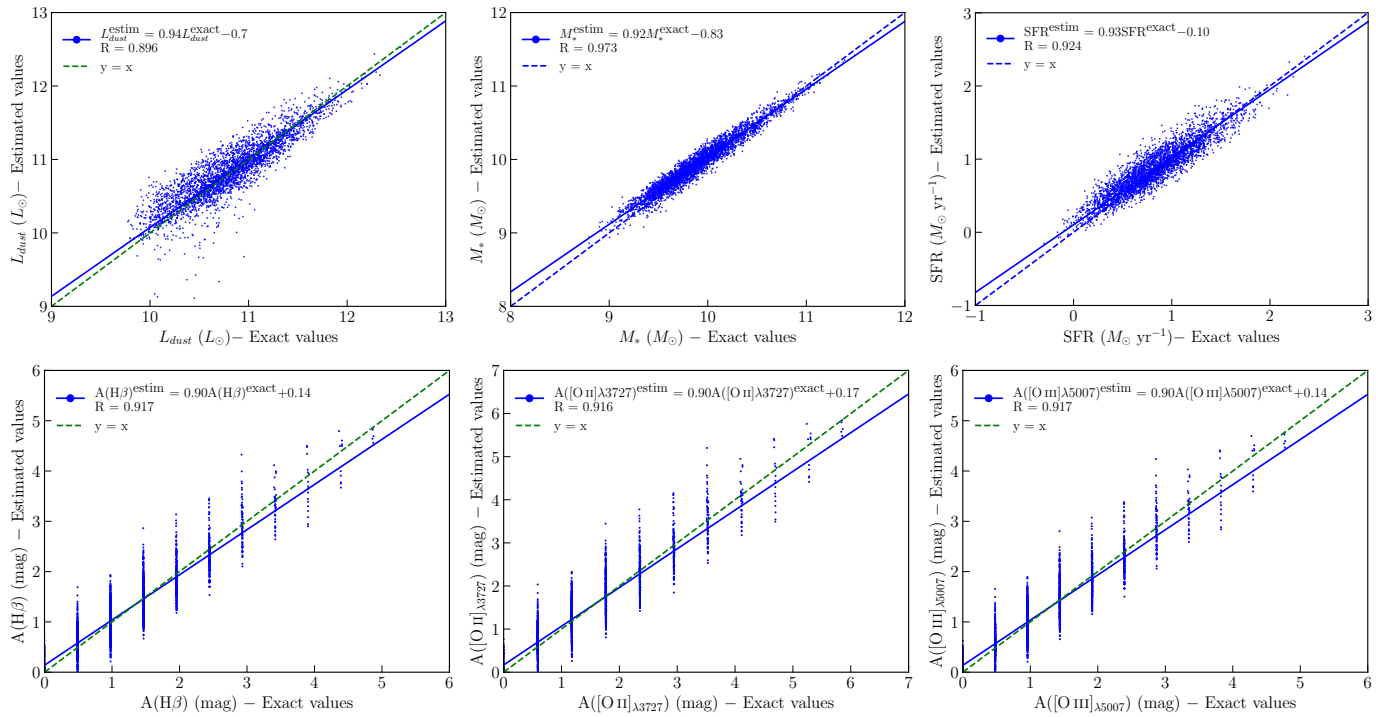


Fig. A.1. Mock analysis of the CIGALE run: parameters estimated by CIGALE versus exact parameters (top left: L_{dust}, top middle: M_*, top right: SFR, bottom left: Hβ attenuation, bottom middle: [O II]λ3727 attenuation, bottom right: [O III]λ5007 attenuation. The blue lines and green lines represent the fit to the data and the one-to-one relation, respectively. The equation of the fit and the Pearson correlation coefficient R are indicated in each plot.

A.2. Examples of SEDs

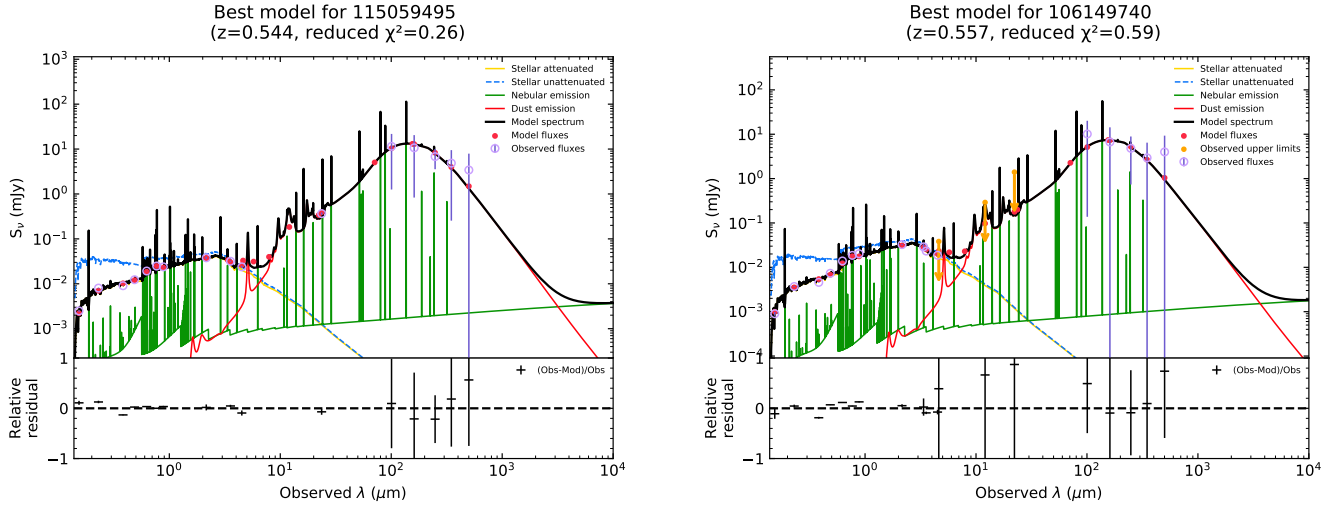


Fig. A.2. Best SEDs for the VIPERS 115059495 and VIPERS 106149740 galaxies reconstructed with CIGALE. VIPERS 106149740 is an example of a galaxy for which the WISE-2, WISE-3, and WISE-4 measurements are upper limits (orange arrows).

Appendix B: List of the calibrations

B.1. UV bands

Brown et al. (2017) – *GALEX*-SDSS DR3 (66 nearby galaxies at $D < 10$ Mpc) – Kroupa IMF

$$\log(\mathrm{SFR})(M_\odot\ \mathrm{yr}^{-1}) = \frac{f - B}{A} - 1.26 \tag{B.1}$$

$f = \log(L_{FUV}) + 2(M_{FUV} - M_{NUV})$ with $A = 0.9$ and $B = 42.25$ [Calzetti et al. (2000) attenuation law] (B.2)

$f = \log(L_{FUV}) + 1.532(M_{FUV} - M_{NUV}) - 0.033$ with $A = 0.96$ and $B = 42.42$ [Hao et al. (2011) attenuation law] (B.3)

Davies et al. (2016) – GAMA II survey (3749 galaxies at $z < 0.13$) – Chabrier IMF

$$\log(SFR_{NUV})\ (M_\odot\ \mathrm{yr}^{-1}) = 0.62 \times (\log[L_{NUV}(\mathrm{W\ Hz}^{-1})] - 21.5) + 0.014 \tag{B.4}$$

$$\log(SFR_{FUV})\ (M_\odot\ \mathrm{yr}^{-1}) = 0.75 \times (\log[L_{FUV}(\mathrm{W\ Hz}^{-1})] - 21.5) + 0.17 \tag{B.5}$$

Salim et al. (2007) – *GALEX*-SDSS DR3 (48 295 galaxies at $0.005 < z < 0.22$) – Chabrier IMF

$$\log(SFR_{NUV})\ (M_\odot\ \mathrm{yr}^{-1}) = \log[L_{NUV}(\mathrm{W\ Hz}^{-1})] - 21.14 \tag{B.6}$$

$$\log(SFR_{FUV})\ (M_\odot\ \mathrm{yr}^{-1}) = \log[L_{NUV}(\mathrm{W\ Hz}^{-1})] - 21.16 \tag{B.7}$$

Rosa-González et al. (2002) – 31 nearby star-forming galaxies – Salpeter IMF – Attenuation correction included

$$\log(\mathrm{SFR}_{UV})\ (M_\odot\ \mathrm{yr}^{-1}) = \log[L_{UV}(\mathrm{W\ Hz}^{-1})] - 20.19 \tag{B.8}$$

B.2. u band

Davies et al. (2016) – GAMA II survey (3749 galaxies at $z < 0.13$) – Chabrier IMF

$$\log(SFR_u)\ (M_\odot\ \mathrm{yr}^{-1}) = 0.92 \times (\log[L_u(\mathrm{W\ Hz}^{-1})] - 21.25) - 0.079 \tag{B.9}$$

Moustakas et al. (2006) – SDSS (120 846 galaxies at $z \sim 0.1$) – Salpeter IMF – Attenuation correction included

$$\log(\mathrm{SFR_u})\ (M_\odot\ \mathrm{yr}^{-1}) = \log[L_u(\mathrm{erg\ s}^{-1})]] - 42.85 \tag{B.10}$$

Hopkins et al. (2003) – SDSS (2625 galaxies at $z < 0.36$) – Salpeter IMF

$$\log(\mathrm{SFR_u})\ (M_\odot\ \mathrm{yr}^{-1}) = 1.186 \times \log[L_u(\mathrm{W\ Hz}^{-1})] - 21.25 \tag{B.11}$$

Zhou et al. (2017) – South Galactic Cap *u*-band Sky Survey (9596 galaxies at $z < 0.4$) – Salpeter IMF

$$\log(\mathrm{SFR_u})\ (M_\odot\ \mathrm{yr}^{-1}) = 1.25 \times \log[L_u(\mathrm{W\ Hz}^{-1})] - 54.17 \tag{B.12}$$

B.3. Infrared bands

Brown et al. (2017) – Kroupa IMF

$f = \log(L_{8\mu m})$ with $A = 1.3$ and $B = 40.88$ (B.13)

$f = \log(L_{24\mu m})$ with $A = 1.3$ and $B = 40.93$ (B.14)

Wu et al. (2005) – *Spitzer* First Look Survey (91 galaxies + lines from SDSS) – Salpeter IMF

$$\log(\mathrm{SFR}_{8\mu\mathrm{m}})\ (M_\odot\ \mathrm{yr}^{-1}) = \log[L_{8\mu m}(L_\odot)] - 9.14 \tag{B.15}$$

Young et al. (2014) – NOAO Deep Wide Field Survey (91 galaxies, $z < 0.1$) – Salpeter IMF

$$\log(\mathrm{SFR}_{8\mu\mathrm{m}})\ (M_\odot\ \mathrm{yr}^{-1}) = 0.93 \times \log[L_{8\mu m}(L_\odot)] - 8.5 \tag{B.16}$$

Pérez-González et al. (2006) – Galaxy M81 – Salpeter IMF

$$\log(\mathrm{SFR}_{8\mu\mathrm{m}})\ (M_\odot\ \mathrm{yr}^{-1}) = 0.87 \times \log[L_{8\mu m}(L_\odot)] - 7.9 \tag{B.17}$$

Rieke et al. (2009) – SED templates based on local galaxies – Kroupa IMF

$$\log(\mathrm{SFR}_{24\mu\mathrm{m}})\ (M_\odot\ \mathrm{yr}^{-1}) = \log[L_{24\mu m}(\mathrm{erg\ s}^{-1})] - 42.69 \text{ if } L_{24\mu m} > 4 \times 10^{42}\ \mathrm{erg\ s}^{-1} \tag{B.18}$$

$$\log(\mathrm{SFR}_{24\mu\mathrm{m}})\ (M_\odot\ \mathrm{yr}^{-1}) = 1.05 \times \log[L_{24\mu m}(\mathrm{erg\ s}^{-1})] - 44.79 \text{ if } L_{24\mu m} > 5 \times 10^{43}\ \mathrm{erg\ s}^{-1} \tag{B.19}$$

Zhu et al. (2008) – SDSS-IRAC/MIPS24μm (413 galaxies) – Kroupa IMF

$$\log(\mathrm{SFR}_{24\mu\mathrm{m}})\ (M_\odot\ \mathrm{yr}^{-1}) = 0.848 \times \log[L_{24\mu m}(\mathrm{erg\ s}^{-1})] - 36.09 \tag{B.20}$$

Relaño et al. (2007) – *Spitzer*-HST (41 nearby galaxies) – Kroupa IMF

$$\log(\mathrm{SFR}_{24\mu\mathrm{m}})\ (M_\odot\ \mathrm{yr}^{-1}) = 0.826 \times \log[L_{24\mu m}(\mathrm{erg\ s}^{-1})] - 35.25 \tag{B.21}$$

B.4. $L_{\rm TIR}$

Kennicutt (1998) – Salpeter IMF

$$\log(\mathrm{SFR_{TIR}})\ (M_\odot\ \mathrm{yr}^{-1}) = \log[L_{\rm TIR}(\mathrm{erg\ s}^{-1})] - 43.35 \tag{B.22}$$

B.5. Composite tracers

Bell et al. (2005) – PEGASE calibration – Kroupa IMF

$$\log(\mathrm{SFR_{TIR+2800Å}})\ (M_\odot\ \mathrm{yr}^{-1}) = \log[(L_{\rm TIR} + 3.3L_{2800Å})(L_\odot)] - 10.0 \tag{B.23}$$

Kennicutt et al. (2009) – SINGS and Moustakas & Kennicutt (2006) survey (171 galaxies at $D < 154$ Mpc) – Kroupa IMF

$$\log(\mathrm{SFR_{[O\,II]+\lambda}})\ (M_\odot\ \mathrm{yr}^{-1}) = 42.75 + \log[(L_{\rm [O\,II]} + a_\lambda L_\lambda)(\mathrm{erg\ s}^{-1})] \tag{B.24}$$

$$\text{where } a_\lambda = 0.016 - 0.029 - 0.0036\ for\ \lambda = \ 8\ \mu m,\ 24\ \mu m\ and\ L_{\rm TIR},\ \text{respectively.} \tag{B.25}$$

Clark et al. (2015) – H ATLAS (Phase-I Version-3)-SDSS-GAMA (42 galaxies at $D < 46$ Mpc) – Kroupa (UV) / Chabrier (IR) IMF

$$\log(\mathrm{SFR_{FUV+W4}})\ (M_\odot\ \mathrm{yr}^{-1}) = \log[(10^{-9.69}L_{FUV} + (1-\eta)10^{-9.125}L_{W4})(L_\odot)] \tag{B.26}$$

Arnouts et al. (2013) – Deep 24 μm-COSMOS-SWIRE (~17 600 galaxies at $0.2 < z < 1.3$) – Chabrier IMF

$$NRK = 0.31(NUV - r) + 0.958(r - K_{\rm s}) \tag{B.27}$$

$$\log(IRX) = -0.69 + 3.43z - 3.49z^2 + 1.22z^3 + 0.63 \times NRK \tag{B.28}$$

$$\log(\mathrm{SFR_{NrK}})\ (M_\odot\ \mathrm{yr}^{-1}) = \log[(L_{\rm TIR} + 2.3L_{NUV})(L_\odot)] - 10.07 \tag{B.29}$$

Boquien et al. (2014) – For $Z = 0.02$ and $\tau = 100$ Myr – Chabrier IMF

$$\log(\mathrm{SFR_{FUV+24\mu m}})\ (M_\odot\ \mathrm{yr}^{-1}) = -21.09 + \log[(L_{FUV} + 3.89L_{24\mu m})(\mathrm{W\ Hz}^{-1})] \tag{B.30}$$

B.6. Lines

Kennicutt (1998) – Salpeter IMF

$$\log(\mathrm{SFR_{H\alpha}})\ (M_\odot\ \mathrm{yr}^{-1}) = \log[L_{\rm H\alpha}(\mathrm{erg\ s}^{-1})] - 41.10 \tag{B.31}$$

$$\log(\mathrm{SFR_{[O\,II]}})\ (M_\odot\ \mathrm{yr}^{-1}) = \log[L_{\rm [O\,II]}(\mathrm{erg\ s}^{-1})] - 41.20 \tag{B.32}$$

Villa-Vélez et al. (2021) – 182 galaxies of COSMOS ($z \sim 1.6$) – Chabrier IMF

$$\log(\mathrm{SFR_{[O\,III]}})\ (M_\odot\ \mathrm{yr}^{-1}) = \log[L_{\rm [O\,III]}(\mathrm{erg\ s}^{-1})] - A \tag{B.33}$$

$$\text{where } A = 41.72,\ 41.35,\ 41.24,\ 41.01\ and\ 40.76\ for\ log(U) \sim -1.25,\ -1.75,\ -2.25,\ -2.75\ and\ -3.25,\ \text{respectively.} \tag{B.34}$$

Rosa-González et al. (2002) – Salpeter IMF – Attenuation correction included

$$\log(\mathrm{SFR_{[O\,II]}})\ (M_\odot\ \mathrm{yr}^{-1}) = \log[L_{\rm [O\,II]}(\mathrm{erg\ s}^{-1})] - 40.08 \tag{B.35}$$

Gilbank et al. (2010) – SDSS (43 155 galaxies at $0.032 < z < 0.2$) – Salpeter IMF – Attenuation correction included ($A_{\rm H\alpha} = 1$ mag)

$$\log(\mathrm{SFR_{[O\,II]}})\ (M_\odot\ \mathrm{yr}^{-1}) = \log[L_{\rm [O\,II]}(\mathrm{erg\ s}^{-1})] - \log[a \times \tanh((x-b)/c) + d] - 40.40 \tag{B.36}$$

$$\text{where } x = \log(M_*/M_\odot),\ a = -1.424,\ b = 9.827,\ c = 0.572,\ d = 1.7 \tag{B.37}$$

Appendix C: SFRs from recipes versus SFRs from CIGALE

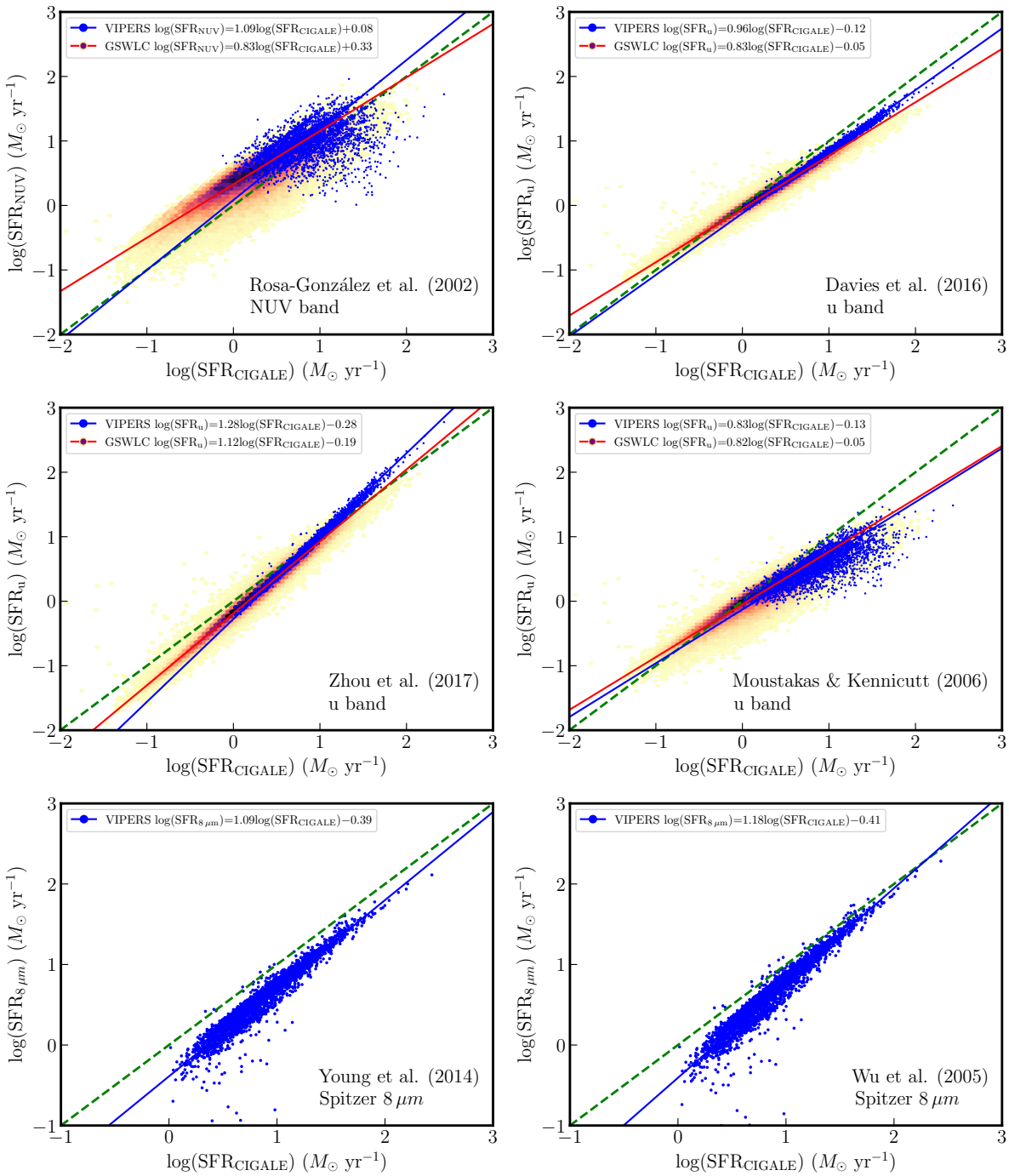


Fig. C.1. SFRs derived using different calibrations (written in the bottom right in each plot) for VIPERS (blue points) and GSWLC (density pot). The dashed blue, red, and green lines are the fit for VIPERS, GSWLC, and the one-to-one relation, respectively.

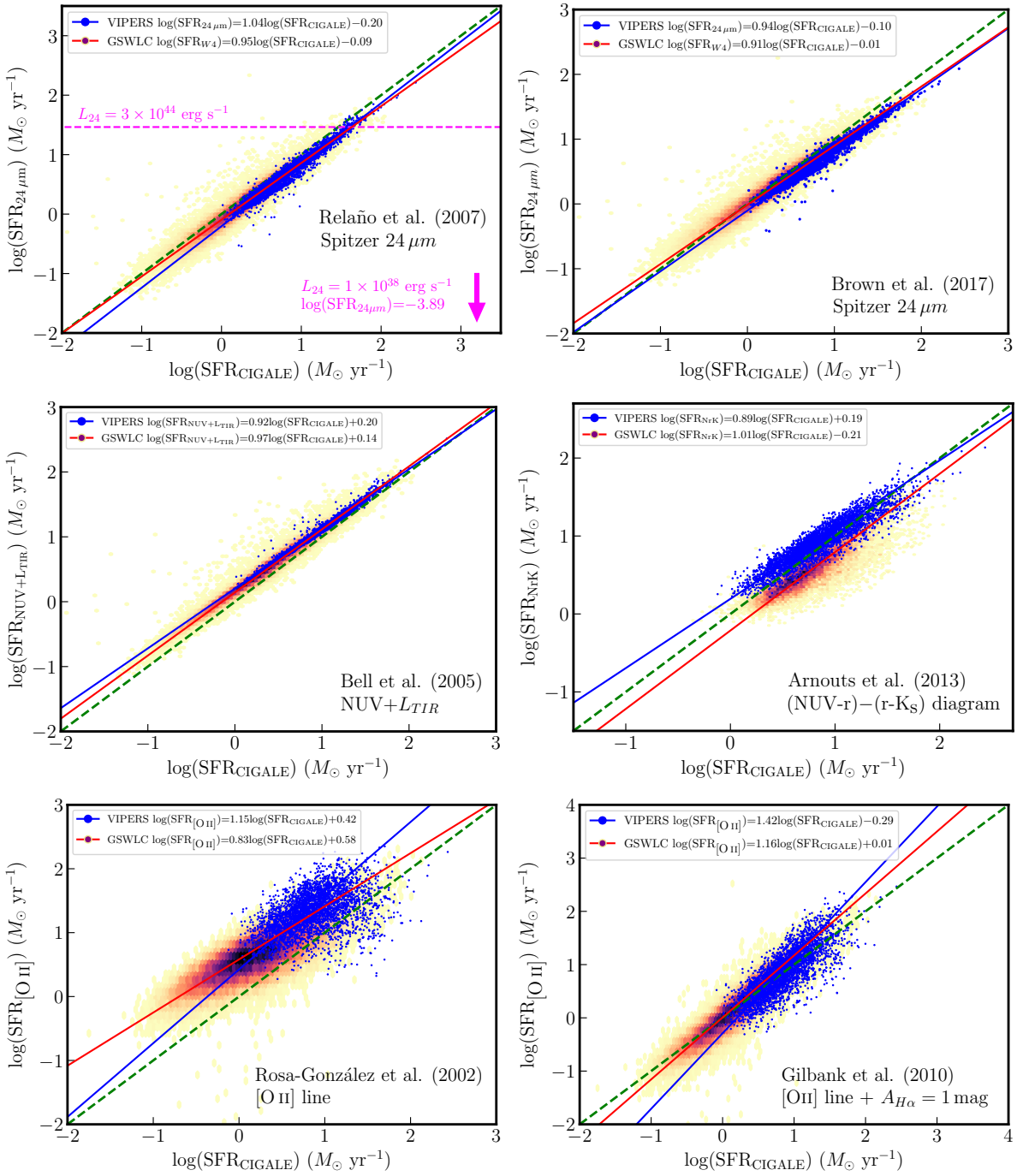


Fig. C.2. Same as for Fig. C.1. The pink arrow indicates that the lowest L_{24} used to calibrate the Relaño et al. (2007) relation is out of the range of the image. For GSWLC, the WISE-4 luminosity is converted to a Spitzer 24-μm luminosity.

Appendix D: WISE-3, WISE-4, and *Spitzer* 24-μm as SFR calibrators at $0 < z < 0.9$

The SFR calibrations based on the monochromatic luminosity around 20 μm give a good estimation of the SFR because the luminosity at this wavelength traces reasonably well $L_{\rm TIR}$, which is itself a good SFR tracer. Since most of the WISE-4 measurements are upper limits at $z > 0.5$, we did not calibrate the WISE-4 band as previously done in the local Universe (e.g., Cluver et al. 2014, 2017.

Using SED templates, it is possible to obtain reliable measurements of $L_{\rm TIR}$ and the SFR based on the observed flux in the WISE-3, WISE-4, and the *Spitzer* 24-μm band. Figure D.1 shows the SFR estimated from the observed flux from WISE-4 (from unWISE) for GSWLC and *Spitzer* 24 μm for VIPERS, using the BOSA templates (Boquien & Salim 2021, valid up to $z = 4$). Flux uncertainties are propagated through the templates to estimate the uncertainties on the SFR. For GSWLC, the agreement with CIGALE SFR is good, with a mean and scatter of 0.05 and 0.13 dex. Using *Spitzer* 24-μm measurements, the mean and scatter are equal to 0.02 and 0.20 dex for VIPERS galaxies, but only galaxies for which $L_{\rm TIR} > 3.5 \times 10^{10}\ L_{\odot}$ (estimated with CIGALE) are detected at 24 μm.

To estimate at which $L_{\rm TIR}$, WISE-3, WISE-4 and *Spitzer* 24-μm measurements can be reliably used as SFR tracers, we used the BOSA templates to derive the 3σ detection limit at the redshift limits of GSWLC and VIPERS. Horizontal dashed lines in Figure D.1 show the 3σ limits at $z = 0.01,\ 0.3,\ 0.5$, and 0.9 in terms of log(SFR), above which each of the bands can be used as an SFR tracer. The derivation of SFR from *Spitzer* 24 μm at $z = 0.01 - 0.3$ can be performed for most of the galaxies ($3.9 \times 10^7 - 2.6 \times 10^{10}\ L_{\odot}$), although it is reliable only for luminous galaxies ($9.7 \times 10^{10} - 2.4 \times 10^{11}\ L_{\odot}$) at $z = 0.5 - 0.9$. On the contrary, the sensitivity of the WISE-4 band is too low, and only very luminous galaxies ($1.2 \times 10^{12} - 2.6 \times 10^{12}\ L_{\odot}$) can be observed at $z = 0.5 - 0.9$, while this band remains a good SFR tracer for GSWLC ($4.1 \times 10^8 - 3.1 \times 10^{11}\ L_{\odot}$). The sensitivity of WISE-3 is in between *Spitzer* 24 μm and WISE-4 but this band remains unuseful for most of the VIPERS galaxies ($2.6 \times 10^{11} - 8.3 \times 10^{11}\ L_{\odot}$), while the SFR of most of the GSWLC galaxies can be derived using this band ($9.3 \times 10^7 - 7.2 \times 10^{10}\ L_{\odot}$). Good detections (i.e., 3σ) of all galaxies in our VIPERS sample ($L > 1.9 \times 10^9\ L_{\odot}$) would require a 3σ sensitivity at 12 and 24 μm around 0.58 and 1.7 μJy, respectively.

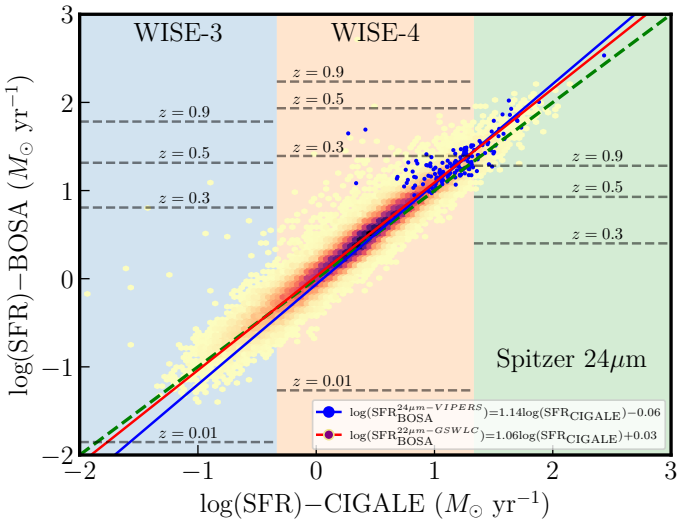


Fig. D.1. Comparison of SFRs from the observed fluxes of *Spitzer* (blue, VIPERS) and WISE-4 (red, GSWLC) using the BOSA templates with SFRs derived from CIGALE. The limits, computed for the redshift limits of VIPERS and GSWLC, above which WISE-3 (blue area), WISE-4 (orange area), and *Spitzer* 24 μm (green area) can be used to reliably estimate the SFR are shown (dashed black lines). In units of log(SFR [$M_\odot$ yr^{-1}]), the limits, for increasing redshift, are: -1.9, 0.8, 1.31, and 1.8 (WISE-3), -1.3, 1.4, 1.9, and 2.2 (WISE-4), and -2.2, 0.4, 0.9, and 1.3 (*Spitzer* 24 μm).

Appendix E: Parameters of the fit performed in this work

Table E.1. Parameters and properties of each fit presented in this work.

Reference (1)	Catalog – Band (2)	N (3)	m (4)	b (5)	Pearson (6)	Mean (7)	Scatter (8)	CCC (9)	CCC_{GV} (10)
				FUV					
Brown et al. (2017)[2]	V – (Calzetti)	3 457	1.21	−0.28	0.99	0.09	0.10	0.94	
	G – (Calzetti)	91 533	0.95	−0.06	0.83	0.02	0.30	0.83	0.91
	V – (Hao)	3 457	1.05	−0.04	0.99	0.01	0.05	0.99	
	G – (Hao)	91 533	0.95	0.02	0.88	−0.02	0.25	0.88	0.94
Davies et al. (2016)	V	3 457	0.82	0.0	0.99	0.16	0.07	0.87	0.88
	G	91 533	0.67	0.12	0.85	−0.07	0.25	0.82	
Salim et al. (2007)	V	3 457	1.0	−0.01	1.00	0.02	0.03	0.99	
	G	91 533	0.88	0.09	0.87	−0.08	0.24	0.86	0.94
				NUV					
Davies et al. (2016)	V	3 457	0.80	−0.13	0.97	0.29	0.10	0.67	0.79
	G	91 533	0.59	0.07	0.80	−0.01	0.29	0.76	
Salim et al. (2007)	V	3 457	1.0	−0.01	1.00	0.02	0.03	0.99	
	G	91 533	0.89	0.09	0.87	−0.08	0.24	0.86	0.93
Rosa-González et al. (2002)	V	3 457	1.09	0.08	0.47	−0.11	0.32	0.43	0.78
	G	91 533	0.83	0.33	0.86	−0.20	0.25	0.77	
				***u*-band**					
Davies et al. (2016)[3]	V	3 457	0.86	−0.05	0.99	0.18	0.06	0.85	0.81
	G	90 965[4]	0.83	−0.33	0.89	0.42	0.22	0.62	
Hopkins et al. (2003)	V	3 457	1.23	−0.26	0.99	0.07	0.08	0.96	
	G	91 533	1.06	−0.17	0.99	0.15	0.09	0.94	0.97
Zhou et al. (2017)	V	3 457	1.28	−0.28	0.99	0.04	0.10	0.97	0.96
	G	91 533	1.12	−0.19	0.99	0.16	0.10	0.93	
Moustakas et al. (2006)	V	3 457	0.83	−0.13	0.79	0.31	0.21	0.50	0.80
	G	91 533	0.82	−0.05	0.93	0.14	0.18	0.87	
Davies et al. (2016)	V	3 457	0.96	−0.12	0.99	0.17	0.04	0.88	
	G	91 533	0.83	−0.05	0.99	0.09	0.11	0.94	0.95
				8 μm					
Brown et al. (2017)	V	3 385[5]	0.91	−0.03	0.96	0.10	0.10	0.91	
Pérez-González et al. (2006)	V	3 385[5]	1.03	−0.33	0.96	0.29	0.11	0.71	
Young et al. (2014)	V	3 385[5]	1.09	−0.39	0.96	0.30	0.12	0.72	
Wu et al. (2005)	V	3 385[5]	1.18	−0.41	0.96	0.24	0.14	0.78	

Table E.1. continued.

Reference (1)	Catalog – Band (2)	N (3)	m (4)	b (5)	Pearson (6)	Mean (7)	Scatter (8)	CCC (9)	CCC_{GV} (10)
			24 μm						
Rieke et al. (2009)	V	3 385[5]	1.28	−0.28	0.97	0.004	0.13	0.95	0.96
	G	68 911[6]	1.16	−0.13	0.97	0.07	0.16	0.94	
Zhu et al. (2008)	V	3 385[5]	1.06	−0.11	0.97	0.04	0.08	0.97	
	G	68 911[6]	0.98	0.0	0.97	0.01	0.12	0.97	0.98
Relaño et al. (2007)	V	3 385[5]	1.04	−0.20	0.97	0.15	0.08	0.89	0.94
	G	68 911[6]	0.95	−0.09	0.97	0.11	0.12	0.94	
Brown et al. (2017)	V	3 385[5]	0.94	−0.10	0.98	0.14	0.08	0.89	0.95
	G	68 911[6]	0.91	−0.01	0.97	0.04	0.12	0.96	
			L_{TIR}						
Kennicutt (1998)	V	3 385[5]	1.22	−0.26	0.98	0.04	0.11	0.95	0.97
	G	68 911[6]	1.08	0.03	0.96	0.04	0.13	0.96	
			Composite tracers						
Kennicutt et al. (2009)	V – [O II]+8 μm	3 385[5]	0.93	−0.04	0.96	0.12	0.09	0.91	
	V – [O II]+24 μm	3 385[5]	1.0	0.04	0.98	−0.04	0.06	0.98	
	G – [O II]+WISE-4	35 922[6,7]	1.0	−0.01	0.97	0.02	0.10	0.97	0.98
	V – [O II]+L_{TIR}	3 385[5]	0.98	0.0	0.98	0.01	0.07	0.98	0.96
	G – [O II]+L_{TIR}	35 922[6,7]	1.05	0.08	0.92	−0.06	0.18	0.91	
Arnouts et al. (2013)	V – NUVrK_s	3 457	0.89	0.19	0.92	−0.07	0.14	0.89	0.80
	G – NUVrK_s	19 438[8]	1.01	−0.21	0.87	0.21	0.15	0.68	
Bell et al. (2005)	V – NUV+L_{TIR}	3 385[5]	0.92	0.20	0.99	−0.13	0.04	0.92	0.97
	G – NUV+L_{TIR}	68 911[6]	0.97	0.14	0.98	−0.14	0.09	0.93	
Clark et al. (2015)	V – FUV+24 μm	3 385[5]	1.01	0.07	1.0	−0.08	0.03	0.97	0.97
	G – FUV+WISE-4	68 911[6]	1.01	−0.11	0.98	0.12	0.10	0.95	
Boquien et al. (2014)	V – FUV+24 μm	3 385[5]	1.01	−0.01	1.00	−0.01	0.03	0.99	
	G – FUV+WISE-4	68 911[6]	1.07	−0.05	0.98	0.02	0.10	0.98	0.99

Table E.1. continued.

Reference (1)	Catalog – Band (2)	N (3)	m (4)	b (5)	Pearson (6)	Mean (7)	Scatter (8)	CCC (9)	CCC_{GV} (10)
Spectral lines									
Kennicutt (1998)	V – Hβ	3 457	1.26	−0.25	0.88	−0.01	0.19	0.87	0.94
	G – Hβ	91 533	1.04	−0.08	0.94	0.07	0.19	0.92	
Kennicutt (1998)	V – [O II]	3 457	1.03	0.12	0.85	−0.11	0.19	0.81	0.91
	G – [O II]	48 845[7]	0.84	0.01	0.86	0.08	0.23	0.84	
	V – [O II] Reddening	3 457	1.12	−0.11	0.90	0.01	0.17	0.89	0.93
	G – [O II] Reddening	48 845[7]	0.92	−0.10	0.88	0.12	0.22	0.86	
	V – [O II] Metal	3 192[9,10]	1.25	−0.27	0.93	0.05	0.17	0.90	
	G – [O II] Metal	35 403[9,10,11]	0.94	−0.07	0.91	0.06	0.20	0.90	0.94
Kennicutt (1998)	V – [O III]	3 457	1.20	−0.14	0.65	−0.04	0.31	0.64	0.81
	G – [O III]	91 533	0.88	0.07	0.78	−0.17	0.32	0.73	
	V – [O III] Metal	3 192[9,10]	1.25	−0.22	0.77	0.05	0.26	0.75	
	G – [O III] Metal	35 396[9,10,11]	1.16	−0.05	0.93	0.04	0.20	0.92	0.91
Villa-Vélez et al. (2021)	V – [O III]	3 382[9]	1.10	0.04	0.79	0.09	0.24	0.76	0.89
	G – [O III]	35 451[9]	0.95	−0.13	0.87	−0.19	0.24	0.80	
Rosa-González et al. (2002)	V – [O II]	3 457	1.15	0.42	0.44	−0.46	0.35	0.22	0.57
	G – [O II]	48 845[7]	0.83	0.58	0.76	−0.44	0.30	0.48	
Gilbank et al. (2010)	V – [O II]	3 457	1.42	−0.29	0.80	−0.00	0.26	0.78	0.91
	G – [O II]	48 845[7]	1.16	0.01	0.92	0.01	0.22	0.91	

Notes. (1) Reference to the literature, (2) Catalog used (V: VIPERS, G: GSWLC) and bands (for composite and spectral line tracers) used to derive the SFR, (3) Number of galaxies used to perform the fit, (4) and (5) coefficients of the linear fit ($y = mx + b$)[1] , (6) Pearson coefficient, (7) Mean, (8) Scatter estimated from calibrations; additional scatter from template bias can be found in Sect. 5.1, (9) Concordance correlation coefficient, and (10) Concordance correlation coefficient for VIPERS+GSWLC. For each band, the preferred calibration for GSWLC and VIPERS is shown in blue, and in magenta for GSWLC+VIPERS. [1]Uncertainties on the coefficient m and b are $\sim 10^{-2}$. [2]Using the Calzetti et al. (2000) and Hao et al. (2011) attenuation recipes. [3]Assuming an old-stellar population decontamination. [4]The decontamination cannot be applied to all GSWLC galaxies. [5]Galaxies whose SED fitting was incorrect in the IR were removed. [6]Galaxies with available L_{W4}. [7][O II] sample (see Tab. 3). [8]Galaxies at $z < 0.1$ and with $NRK_{sSFR} > 1.9$ were excluded (see Sect. 4.1.4). [9]Galaxies for which [O III]λ5007/[O II]λ3727 < 2 (see Sect. 4.2.2). [10]Galaxies for which log(O/H)+12 < 8.4 were excluded (see Sect. 4.2.2). [11][O II]+[O III] sample (see Tab. 3).